Theory of Lightwave-Driven Quantum Electronics in Solids

by

Markus Borsch

A dissertation submitted in partial fulfillment
of the requirements for the degree of
Doctor of Philosophy
(Electrical and Computer Engineering)
in the University of Michigan
2023

Doctoral Committee:

Professor Mackillo Kira, Chair
Professor Steven T. Cundiff
Associate Professor Parag B. Deotare
Professor Theodore B. Norris

Markus Borsch

markbor@umich.edu

ORCID: 0000-0002-6152-1921

Dedication

To my parents.

Acknowledgements

My first thanks go to my research advisor Mackillo Kira. Ever since I joined his research group ten years ago at the University of Marburg in Germany, he has provided me with much support, interesting research questions, and great opportunities, not least of which his offer to join him build up a new research group at the University of Michigan and pursue my PhD at this institution.

I would also like to thank Steven Cundiff, Parag Deotare, and Theodore Norris for serving on my thesis committee.

Much of this work would not have been possible without the many people who have collaborated with me over the years. Rupert Huber has provided us with unique experiments and his perspectives and push towards the limitations of both his experiments and our theory has lead to a very fruitful collaboration. Much of the experimental work was performed by his students Christoph Schmid and Josef Freudenstein, who were fantastic to work with. The first experimental data I ever analyzed was measured by Eric Martin in Steven Cundiff's lab. I am grateful for the many meetings we had and their patience in explaining every detail of their experiment. Towards the end of my PhD work I have also been involved in a project with Parag Deotare. I really appreciate the interesting discussions I had with him and the challenges he posed that pushed our theory approach in new directions.

I would also like thank my research groups. Starting with the Semiconductor Theory Group in Marburg (Ulrich Huttner, Christian Berger, Johannes Steiner, Stephan W. Koch, and the others) and continuing at the Quantum Science Theory Lab. Here, I want to thank in particular Benjamin Girodias and Matthias Florian who I have directly worked with on various projects, Ady Hambarde, Cody Patterson, Qiannan Wen, Weiwei Jiang, You Wu, who I have had many discussions with, as well as the many other people that have crossed my path in the lab over the years.

Fortunately, I also had many great connections outside of academia that I want to thank. My roommates, in particular my first ones, helped me a great deal learn about and navigate this country I just moved to. All the people I played Ultimate Frisbee with over the years, in particular the HAC group for year-round games, and especially John and Aneet. All the great friends I made pondering over pieces of plastic and cardboard, including, but not limited to, Ariel, Elise, Ethan, Greg, Kristian, Rachel, and Zack.

Particular thanks to Em*i*ly for her *l*ove and support. There are so many great memor*i*es. From Saturday Dinners to Ba*k*ing Wedn*e*sdays, from *b*ike rides to hiking to*u*rs, from movie ni*g*hts to cro*s*swords, and . . . silliness.

Finally, the biggest thanks to my family, Heike, Manfred, and Lisa. I am beyond grateful for their support in everything I am doing, even if that entails moving 6600 km away.

Contents

List of Figures

List of Appendices

Abstract

Lightwave electronics is based on the idea of using the instantaneous field of strong optical waves to drive and sculpt electronic states on ultrafast time scales. By utilizing the oscillation cycle of light, electronic currents can be switched thousand times faster than traditional electronics to enable petahertz electronics, properties of electronic states in solids become accessible for quantum information applications, and access to correlated many-body states in solids is provided. In this Thesis, I present a comprehensive many-body quantum theory based on the quantum-dynamic cluster expansion approach to quantitatively describe lightwave-driven many-body excitations in quantum materials. The theory is applied to analyze lightwave excitations in quantitative theory–experiment comparisons which led to the development of an ecosystem of new lightwave-based techniques to characterize quantum materials and probe quantum correlations in situ. The theory is also extended to describe spatially inhomogeneous excitations and nanostructures.

First, the theoretical background of the quantum-dynamic cluster expansion is summarized and the theory to describe lightwave excitations in two-dimensional materials derived. I describe how the resulting semiconductor Bloch equations can be combined with *ab initio* density-functional theory computations and solved numerically on the full two-dimensional Brillouin zone for a predictive description of the excitation dynamics of realistic materials.

By analyzing the emission dynamics of lightwave-driven coherent excitons in quantum materials, we discovered emergent interference patterns in momentum space, crystal-momentum combs, which precisely locate the emission of harmonic sidebands in momentum space and connect their intensities to the electronic band structure. I apply this connection to

reconstruct the band structure from harmonic sideband emission, light that is emitted from a semiconductor in a nonlinear process after excitation with two colors, and demonstrate the approach for two-dimensional tungsten diselenide in a comprehensive theory-experiment comparison.

Harmonic sidebands in solids are generated from lightwave-driven electron–hole recollisions and information about the electronic dynamics is encoded in the emitted light. In a quasiparticle-collider approach, we utilize extremely nonperturbative effects to detect millielectronvolt correlations with attosecond precision, beating the Heisenberg uncertainty limit by two orders of magnitude. We find that strong excitonic correlations in monolayers of tungsten diselenide create a distinct delay in the attoclocking setup compared to a bulk sample with weaker correlations. In a detailed theory-experiment analysis, I demonstrate direct clocking of quasiparticle correlations with attosecond precision which I connect to the dynamics of electron–hole pairs in phase-space using a Wigner-function representation.

The valley-degree of freedom, emergent in some two-dimensional quantum materials, can be switched coherently on ultrafast time scales using lightwave excitations with potential applications in solid-state based classical and quantum-information processing. I apply the developed theory to predict conditions for efficient coherent valleytronic switches and propose how sequencing of multiple switches with petahertz clock rates could be realized and detected experimentally.

Finally, I extend the semiconductor Bloch equations to describe spatial semiconductor and nanostructure excitation by using a Wigner-function based formulation of the single and two-particle correlations for an efficient and intuitive representation in phase space. I find that the spatial dynamics of coherent excitations exhibits a quantum character while electrons, holes, and incoherent excitons show a classical behavior in their spatial kinetics. These properties are identified in a careful theoretical analysis and compared to experimental investigations of the coherent and incoherent dynamics of spatially local excitations.

Chapter 1

Introduction

Information technology is based on electronic and optoelectronic devices and has seen rapid technological advancements that have transformed society with applications like the internet, smartphones, and machine learning. The triumphant success of information technology, producing an exponential growth of computing power over the last 60 years [1, 2], is owed to the integrability and scalability of solid-state devices which are products of the first quantum revolution [3]. While a quantum mechanical description is necessary to understand how electrons move in solids [4, 5], the functionality of solid-state devices can often be described in terms of classical electric currents and light.

Today, we are at the cusp of a second quantum revolution [3] as evidenced by recent breakthroughs in quantum computing [6, 7], communication [8, 9], and sensing [10, 11], which aim to derive functionality from quantum mechanics directly instead of using devices that merely work because of quantum mechanics. Several platforms have been developed to study quantum mechanics and derive functionality from it, some of which include quantum dots [12], superconducting qubits [13], cold atoms [14, 15], integrated photonics [16, 17], and vacancy centers [18, 19]. These are often laboratory-size instruments that require peripheral infrastructure like dilution refrigerators or laser systems. A robust and universal quantum platform comparable to that of solid-state devices of the first quantum revolution has not been identified yet.

Lightwave quantum electronics [20] could provide such a platform by utilizing the quantum properties of electrons in solid-state systems. If successful, such devices could directly be integrated with electronic and optoelectronic applications. Lightwave electronics aims to sculpt the quantum dynamics of electrons on time scales faster than the oscillation period of light by using intense optical waves as fast biasing fields that interact with the electron's charge. This concept was first explored in atomic and molecular physics [21] and was used to explain high-harmonic (HH) generation [22, 23], a nonlinear process in which a target emits several orders of harmonics of the light illuminating it. High-harmonic generation can be understood through the semiclassical three-step model (3SM) [24]: (i) The field of a strong lightwave ionizes and electron from a state bound to the ionic core; (ii) The field then accelerates the effectively free electron away from the ion and increases its kinetic energy; (iii) As the oscillating field changes its sign, the electron returns to its ion core and releases its excess kinetic energy as HH emission upon collision with the ion. By analyzing the generated HH, information about the electron's state and can be deduced. This idea laid the foundations of attosecond physics [21, 25–28] that enabled generation and measurement of attosecond pulses in the extreme-ultraviolet [25, 29–32], imaging dynamic changes in molecular structures [33–35], and tomographic imaging of molecular orbitals [36–38].

In crystalline solids [4, 5], ionic cores are arranged in a crystal structure. When electrons move in a solid, many of its properties become strongly distorted and defy classical intuition. Instead of being bound to a single ion, electrons in solids occupy delocalized Bloch states [39] that extend over the entire crystal. The electron's mass can change with velocity, the spin can flip creating magnetization, or it can encounter energy-forbidden regions dictating materials to be conductive or insulating. Furthermore, Coulomb interaction between electrons and ionic cores that make up a solid lead to a wide variety of emergent quantum phenomena such as the binding of pairs of electrons and holes into excitons [40–42], higher order many-body complexes [42–44], and superconducting quantum phases [45] which can be functionalized and manipulated in lightwave quantum electronics.

First lightwave-electronic investigations in solids explored Rabi flopping [46–49] between excitonic $1s$ and $2p$ states. The HH generation in solids was first observed [50] in ZnS where harmonics up to the 7th order were detected using strong mid-infrared pulses with peak intensities in the order of 10^{12} W/cm^2. Subsequently, up to 25 HHs extending above the band gap were observed in ZnO [51] and the first generation of phase-locked HH pulses in solids was achieved [52] using THz driving fields. Unlike HH generation from isolated atoms, HHs in solids originate from multiple processes: transitions between electronic bands (interband emission [53, 54]) and currents induced by the accelerated electrons (intraband emission [51, 55]). In addition, electrons with a broad range of momenta can be excited between multiple electronic bands [56] and electron acceleration can be strong enough to induce Bloch oscillations [52] across the periodic boundaries of the Brillouin zone, both of which compromise a simple 3SM interpretation.

The electronic motion in solids can be controlled and studied more precisely by pumping the system resonantly, creating coherent excitons, and driving the excited states with a second, strong lightwave. The coherent excitons [41], atom-like bound states between an electron and a hole, undergo an ionization–acceleration–recollision process that leads to the emission of harmonic sidebands (HSBs) and resembles the 3SM of atomic HH generation. This HSB modality was first demonstrated in the perturbative regime in GaAs quantum wells [57], subsequently observed in the non-perturbative regime [58] with detection of up to eighteen HSB orders, and the dynamic nature of quasiparticle collisions was studied [59].

The potential of lightwave electronics to manipulate electronic states on the timescale of light's oscillation cycle creates promising opportunities for quantum information applications. The basic concept of lightwave electronics in condensed matter has been proven [60–62], but innovation of actual applications is challenging because quantum effects are inherently counterintuitive, hard to grasp, and short lived. Efficient discovery of new applications requires robust quantum theories to work in conjunction with experiments. The results presented in this Thesis emerged from strong collaborations between our theory work and

different experimental groups. The main results presented include:

1. Development of a comprehensive theory framework to describe lightwave-electronic excitations in semiconductors.

2. Development of an ecosystem of lightwave-based techniques that use HSB generation to characterize quantum materials and probe quantum correlations in situ.

3. Theoretical discussion of the limitations of valleytronic-based lightwave quantum-information processing.

4. Development of a microscopic theory to describe the dynamics of spatially local excitations in semiconductor nanodevices.

This Thesis is organized as follows: Chapter 2 briefly summarizes the core concepts of many-body quantum theories, including the formalism of second quantization and quantum-dynamic cluster expansion (QDCE) that our theoretical investigations are based on. A detailed description of the microscopic theory that we developed to describe lightwave-electronic processes in semiconductors is given in Chapter 3. This theory is the basis of the results presented in Chapters 4, 5, and 6. Chapter 4 introduces a new technique, super-resolution crystal-momentum comb tomography, to reconstruct the electronic band structure of quantum materials from a set of HSB measurements. We demonstrate this technique in monolayer tungsten diselenide with extensive theory–experiment comparisons. In Chapter 5, we apply a quasiparticle-collider approach to probe the dynamics of electronic correlations on attosecond time scales which is demonstrated by theory–experiment comparisons in bulk and monolayer sample of tungsten diselenide. Chapter 6 discusses the potential and fundamental limitations of valleytronic-based information processing with petahertz clock rates by using strong lightwaves to switch the valleytronic state of electrons. The remaining chapters present results regarding the effect of spatial inhomogeneities such as created by spatially local excitations or excitations within nanostructures. Chapter 7 introduces a microscopic

theory based on a Wigner-function representation of clusters to describe such excitations. Chapter 8 discusses the effect of spatial inhomogeneities on coherent excitations on ultrafast time scales, including a comparison to experiment. In Chapter 9, we derive the macroscopic dynamics of incoherent excitons and compare the resulting equations to experiments. Finally, Chapter 10 provides a conclusion of the presented work and outlines future opportunities.

Chapter 2

Theoretical Background

The quantum dynamics of a single particle is described by quantum mechanics and can be efficiently solved numerically, if not analytically [63]. To describe solids, the dynamics of billions of interacting particles have to be considered, even for microscopically small samples. In this chapter, we briefly summarize the key concepts that form the foundation of our theoretical work. For a more extensive introduction we refer the reader to Reference [41] which we follow in this chapter.

The starting point of our quantum theory is the formulation of a Hamiltonian. For solids, the minimal-substitution Hamiltonian [41, 64, 65]

$$\hat{H}_N = \sum_{j=1}^{N} \left\{ \frac{[\mathbf{p}_j + |e|\mathbf{A}(\mathbf{r}_j)]^2}{2m_0} + U(\mathbf{r}_j) \right\} + \sum_{i<j}^{N} V(|\mathbf{r}_i - \mathbf{r}_j|) + \hat{H}_F + \hat{H}_{\text{ph}} \ , \tag{2.1}$$

is a common choice where $\mathbf{r}_j$ and $\mathbf{p}_j$ are the position and momentum operators of electrons with mass m_0 and charge $-|e|$ which move in a lattice-periodic potential $U(\mathbf{r})$ and couple to a quantized light field via the vector potential $\mathbf{A}(\mathbf{r})$. Electrons interact with each other via the Coulomb potential $V(\mathbf{r})$. $\hat{H}_F$ is the free-field Hamiltonian of the quantized light field and $\hat{H}_{ph}$ the phonon Hamiltonian.

Applying the Göppert-Mayer transformation [41, 64–66], we obtain the Hamiltonian in

the so-called length gauge:

$$\hat{H}^{\mathrm{GM}} = \sum_j \left[\frac{\mathbf{p}_j^2}{2m} + U(\mathbf{r}_j) \right] + \sum_j |e| \mathbf{r}_j \cdot \mathbf{E}(\mathbf{r}_j) + \sum_{i<j}^{N} V(|\mathbf{r}_i - \mathbf{r}_j|) + \hat{H}_F + \hat{H}_{ph} \, . \tag{2.2}$$

It describes the light-matter interaction by a coupling of the electronic dipole $-|e|\mathbf{r}$ with the electric field $\mathbf{E}$. The two Hamiltonians (2.1) and (2.2) are connected by a unitary transformation and describe the same system. However, depending on the specific problem, one might be more suitable than the other.

A thorough description of the formalism of second quantization can be found, for example, in References [41, 67, 68]. It provides an efficient way to describe many-body states in a Fock space by introducing creation and annihilation operators to construct Fock states that satisfy the respective exchange symmetries of fermions and bosons. Following the description in References [41], an operator $\hat{O}$ with real-space representation $U_K(\mathbf{r}_1, \dots \mathbf{r}_K)$ can be expressed in terms of field operators $\hat{\Psi}^\dagger(\mathbf{r})$ and $\hat{\Psi}(\mathbf{r})$ which create and annihilate an electron at position $\mathbf{r}$, respectively:

$$\hat{O} = \int \mathrm{d}^{3K} r \, \hat{\Psi}^\dagger(\mathbf{r}_1) \dots \hat{\Psi}^\dagger(\mathbf{r}_K) U_K(\mathbf{r}_1, \dots \mathbf{r}_K) \hat{\Psi}(\mathbf{r}_K) \dots \hat{\Psi}(\mathbf{r}_1) \, . \tag{2.3}$$

In the Heisenberg picture, the dynamics of an operator $\hat{O}$ can be derived from the Heisenberg equation of motion (HEM) [63, 69]

$$\mathrm{i}\hbar \frac{\partial}{\partial t} \hat{O} = \left[\hat{O}, \hat{H} \right] , \tag{2.4}$$

where $[a, b] = ab - ba$ denotes the commutator between a and b.

For fermions, operators of the form $\left\langle \hat{\Psi}^\dagger \dots \hat{\Psi}^\dagger \hat{\Psi} \dots \hat{\Psi} \right\rangle$ with N creation and N annihilation operators are of interest which we call N–particle operators. For interacting systems (which we discuss here) the Heisenberg equation of motion (2.4) couples the dynamics of N–particle operators to higher order ones (e.g. $N+1$). This leads to an infinite hierarchy of

coupled equations, known as the hierarchy problem [67]. We solve the hierarchy problem in the framework of the quantum-dynamic cluster expansion (QDCE) which is described in detail in References [41, 70]. It expands expectation values into their factorizable single-particle states $\langle 1\rangle$ (singlets), pure two-particle correlations $\Delta\langle 2\rangle$ (doublets), and higher order clusters $\Delta\langle N\rangle$ (triplets, quadruplets, and so on). For a two-particle interaction like the Coulomb interaction, the general dynamics of a N-particle cluster has the form [41, 70]

$$\mathrm{i}\hbar\frac{\partial}{\partial t}\Delta\langle N\rangle = \mathrm{F}[\langle 1\rangle, \Delta\langle 2\rangle, \ldots \Delta\langle N\rangle] + \mathrm{Hi}[\Delta\langle N+1\rangle] \,, \tag{2.5}$$

where the functional F contains products between $\langle 1\rangle, \Delta\langle 2\rangle, \ldots \Delta\langle N\rangle$ and Hi describes the coupling to higher order clusters. These equations still contain the hierarchy problem, however, the equation structure introduces a strictly sequential build up of correlations [41, 70–73] where clusters $\Delta\langle N+1\rangle$ can only appear if $\Delta\langle N\rangle$ already exist. This is different from the N-particle operators $\langle N\rangle$.

The sequential build up makes QDCE an ideal choice to describe the ultrafast lightwave electronic processes of interest in this Thesis. Classical lightwave excitations always start from single-particle states $\langle 1\rangle$ [70], limiting the number of clusters that exist on ultrafast time scales. Because of this, QDCE can systematically truncate the hierarchy problem by only including the relevant correlations and still solve the nonperturbative dynamics exactly.

Chapter 3

Microscopic Theory of Lightwave Electronics

3.1 Introduction

A wide array of simplified models have been used to describe various aspects of lightwave excitations in solids. Intraband currents, macroscopic currents that are generated from moving carriers within a single band, were computed from the classical dynamics of a single electron in a solid [51, 74], effective single-body Schrödinger equation [53, 75–77], or generalized optical Bloch equations [77, 78]. Floquet-Bloch theory [79–81], in which lightwave excitations create replicas of the electronic bands (Floquet bands), were applied to understand lightwave electronic effects in topological quantum materials. While these simplified models provide intuitive pictures and a qualitative understanding of specific mechanisms, they usually neglect many-body and interaction effects which can be significant in solids.

In my thesis work, I developed a comprehensive theory that exactly solves the nonperturbative dynamics of strong lightwave excitations, including many-body interactions, by combining the quantum-dynamic cluster expansion (QDCE) with realistic matrix elements from *ab initio* density-functional theory (DFT) [82–84]. By solving the resulting equations of motion on the full Brillouin zone including all relevant bands, we obtain a fully predictive, parameter free theory that can be compared quantitatively to experiments. In the later chapters, we demonstrate that our approach yields an unequaled agreement with experiments and

provides an unprecedented view into the dynamics of the microscopic state. In this chapter, I describe how the relevant equations of motion, the semiconductor Bloch equations (SBEs), are derived, combined with DFT, and solved self-consistently with Maxwell's equations to describe lightwave-electronic processes. The discussion is kept general wherever possible, but the theory is specifically developed to describe lightwave excitations in two-dimensional quantum materials such as monolayers of transition-metal dichalcogenides (TMDs.)

3.2 Envelope-function approximation

This work concentrates on lightwave electronics in planar nanostructures, more specifically monolayers of TMDs, and their interaction with classical light fields. The three-dimensional real-space coordinate $\mathbf{r} = (\mathbf{r}_\parallel, z)$ can be separated into the two-dimensional $\mathbf{r}_\parallel$ that is parallel to the nanostructure and the one-dimensional z that is perpendicular to it. Similarly, the wave vector can be separated into $\mathbf{k} = (\mathbf{k}_\parallel, k_z)$. The envelope-function approximation [41, 69] separates these two coordinates to effectively reduce the dimensionality of the electron dynamics to two dimensions. The application of this approach is not discussed explicitly in this Thesis and the reader is referred to References [41, 69] for details. From this point on, we apply the envelope function approximation and imply $\mathbf{k}_\parallel$ whenever $\mathbf{k}$ is written to keep notation short. Only the lowest subband resulting from the envelope-function approximation is considered.

3.3 Hamiltonian in second quantization

3.3.1 Single-particle basis

Equation (2.3) is used to convert the Hamiltonian (2.2) into second quantization. For solids, it is convenient to expand the field operators in a Bloch basis [41]

$$\hat{\Psi}(\mathbf{r}) \equiv \sum_{\lambda,\mathbf{k}} \phi_{\lambda,\mathbf{k}}(\mathbf{r}) a_{\lambda,\mathbf{k}} \ , \quad \hat{\Psi}^\dagger(\mathbf{r}) \equiv \sum_{\lambda,\mathbf{k}} \phi^*_{\lambda,\mathbf{k}}(\mathbf{r}) a^\dagger_{\lambda,\mathbf{k}} \ , \tag{3.1}$$

where the single-particle wave functions $\phi_{\lambda,\mathbf{k}}(\mathbf{r})$ describe Bloch electrons in band λ with wave vector $\mathbf{k}$ that are eigenstates of the crystal Hamiltonian

$$\left[\frac{\mathbf{p}^2}{2m} + U(\mathbf{r})\right] \phi_{\lambda,\mathbf{k}}(\mathbf{r}) = E_{\lambda,\mathbf{k}} \phi_{\lambda,\mathbf{k}}(\mathbf{r}) \ , \tag{3.2}$$

with the band structure $E_{\lambda,\mathbf{k}}$. The single-particle states obey the Bloch theorem [39]

$$\phi_{\lambda,\mathbf{k}}(\mathbf{r}) = \frac{1}{\sqrt{\mathcal{S}}} \mathrm{e}^{\mathrm{i}\mathbf{k}\cdot\mathbf{r}} u_{\lambda,\mathbf{k}}(\mathbf{r}) \ , \tag{3.3}$$

with quantization volume $\mathcal{S}$ and lattice periodic functions $u_{\lambda,\mathbf{k}}(\mathbf{r})$. The fermionic creation and annihilation operators ($a^\dagger_{\lambda,\mathbf{k}}$ and $a_{\lambda,\mathbf{k}}$) create and annihilate an electron in the state $\phi_{\lambda,\mathbf{k}}(\mathbf{r})$, respectively.

3.3.2 Hamiltonian and matrix elements

The Hamiltonian (2.2) in second quantization can be computed by inserting the field operators defined in Eq. (3.1) into Eq. (2.3), resulting in

$$\begin{aligned} \hat{H}_{\text{lightwave}} = &\sum_{\lambda,\mathbf{k}} a^\dagger_{\lambda,\mathbf{k}} \big[E_{\lambda,\mathbf{k}} + |e|\big(\mathrm{i}\nabla_{\mathbf{k}} + \boldsymbol{\mathcal{A}}^\lambda_{\mathbf{k}}\big)\cdot\mathbf{E}(t)\big] a_{\lambda,\mathbf{k}} - \sum_{\lambda\neq\nu}\sum_{\mathbf{k}} a^\dagger_{\lambda,\mathbf{k}} a_{\nu,\mathbf{k}} \mathbf{d}^{\lambda,\nu}_{\mathbf{k}}\cdot\mathbf{E}(t) \\ &+ \frac{1}{2}\sum_{\lambda,\nu,\nu',\lambda'}\sum_{\mathbf{k},\mathbf{k}',\mathbf{q}} V^{\lambda,\nu,\nu',\lambda'}_{\mathbf{k},\mathbf{k}',\mathbf{q}} a^\dagger_{\lambda,\mathbf{k}} a^\dagger_{\nu,\mathbf{k}'} a_{\nu',\mathbf{k}'+\mathbf{q}} a_{\lambda',\mathbf{k}-\mathbf{q}} \ , \end{aligned} \tag{3.4}$$

where phonon contributions have been neglected and the electric field is assumed to be classical. Also, the separation of length scales [41] was applied by assuming that quantities like the electric field change slowly within the unit cell. The dipole matrix elements, Berry connection, and Coulomb matrix elements are identified as

$$\mathbf{d}_{\mathbf{k}}^{\lambda,\nu} \equiv -\langle \lambda, \mathbf{k}||e|\mathbf{r}|\nu, \mathbf{k}\rangle \ , \tag{3.5}$$

$$\boldsymbol{\mathcal{A}}_{\mathbf{k}}^{\lambda} \equiv \langle \lambda, \mathbf{k}|\mathrm{i}\boldsymbol{\nabla}_{\mathbf{k}}|\lambda, \mathbf{k}\rangle \ , \tag{3.6}$$

$$V_{\mathbf{k},\mathbf{k}',\mathbf{q}}^{\lambda,\nu,\nu',\lambda'} \equiv V_{\mathbf{q}} \langle \lambda, \mathbf{k}|\lambda', \mathbf{k}-\mathbf{q}\rangle \langle \nu, \mathbf{k}'|\nu', \mathbf{k}'+\mathbf{q}\rangle \ , \tag{3.7}$$

respectively, where the abstract notation

$$\langle \lambda, \mathbf{k}|\hat{O}|\nu, \mathbf{k}'\rangle \equiv \frac{1}{\Omega_0}\int_{\Omega_0} \mathrm{d}^2 r \, u_{\lambda,\mathbf{k}}^*(\mathbf{r}) O(\mathbf{r}) u_{\nu,\mathbf{k}'}(\mathbf{r}) \tag{3.8}$$

defines matrix elements from integrals over the is the unit cell area Ω_0. The Coulomb matrix elements contain the Fourier transformation

$$V_{\mathbf{q}} = \frac{1}{\mathcal{N}} \sum_{\mathbf{R}} \mathrm{e}^{-\mathrm{i}\mathbf{q}\cdot\mathbf{R}} V(\mathbf{R}) \ , \tag{3.9}$$

of the Coulomb potential $V(\mathbf{r})$. In the envelope-function approximation, the momentum representation of the Coulomb interaction $V_{\mathbf{q}}$ no longer resembles the 3D Coulomb interaction because of quantum confinement [41]. To describe the Coulomb interaction of 2D TMDs, we use the Keldysh potential [85, 86]

$$V_{\mathbf{q}}^{\text{Keldysh}} = \frac{|e|^2}{2\varepsilon_0 \varepsilon_r(\mathbf{q}) \mathcal{S}} \frac{1}{|\mathbf{q}|} \ , \quad \text{with} \quad \varepsilon_r(\mathbf{q}) = \frac{\varepsilon_1^r + \varepsilon_2^r}{2}(1 + \rho_0|\mathbf{q}|) \ , \tag{3.10}$$

where ε_1^r and ε_2^r are the relative permittivities of the materials surrounding the TMD on either side, ε_0 is the vacuum permittivity, and ρ_0 is a material parameter that relates to an effective thickness of the TMD.

3.4 Equations of motion

3.4.1 Semiconductor Bloch equations

The singlets $P_{\mathbf{k}}^{\lambda,\nu} \equiv \left\langle a_{\lambda,\mathbf{k}}^{\dagger} a_{\nu,\mathbf{k}} \right\rangle$ are the relevant quantities that describe classical excitations of solids and we assume an implicit time dependence $P_{\mathbf{k}}^{\lambda,\nu} = P_{\mathbf{k}}^{\lambda,\nu}(t)$ for these expectation values unless stated otherwise. The diagonal elements ($\lambda = \nu$) describe the occupation of the electronic state with momentum $\mathbf{k}$ in band λ, the off-diagonal elements ($\lambda \neq \nu$) are microscopic polarizations which describe coherent excitations between two bands λ and ν.

Solids contain an infinite number of bands λ. However, a theoretical description can often be limited to a finite number of bands that are relevant for the studied processes. If n bands are considered, the singlet state of the system would be described by n occupations and $n(n-1)/2$ microscopic polarizations. The equations of motions for these singlets can be computed from the Heisenberg equation of motion (2.4) and are detailed in Appendix A for a general n-band system. Here, we consider a two-band system with one valence ($\lambda = v$) and one conduction band ($\lambda = c$) to simplify the discussion. In the electron–hole picture, this leads to three singlet quantities which we refer to as the microscopic polarization

$$P_{\mathbf{k}} \equiv P_{\mathbf{k}}^{v,c} \,, \tag{3.11}$$

and the electron and hole occupations

$$f_{\mathbf{k}}^{\mathrm{e}} \equiv P_{\mathbf{k}}^{c,c} \,, \quad f_{\mathbf{k}}^{\mathrm{h}} \equiv 1 - P_{\mathbf{k}}^{v,v} \,, \tag{3.12}$$

respectively. The equations of motion describing their dynamics, known as the semiconductor

Bloch equations (SBEs), are

$$\mathrm{i}\hbar\frac{\partial}{\partial t}P_{\mathbf{k}} = \Big[\widetilde{E}^{\mathrm{eh}}_{\mathbf{k}} + \mathrm{i}|e|\mathbf{E}(t)\cdot\big(\nabla_{\mathbf{k}} - \mathrm{i}\boldsymbol{\mathcal{A}}^{\mathrm{eh}}_{\mathbf{k}}\big)\Big]P_{\mathbf{k}} - \big[1 - f^{\mathrm{e}}_{\mathbf{k}} - f^{\mathrm{h}}_{\mathbf{k}}\big]\Omega_{\mathbf{k}}(t) + \Gamma_{\mathbf{k}}\ , \tag{3.13a}$$

$$\hbar\frac{\partial}{\partial t}f^{\mathrm{e/h}}_{\mathbf{k}} = 2\mathrm{Im}[\Omega^{*}_{\mathbf{k}}(t)P_{\mathbf{k}}] + |e|\mathbf{E}(t)\cdot\nabla_{\mathbf{k}}f^{\mathrm{e/h}}_{\mathbf{k}} + \Gamma^{\mathrm{e/h}}_{\mathbf{k}}\ , \tag{3.13b}$$

for which a spatially homogeneous system was assumed by applying the random-phase approximation [69]. We identify the renormalized kinetic energy

$$\widetilde{E}^{\mathrm{eh}}_{\mathbf{k}} \equiv E^{\mathrm{eh}}_{\mathbf{k}} - \sum_{\mathbf{k}'}\left(V^{c,c}_{\mathbf{k},\mathbf{k}'}f^{\mathrm{e}}_{\mathbf{k}} + V^{v,v}_{\mathbf{k},\mathbf{k}'}f^{\mathrm{h}}_{\mathbf{k}'}\right)\ , \tag{3.14}$$

with the free electron–hole energy $E^{\mathrm{eh}}_{\mathbf{k}} \equiv E_{c,\mathbf{k}} - E_{v,\mathbf{k}}$ and Coulomb matrix elements $V^{\lambda,\nu}_{\mathbf{k},\mathbf{k}'} \equiv V^{\lambda,\nu,\nu,\lambda}_{\mathbf{k},\mathbf{k}',\mathbf{k}-\mathbf{k}'}$, and the renormalized Rabi energy

$$\Omega_{\mathbf{k}}(t) \equiv \mathbf{d}^{c,v}_{\mathbf{k}}\cdot\mathbf{E}(t) + \sum_{\mathbf{k}'}V^{c,v}_{\mathbf{k},\mathbf{k}'}P_{\mathbf{k}'}\ , \tag{3.15}$$

with the self-consistently coupled electric field $\mathbf{E}(t)$. We further define $\boldsymbol{\mathcal{A}}^{\mathrm{eh}}_{\mathbf{k}} \equiv \boldsymbol{\mathcal{A}}^{c}_{\mathbf{k}} - \boldsymbol{\mathcal{A}}^{v}_{\mathbf{k}}$ and collect all doublet terms in $\Gamma_{\mathbf{k}}$, $\Gamma^{\mathrm{e}}_{\mathbf{k}}$, and $\Gamma^{\mathrm{h}}_{\mathbf{k}}$, respectively, which produce microscopic scattering [70, 87].

3.4.2 Optical response

The optical response of a semiconductor can be computed self consistently by coupling Maxwell's equations (describing the dynamics of classical light) to the SBEs (describing the dynamics of the semiconductor). Formally, Maxwell's equations can be derived from the Hamiltonian (2.2) by computing the Heisenberg equations of motion for bosonic phonon operators $\left\langle\hat{b}\right\rangle$ and identifying the electric field. Here, we will only use the results and refer the reader to Refs. [41, 65, 70] for details.

For a two-dimensional quantum material situated at $z = 0$ and embedded by a dielectric

environment with refractive index $n(z)$, the electric field is described by the wave equation

$$\left(\frac{\partial^2}{\partial z^2} - \frac{n^2(z)}{c_0^2}\frac{\partial^2}{\partial t^2}\right)\mathbf{E}(z,t) = -\mu_0\delta(z)\frac{\partial}{\partial t}\mathbf{J}(t) \,, \tag{3.16}$$

where plane waves travelling in the z direction and an optically thin semiconductor (thickness much smaller than the wave length of light) are assumed. The semiconductor excitations couple to the light field via the macroscopic current density

$$\mathbf{J}(t) = -\frac{\partial}{\partial t}\mathbf{P}^{\text{inter}}(t) + \mathbf{J}^{\text{intra}}(t) + \mathbf{J}[\Delta\langle 2\rangle] \,, \tag{3.17}$$

which can be split into interband currents from the macroscopic polarization

$$\mathbf{P}^{\text{inter}}(t) = \frac{1}{\mathcal{S}}\sum_{\mathbf{k}} \mathbf{d}_{\mathbf{k}}^{v,c} P_{\mathbf{k}} \,, \tag{3.18}$$

intraband currents $\mathbf{J}^{\text{intra}}(t)$, as well as contributions from doublets $\mathbf{J}[\Delta\langle 2\rangle]$ (see Appendix B for details). In this Thesis, we focus on coherent processes such as harmonic sideband generation which are dominated by interband emission. Intraband currents can easily be included in the dynamics and become important in high-harmonic generation, for example.

The wave equation (3.16) can be solved analytically when assuming the refractive index to be constant with value n_1 for $z < 0$ and n_2 for $z > 0$. In other words, when the quantum material is surrounded by materials with constant refractive indices as illustrated in Fig 3.1. In an experimental setup, this could describe a TMD on a substrate without encapsulation ($n_1 = 1$, $n_2 > 1$). For an electric field $\mathbf{E}_{\text{in}}(t)$ that approaches the quantum material from the left with perpendicular incident, the transmitted and reflected fields at the quantum-material position are then given by

$$\mathbf{E}_{\text{T}}(t) = \frac{2n_1}{n_1+n_2}\mathbf{E}_{\text{in}}(t) - \frac{\mu_0 c_0}{n_1+n_2}\frac{\partial}{\partial t}\mathbf{P}^{\text{inter}}(t) \,, \tag{3.19a}$$

$$\mathbf{E}_{\text{R}}(t) = -\frac{n_2-n_1}{n_1+n_2}\mathbf{E}_{\text{in}}(t) - \frac{\mu_0 c_0}{n_1+n_2}\frac{\partial}{\partial t}\mathbf{P}^{\text{inter}}(t) \,, \tag{3.19b}$$

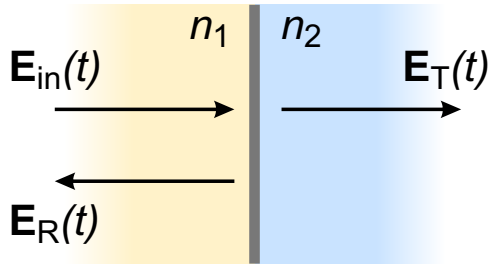

Figure 3.1: Self-consistent electric field for a optically thin quantum material surrounded by dielectric materials. The quantum material (gray line) is surrounded by materials with refractive indices n_1 and n_2 and is excited by the incident electric field $\mathbf{E}_{\mathrm{in}}(t)$. $\mathbf{E}_{\mathrm{R}}(t)$ and $\mathbf{E}_{\mathrm{R}}(t)$ are the reflected and transmitted electric fields at the position of the quantum material, respectively.

respectively. The actual field exciting the quantum material and entering the SBEs is $\mathbf{E}(t) = \mathbf{E}_{\mathrm{T}}(t)$ and contains both the incident field and the field radiated by the quantum material itself. In later chapters, we also separately study the field

$$\mathbf{E}_{\mathrm{rad}} \equiv -\frac{\mu_0 c_0}{n_1 + n_2} \frac{\partial}{\partial t} \mathbf{P}^{\mathrm{inter}}(t) \, , \tag{3.20}$$

that is radiated by the material.

Reflection and transmission spectra are connected to the fields (3.19) by a Fourier transformation $\mathbf{E}(f) = \int \mathrm{d}t \, \mathbf{E}(t) \mathrm{e}^{2\pi \mathrm{i} f t}$ with frequency f, and intensity spectra are given by $I(f) = |\mathbf{E}(f)|^2$. Later chapters analyze frequency regions for which the incident field $\mathbf{E}_{\mathrm{in}}(f)$ is negligibly small compared to the radiated field $\mathbf{E}_{\mathrm{rad}}(f)$. In those cases, the intensity spectra can be computed from

$$I(f) \propto \left| f \, \mathbf{P}^{\mathrm{inter}}(f) \right|^2 , \tag{3.21}$$

where $\mathbf{P}^{\mathrm{inter}}(f)$ is the Fourier transformation of $\mathbf{P}^{\mathrm{inter}}(t)$. The wave equation (3.16) can also be solved straightforwardly for more complex dielectric structures $n(z)$ using the transfer-matrix approach [41, 88] and be extended to include multiple coupled quantum-material layers and different excitation geometries.

3.4.3 Doublet contributions and microscopic scattering

As discussed in Chapter 2, classical light first excites singlets ($P_{\mathbf{k}}$, $f^{\mathrm{e}}_{\mathbf{k}}$, and $f^{\mathrm{h}}_{\mathbf{k}}$, see Reference [70]). Once these are formed, scattering among the singlets creates two-particle correlations, doublets, which couple back to the singlet dynamics via $\Gamma_{\mathbf{k}}$, $\Gamma^{\mathrm{e}}_{\mathbf{k}}$, and $\Gamma^{\mathrm{h}}_{\mathbf{k}}$ and create a microscopic scattering. Phenomenologically, the effects of doublets are observed as excitation-induced dephasing for $P_{\mathbf{k}}$ and carrier relaxation for $f^{\mathrm{e/h}}_{\mathbf{k}}$ [41, 70].

In this thesis, we are interested in the ultrafast coherent dynamics that unfolds on time scales where singlets dominate and doublets just start forming. Instead of solving the doublets dynamically alongside the singlets (which would significantly increase the computational complexity), we carefully analyze the doublet dynamics and microscopic scattering. The two most important aspects of a realistic microscopic scattering (a diffusive character and quantum memory) are discussed in the following two sections and combined into an effective microscopic scattering model.

Diffusive scattering

The doublet contributions to $P_{\mathbf{k}}$ collected in the scattering term $\Gamma_{\mathbf{k}}$ in the SBE (3.13a) satisfies the conservation law [70]

$$\sum_{\mathbf{k}} \Gamma_{\mathbf{k}} = 0 \,, \tag{3.22}$$

and shows that Coulomb scattering has a diffusive character that alone conserves the microscopic polarization. A phenomenological dephasing $\Gamma_{\mathbf{k}} = -\mathrm{i}\gamma P_{\mathbf{k}}$ that is often applied clearly violates this conservation. To mimic the diffusive character, we apply a diffusive scattering model

$$\Gamma_{\mathbf{k}} = -\mathrm{i}\left[\gamma^{(1)}_{\mathbf{k}} P_{\mathbf{k}} - \sum_{\mathbf{k}'} \gamma^{(2)}_{\mathbf{k},\mathbf{k}'} P_{\mathbf{k}'}\right] , \quad \gamma^{(1)}_{\mathbf{k}} = \sum_{\mathbf{k}'} \gamma^{(2)}_{\mathbf{k},\mathbf{k}'} \,, \tag{3.23}$$

which satisfies Eq. (3.22) by definition. For the scattering kernel, we choose a Gaussian form

$$\gamma^{(2)}_{\mathbf{k},\mathbf{k}'} = \gamma \mathrm{e}^{-|\mathbf{k}-\mathbf{k}'|^2/\Delta K^2} \ . \tag{3.24}$$

This creates a state-dependent dephasing which is an important aspect of excitation-induced dephasing (EID) and crucial in the context of lightwave excitations. Because lightwave driving rapidly changes the microscopic state of the system, the effective dephasing becomes strongly time-dependent. The intricacies of this temporal dephasing cannot be captured by a simple phenomenological dephasing constant. The parameters γ and ΔK of the diffusive scattering model used in this work were deduced from fully microscopically computed scattering matrices [89].

Quantum memory

The formation of doublets and the subsequent emergence of dephasing takes time because of the sequential build-up of correlations discussed in Section 2. A careful analysis of the build up of scattering led to the development of the quantum-memory model detailed in Ref. [87]. Its name originates from the fact that dephasing is dependent on the history of the system at earlier times which results in a frequency-dependent dephasing. It becomes particularly important in the description of off-resonant excitations as it greatly reduces the tail of absorption lines which for a constant dephasing would have Lorentzian shapes [41].

Scattering model for monolayer TMDs

In our computations, we combine the diffusive scattering with a quantum-memory model to describe the Coulomb scattering. At room temperature, phonon-induced dephasing occurs which we take into account by adding an extra $\mathbf{k}$-dependent dephasing to the quantum-memory kernel. The scattering model used in our computations is detailed in Appendix C.

3.5 Interband excitation vs lightwave driving

The electric field enters the SBEs in two places. The first appearance is in the renormalized Rabi energy (3.15) where the electric field couples via the dipole matrix elements $\mathbf{d}_{\mathbf{k}}^{c,v}$ and creates excitations between the valence and conduction band [41]. These so called interband excitations are the dominant process of resonant excitations. The electric field also appears in connection with gradients of the form

$$\frac{\partial}{\partial t} s_{\mathbf{k}}(t) = \frac{|e|}{\hbar} \mathbf{E}(t) \cdot \nabla_{\mathbf{k}} s_{\mathbf{k}}(t) \ , \tag{3.25}$$

for all singlet quantities $s_{\mathbf{k}} \in \left\{ P_{\mathbf{k}}, f_{\mathbf{k}}^{\mathrm{e}}, f_{\mathbf{k}}^{\mathrm{h}} \right\}$. Equation (3.25) is solved by

$$s_{\mathbf{k}}(t) = s_{\mathbf{k} - \frac{|e|}{\hbar}\mathbf{A}(t)}(t_0) \ , \ \text{with} \quad \mathbf{A}(t) = -\int_{t_0}^{t} \mathrm{d}\tau \, \mathbf{E}(\tau) \ , \tag{3.26}$$

which is a simple translation of $s_{\mathbf{k}}$ in momentum space that is equivalent to the acceleration theorem of Bloch electrons in solids [39, 90]. We refer to these light-induced translations as lightwave or intraband driving.

For a sinusoidal field $\mathbf{E}(t) = \hat{\mathbf{e}} E_0 \cos(2\pi f t)$ with frequency f and peak electric field E_0 in the direction $\hat{\mathbf{e}}$, singlets are translated in momentum space by

$$\mathbf{k}(t) = \frac{|e| \mathbf{E}_0}{hf} \sin(2\pi f t) \ , \tag{3.27}$$

resulting in a sinusoidal motion in the direction of the electric field with amplitude $\frac{|e|E_0}{hf}$. From Eq. (3.27) follows that the oscillation amplitude increases with increasing peak field strength or decreasing driving frequency.

For TMD materials with optical gaps, typical resonant excitations efficiently create interband transitions, but create negligible lightwave driving. In contrast, low frequency, off-resonant fields can create considerable lightwave driving without inducing substantial interband transitions. At the most extreme excitation strengths, both processes can occur for

both resonant and off-resonant frequencies. However, such conditions are not considered in this Thesis.

3.6 *Ab initio* matrix elements

The single-particle states $\phi_{\lambda,\mathbf{k}}(\mathbf{r})$ defined in Eq. (3.1) are needed to explicitly compute matrix elements and solve the SBEs for realistic materials. Density-functional theory [82–84] is an *ab initio* approach to solve $\phi_{\lambda,\mathbf{k}}(\mathbf{r})$ on the full Brillouin zone for any given crystal structure. However, calculations are usually performed on $\mathbf{k}$ grids that are much coarser than what is required to solve the SBEs. Solving DFT on dense $\mathbf{k}$ grids is possible, but numerically expensive. Maximally localized Wannier functions [91, 92] as implemented by the wannier90 code [93] can be used to map DFT computations onto a tight-binding (TB) model to interpolate DFT results at arbitrary $\mathbf{k}$.

The subsequent sections introduce the tight-binding formalism and show how a tight-binding model can be constructed from a DFT calculation. We then derive all matrix elements that are needed in the SBEs from the tight-binding model and elaborate how the gauge freedom in the $\mathbf{k}$-dependent phase of the single-particle states can be settled to recover smooth and differentiable matrix elements.

3.6.1 Tight-binding model

A detailed introduction of the tight-binding model can be found, for example, in Reference [5]. In this Section, I summarize the key equations and ideas that are needed for the subsequent explicit computation of microscopic matrix elements.

In a tight-binding model, the single-particle wave functions are approximated as a linear combination of atomic orbitals (LCAO)

$$\psi_{\alpha,\mathbf{k}}(\mathbf{r}) = \frac{1}{\sqrt{N}} \sum_{\mathbf{R}} \mathrm{e}^{\mathrm{i}\mathbf{k}\cdot\mathbf{R}} \varphi_\alpha(\mathbf{r}-\mathbf{R}) \,, \tag{3.28}$$

with atomic orbitals $\varphi_\alpha(\mathbf{r})$, number of sites N, and lattice vectors $\mathbf{R}$. The LCAO states satisfy the Bloch theorem

$$\psi_{\alpha,\mathbf{k}}(\mathbf{r}+\mathbf{R}) = \mathrm{e}^{\mathrm{i}\mathbf{k}\cdot\mathbf{R}}\psi_{\alpha,\mathbf{k}}(\mathbf{r}) \ , \tag{3.29}$$

and are used to obtain the tight-binding Hamiltonian by expressing the crystal Hamiltonian in the LCAO basis

$$\begin{aligned} H_{\alpha,\beta}(\mathbf{k}) &\equiv \int \mathrm{d}\mathbf{r}\, \psi^*_{\alpha,\mathbf{k}}(\mathbf{r})\hat{H}(\mathbf{r})\psi_{\beta,\mathbf{k}}(\mathbf{r}) \\ &= \sum_{\mathbf{R}} \mathrm{e}^{\mathrm{i}\mathbf{k}\cdot\mathbf{R}} \int \mathrm{d}\mathbf{r}\, \varphi^*_\alpha(\mathbf{r})H(\mathbf{r})\varphi_\beta(\mathbf{r}-\mathbf{R}) \\ &= \sum_{\mathbf{R}} \mathrm{e}^{\mathrm{i}\mathbf{k}\cdot\mathbf{R}} \langle \alpha, \mathbf{0}|\hat{H}|\beta, \mathbf{R}\rangle \ , \end{aligned} \tag{3.30}$$

where we introduced the abstract notation $\varphi_\alpha(\mathbf{r}-\mathbf{R}) = \langle \mathbf{r}|\alpha, \mathbf{R}\rangle$.

3.6.2 Tight-binding Hamiltonian from DFT

The tight-binding Hamiltonian can be directly constructed from a DFT calculation using the wannier90 code. It generates maximally localized Wannier functions that act as the atomic orbitals $\varphi_\alpha(\mathbf{r})$ in (3.28). Conveniently, the wannier90 code directly generates outputs of the matrix elements $\langle \alpha, \mathbf{0}|\hat{H}|\beta, \mathbf{R}\rangle$ to be used in Eq. (3.30).

The Wannier functions are constructed from a subset of the DFT states which allows for downfolding and reduction of the number of bands to a subset relevant for the dynamics. This process, also referred to as Wannier interpolation [94], is a standard tool in the DFT community and we refer the reader to References [94, 95] for details.

3.6.3 Single particle eigenstates and electronic bands

The single-particle eigenstates $|\phi_{\lambda,\mathbf{k}}\rangle$ and eigenenergies $E_{\lambda,\mathbf{k}}$ that form the band structure result from the eigenvalue problem

$$\hat{H}\,|\phi_{\lambda,\mathbf{k}}\rangle = E_{\lambda,\mathbf{k}}\,|\phi_{\lambda,\mathbf{k}}\rangle \ . \tag{3.31}$$

In the LCAO basis, this is equivalent to diagonalization of the TB Hamiltonian $H_{\alpha,\beta}(\mathbf{k})$ which can be efficiently performed numerically for each desired $\mathbf{k}$ point. The resulting eigenvectors $c_\alpha^\lambda(\mathbf{k})$, defined by

$$\sum_\beta H_{\alpha,\beta}(\mathbf{k}) c_\beta^\lambda(\mathbf{k}) = E_{\lambda,\mathbf{k}} c_\alpha^\lambda(\mathbf{k}) \ , \tag{3.32}$$

expand the eigenstates

$$\begin{aligned} \phi_{\lambda,\mathbf{k}}(\mathbf{r}) &= \sum_\alpha c_\alpha^\lambda(\mathbf{k}) \psi_{\alpha,\mathbf{k}}(\mathbf{r}) \\ &= \frac{1}{\sqrt{N}} \sum_\alpha c_\alpha^\lambda(\mathbf{k}) \sum_{\mathbf{R}} \mathrm{e}^{\mathrm{i}\mathbf{k}\cdot\mathbf{R}} \varphi_\alpha(\mathbf{r}-\mathbf{R}) \ , \end{aligned} \tag{3.33}$$

in the LCAO basis. Later, we will also use

$$\phi_{\lambda,\mathbf{k}}(\mathbf{r}) = \frac{1}{\sqrt{N}} \mathrm{e}^{\mathrm{i}\mathbf{k}\cdot\mathbf{r}} u_{\lambda,\mathbf{k}}(\mathbf{r}) \ , \tag{3.34}$$

with the lattice periodic wave functions

$$u_{\lambda,\mathbf{k}}(\mathbf{r}) = \sum_\alpha c_\alpha^\lambda(\mathbf{k}) \sum_{\mathbf{R}} \mathrm{e}^{\mathrm{i}\mathbf{k}\cdot(\mathbf{R}-\mathbf{r})} \varphi_\alpha(\mathbf{r}-\mathbf{R}) \ , \tag{3.35}$$

which are orthogonal when integrated over the unit cell with area Ω_0:

$$\langle \lambda,\mathbf{k}|\mu,\mathbf{k}\rangle \equiv \frac{1}{\Omega_0} \int_{\Omega_0} \mathrm{d}^2 r \, u_{\lambda,\mathbf{k}}^*(\mathbf{r}) u_{\mu,\mathbf{k}}(\mathbf{r}) = \delta_{\lambda,\mu} \ . \tag{3.36}$$

3.6.4 Coulomb matrix elements

The Coulomb matrix elements

$$V^{\lambda,\nu}_{\mathbf{k},\mathbf{k}'} = V_{\mathbf{k}-\mathbf{k}'} \langle \lambda, \mathbf{k} | \lambda, \mathbf{k}' \rangle \langle \nu, \mathbf{k}' | \nu, \mathbf{k} \rangle \tag{3.37}$$

require evaluation of the overlap integrals

$$\langle \lambda, \mathbf{k} | \nu, \mathbf{k}' \rangle = \sum_{\alpha,\beta} \left[c^{\lambda}_{\alpha}(\mathbf{k}) \right]^* c^{\nu}_{\beta}(\mathbf{k}') \sum_{\mathbf{R}} \mathrm{e}^{-\mathrm{i}\mathbf{k}\cdot\mathbf{R}} \int \mathrm{d}^2 r \, \mathrm{e}^{-\mathrm{i}(\mathbf{k}-\mathbf{k}')\cdot\mathbf{r}} \varphi^*_{\alpha}(\mathbf{r}-\mathbf{R}) \varphi_{\beta}(\mathbf{r}) \, . \tag{3.38}$$

We approximate $\int \mathrm{d}^2 r \, \mathrm{e}^{-\mathrm{i}(\mathbf{k}-\mathbf{k}')\cdot\mathbf{r}} \varphi^*_{\alpha}(\mathbf{r}-\mathbf{R}) \varphi_{\beta}(\mathbf{r}) \approx \delta_{\mathbf{R},\mathbf{0}} \delta_{\alpha,\beta}$ which is motivated by $\varphi_{\alpha}(\mathbf{r})$ being localized wave functions that have their largest overlap for $\mathbf{R} = 0$. This approximation is best for small $|\mathbf{k}-\mathbf{k}'|$. However, at large $|\mathbf{k}-\mathbf{k}'|$ where the approximation fails, the Coulomb potential $V_{\mathbf{k}-\mathbf{k}'}$ becomes small which renders the precise value of the integral less important. As a result, the overlaps are well approximated by

$$\langle \lambda, \mathbf{k} | \nu, \mathbf{k}' \rangle \approx \sum_{\alpha} \left[c^{\lambda}_{\alpha}(\mathbf{k}) \right]^* c^{\nu}_{\alpha}(\mathbf{k}') \, , \tag{3.39}$$

which yields the tight-binding Coulomb matrix elements

$$V^{\lambda,\lambda'}_{\mathbf{k},\mathbf{k}'} \Big|_{\mathrm{TB}} = V_{\mathbf{k}-\mathbf{k}'} \sum_{\alpha} \left[c^{\lambda}_{\alpha}(\mathbf{k}) \right]^* c^{\lambda}_{\alpha}(\mathbf{k}') \sum_{\beta} \left[c^{\nu}_{\beta}(\mathbf{k}') \right]^* c^{\nu}_{\beta}(\mathbf{k}) \, . \tag{3.40}$$

3.6.5 Dipole matrix elements

To compute the dipole matrix elements defined in Eq. (3.5), we use the so called Peierls approximation. Technically, it applies the generalized Feynman–Hellman theorem [96] to represent the dipole matrix elements exactly as

$$\mathbf{d}^{\lambda,\nu}_{\mathbf{k}} = -\frac{\mathrm{i}|e|}{E_{\nu}(\mathbf{k}) - E_{\lambda}(\mathbf{k})} \langle \lambda, \mathbf{k} | \nabla_{\mathbf{k}} H(\mathbf{k}) | \nu, \mathbf{k} \rangle \, . \tag{3.41}$$

When inserting the tight-binding states (3.35), the tight-binding dipole can be approximated as

$$\mathbf{d}^{\lambda,\nu}_{\mathbf{k},\mathbf{k}'}\Big|_{\mathrm{TB}} = \frac{\mathrm{i}|e|}{E_{\nu\mathbf{k}} - E_{\lambda\mathbf{k}}} \sum_{\alpha,\beta} \left[c^{\lambda}_{\alpha}(\mathbf{k})\right]^{*} c^{\nu}_{\beta}(\mathbf{k}) \nabla_{\mathbf{k}} H^{\alpha,\beta}(\mathbf{k}) \;, \tag{3.42}$$

which neglects terms that contain gradients of the LCAO states $\psi_{\alpha,\mathbf{k}}(\mathbf{r})$.

3.6.6 Berry connection

The Berry connection (3.6) is defined based on gradients of the lattice-periodic functions (3.35). We use an approach that is based on finite-differences to compute the Berry connection numerically on a discrete grid.

For an infinitesimal δ and unit vector $\hat{\mathbf{e}}$, one finds [95]

$$\hat{\mathbf{e}} \cdot \boldsymbol{\mathcal{A}}^{\lambda}_{\mathbf{k}} = -\mathrm{Im}\,\langle \lambda, \mathbf{k} | \hat{\mathbf{e}} \cdot \nabla_{\mathbf{k}} | \lambda, \mathbf{k} \rangle = -\frac{1}{\delta} \mathrm{Im}\ln \langle \lambda, \mathbf{k} | \lambda, \mathbf{k} + \delta\hat{\mathbf{e}} \rangle \;\; . \tag{3.43}$$

Based on this relation, the tight-binding Berry connection along $\hat{\mathbf{e}}$-direction can be approximated as

$$\hat{\mathbf{e}} \cdot \boldsymbol{\mathcal{A}}^{\lambda}_{\mathbf{k}}\Big|_{\mathrm{TB}} = -\frac{1}{\delta} \mathrm{Im}\ln \left(\sum_{\alpha} \left[c^{\lambda}_{\alpha}(\mathbf{k})\right]^{*} c^{\lambda}_{\alpha}(\mathbf{k} + \delta\hat{\mathbf{e}}) \right) \tag{3.44}$$

if we assume $\mathbf{k}$ and $\mathbf{k} + \delta\hat{\mathbf{e}}$ to be two neighboring points of a discrete grid with a finite δ. To derive this expression, similar approximations to $\langle \lambda, \mathbf{k} | \lambda, \mathbf{k}' \rangle$ as in Section 3.6.4 for the Coulomb matrix elements have been applied. Equation (3.44) can easily evaluate the Berry connection along the direction of the vectors spanning the discrete grid. In general, these are not orthogonal. However, computing the Berry connection in two directions that are not collinear is sufficient to construct the full vectorial $\boldsymbol{\mathcal{A}}^{\lambda}_{\mathbf{k}}$.

3.6.7 Geometric gauge

The geometric gauge refers to a particular choice of phases of the eigenstates $u_{\lambda,\mathbf{k}}(\mathbf{r})$ which can be chosen freely [95]. Introducing a new set of states

$$\widetilde{u}_{\lambda,\mathbf{k}}(\mathbf{r}) = \mathrm{e}^{\mathrm{i}\theta_{\lambda,\mathbf{k}}} u_{\lambda,\mathbf{k}}(\mathbf{r}) \,, \tag{3.45}$$

changes the microscopic matrix elements. However, observables such as the interband polarization density in Eq. (3.18) remain invariant under such transformations of the geometric gauge. When the eigenproblem (3.32) is solved numerically, the phases assigned to the eigenstates are not physically motivated and can exhibit non-differentiable points as a function of $\mathbf{k}$. To make numerically computed eigenstates usable in the SBEs, the geometric gauge needs to be chosen such that the states $\widetilde{u}_{\lambda,\mathbf{k}}(\mathbf{r})$ are differentiable.

Finding a gauge transformation that makes states differentiable in all directions of the two-dimension Brillouin zone would be ideal. However, this is not generally possible [95]. Differentiability in one particular direction can be achieved by applying the twisted-parallel transport gauge as discussed in Ref. [95]. This is sufficient for the SBEs because they only contain gradients in a single direction at any given time (parallel to the electric field). Integrating the Berry connection along a slice in one direction across the whole Brillouin zone amounts to a finite Berry phase which is gauge invariant. The twisted-parallel transport gauge evenly spreads this phase across the slice, generating a constant Berry connection that is differentiable even across the periodic boundaries of the Brillouin zone. This can be repeated for all slices in the same direction until the whole two-dimensional Brillouin zone is covered. For linearly polarized light $\mathbf{E}$, the twisted-parallel transport gauge needs to be computed only once in the direction of the field. For more general fields, the gauge can also be adjusted dynamically [77], following the direction of the electric field as a function of time.

3.7 Numerical implementation

To describe lightwave-electronic excitations of TMDs, we solve the SBEs numerically on the full two-dimensional Brillouin zone in a moving frame

$$s_{\mathbf{k}}^{\mathrm{mov}}(t) \equiv s_{\mathbf{k}+\frac{|e|}{\hbar}\mathbf{A}(t)}(t) \;, \quad \text{with} \quad \mathbf{A}(t) = -\int_{-\infty}^{t} \mathrm{d}\tau\, \mathbf{E}(\tau) \;, \tag{3.46}$$

for all singlets $s_{\mathbf{k}} \in \left\{P_{\mathbf{k}}, f_{\mathbf{k}}^{\mathrm{e}}, f_{\mathbf{k}}^{\mathrm{h}}\right\}$, which eliminates the gradient terms in the SBEs. The two-dimensional Brillouin zone is discretized using a rhombic grid as described in Appendix D and all matrix elements are computed from *ab initio* methods as elaborated above. The resulting set of coupled ordinary differential equations is solved in time, starting from the ground state, using a the 4th order Runge-Kutta method [97]. We compute the dynamics on grids with up to $117 \times 117 = 13689$ $\mathbf{k}$ points and have verified that the numerical results are well converged at $69 \times 69 = 4761$ $\mathbf{k}$ points.

Chapter 4

Lightwave Tomography of Quantum Materials

This Chapter is in parts adapted from M. Borsch, C. P. Schmid, L. Weigl, S. Schlauderer, N. Hofmann, C. Lange, J. T. Steiner, S. W. Koch, R. Huber, and M. Kira, "Super-resolution lightwave tomography of electronic bands in quantum materials", Science **370**, 1204 (2020).

4.1 Introduction

The electronic band structure of quantum materials defines important material properties and is the foundation of quantum functionalities, including spin-valley, topological, and many-body effects. Characterization of the band structure is an important part in the discovery process to find new materials with quantum functionalities. The metaphorical gold standard to experimentally access band structures is set by angle-resolved photoemission spectroscopy (ARPES) [98–101]. Because it is based on detection of photoemitted electrons, it requires ultrahigh vacuum and is only sensitive close to the surface of materials. Buried materials such as quantum-well structures cannot be probed by ARPES because photoexcited electrons cannot pass undisturbed through the material, if at all. All-optical band-structure reconstruction based on high-harmonic generation has been proposed [102] as an alternative. It provided inspiration for experimental realizations [103–106] of this ap-

proach which is based on fitting experimentally measured spectra to computed spectra based on trial band structures to find the maximum agreement. A direct band-structure mapping is not possible because the strong light fields used to generate HH create excitations throughout the Brillouin zone that experience significant lightwave driving [52] as well as electronic interferences between multiple bands [56].

To overcome the limitations set by ARPES and HHG-based approaches, we developed super-resolution lightwave tomography. It is a new all-optical approach that directly connects the intensities of harmonic sidebands to the band structure via crystal-momentum combs and can be applied to microscopically small, atomically thin, or buried materials in situ without the need of ultra-high vacuum. In this Chapter, super-resolution lightwave tomography is introduced and the concept is demonstrated for monolayer WSe_2 in a detailed comparison between experiment and the QDCE theory developed in Chapter 3. In addition, the potential of tomography beyond the band structure to access dipole and Coulomb matrix elements is discussed.

4.2 Idea of lightwave tomography

Figure 4.1 shows the band structure of WSe_2 near its direct gap at the K point and illustrates the basic idea of lightwave band-structure reconstruction. A pair of bands (red lines) is selected by resonantly exciting (red wave) an electron–hole pair (blue and red spheres) between them. A strong off-resonant lightwave drives the excited coherence to a different wave vector $\mathbf{k}$ (blue and red arrow) where electron and hole can recombine and emit light at the respective gap energy (blue wave). By scanning $\mathbf{k}$ and recording the emitted photon energy, the energy gap could be reconstructed as function of the wave vector $\mathbf{k}$. However, two limitation are in the way of such a straightforward approach. First, lightwave sources with enough control to permanently move coherences to a specific $\mathbf{k}$ do not exist. Second, the dynamics and emission energy is complicated by many-body effects.

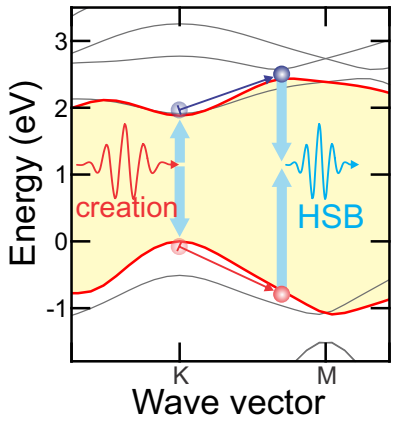

Figure 4.1: Idea of lightwave band-structure reconstruction. A resonant light pulse (red wave) generates an electron (blue sphere) and hole (red sphere) between two selected bands (red lines). A off-resonant lightwave then drives the charges to a different wave vector (blue and red arrows) where electron and hole recombine, emitting light in the form of harmonic sidebands (HSB, blue wave).

In our approach, we select the two red bands in Fig. 4.1 by resonantly exciting the $1s$-A exciton of monolayer WSe_2. The excited excitonic wave packet is described by the microscopic polarization $P_{\mathbf{k}}$ and is located at the K point where the gap energy between the two bands, $E^{\mathrm{eh}}_{\mathbf{k}}$, is minimized. The excited $P_{\mathbf{k}}$ is strongly localized in momentum space and oscillates with frequency f_{1s} where hf_{1s} is the energy of the $1s$ resonance. Figure 4.2 (bottom part at $t = 0$) shows a computed $P_{\mathbf{k}}$ as a color map on top of the electron–hole energy $E^{\mathrm{eh}}_{\mathbf{k}}$. A strong multi-terahertz (THz) field moves $P_{\mathbf{k}}$ on an approximately sinusoidal trajectory in momentum space (Fig. 4.2 at $t > 0$). The resulting increase in energy $E^{\mathrm{eh}}_{\mathbf{k}}$ when moving away from the minimum at the K point changes the frequency at which $P_{\mathbf{k}}$ oscillates and leads to emission of HSBs. In addition to a continued back-and-forth motion, $P_{\mathbf{k}}$ exhibits considerable spreading and interferences caused by many-body effects which does not allow for a simple reconstruction as proposed above. However, the combination of a narrow wave packet excited at the K point and driving along an almost sinusoidal path leads to the emergence of crystal-momentum combs which elegantly link the emission of HSBs to $E^{\mathrm{eh}}_{\mathbf{k}}$.

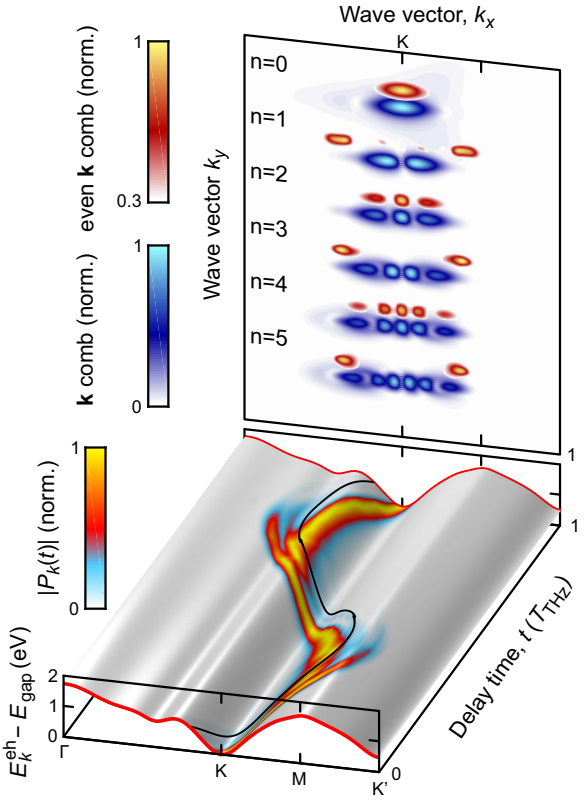

Figure 4.2: Lightwave dynamics and crystal-momentum combs. Bottom, computed dynamics of the microscopic polarization (color map, $|P_{\mathbf{k}}(t)|^2$) for a typical lightwave excitation generating harmonic sidebands (HSBs), projected onto the gray surface which shows the electron–hole energy $E_{\mathbf{k}}^{\mathrm{eh}}$ relative to the gap energy E_{gap} (red line). The black line indicates the vector potential of the lightwave with cycle length T_{THz}. Top, Comparison of crystal-momentum combs (**k** combs) (blue color map) with their even parts (red–yellow color map) for 0th to 5th order HSBs based on the dynamics shown below.

4.3 Crystal-momentum combs

To obtain the optical response of a semiconductor from the SBEs (see Section 3.4.2), we usually compute the dynamics of the microscopic polarization $P_{\mathbf{k}}(t)$ from which the macroscopic polarization $P(t) = \frac{1}{\mathcal{S}} \sum_{\mathbf{k}} d_{\mathbf{k}} P_{\mathbf{k}}(t)$ can be constructed. $P(t)$ is related to the light field emitted by coherent excitons as a function of time and a Fourier transformation yields the corresponding emission spectrum $I(f) \propto |fP(f)|^2$ with frequency f. Mathematically, the order of macroscopic sum (first) and Fourier transformation (second) can be switched and

we obtain

$$I(f) \propto \left| f \frac{1}{\mathcal{S}} \sum_{\mathbf{k}} d_{\mathbf{k}} p_{\mathbf{k}}(f) \right|^2 , \tag{4.1}$$

where

$$p_{\mathbf{k}}(f) \equiv \int \mathrm{d}t \, P_{\mathbf{k}}(t) \mathrm{e}^{2\pi \mathrm{i} f t} , \tag{4.2}$$

is the Fourier component of the microscopic polarization. It shows which $\mathbf{k}$ points in momentum space oscillate with frequency f and contribute to the emission of light with photon energy hf.

When the system is excited by a resonant pulse with frequency f_{opt} and a THz pulse with frequency f_{THz}, HSBs are expected at frequencies $f_n = f_{\mathrm{opt}} + n f_{\mathrm{THz}}$ for integer n. The blue colormap in Fig. 4.2 shows $|p_{\mathbf{k}}(f_n)|$ for $n = 0$ to 5 resulting from the dynamics shown underneath it. The emergence of very distinct interference patterns, the crystal-momentum combs, becomes clear when analyzing $P_{\mathbf{k}}(t) = P^{\mathrm{rot}}_{\mathbf{k}}(t) \mathrm{e}^{-2\pi \mathrm{i} f_{\mathrm{opt}} t}$ in the rotating frame which removes the excitation frequency f_{opt} from the oscillations of $P_{\mathbf{k}}(t)$.

In a reduced picture, a lightwave with field $\mathbf{E}_{\mathrm{THz}}$ simply translates $P^{\mathrm{rot}}_{\mathbf{k}}(t) = P^{\mathrm{rot}}_{\mathbf{k}(t)}$ by $\mathbf{k}(t) = \mathbf{k} - 2\pi \frac{|e|}{h} \int_{-\infty}^{t} \mathrm{d}t' \, \mathbf{E}_{\mathrm{THz}}(t')$ according to Eq. (3.26). For a Gaussian $P^{\mathrm{rot}}_{\mathbf{k}}$ and a sinusoidal driving field, the integral in Eq. (4.2) can be solved analytically and the resulting $p_{\mathbf{k}}(f_n)$ are shown for $n = 0$ to 6 in Fig. 4.3a. The $p_{\mathbf{k}}(f_n)$ exhibit the same structure of n nodes and $(n+1)$ peaks for the nth order as the $\mathbf{k}$-combs from the QDCE computation in Fig. 4.2, attesting that the reduced model captures the correct physics. Figure 4.3b illustrates how the $\mathbf{k}$-combs are generated on the example of the 5th order HSB. A wave packet $P^{\mathrm{rot}}_{\mathbf{k}}(t)$ following a sinusoidal translation (black line) crosses a given $\mathbf{k}$ value twice per THz cycle (sparks), each time creating a contribution to the integral in Eq. (4.2), which in the rotating

frame and for the 5th order HSB reads

$$p_{\mathbf{k}}(f_5) = \int \mathrm{d}t\, P^{\mathrm{rot}}_{\mathbf{k}}(t) \mathrm{e}^{2\pi \mathrm{i} * 5 \frac{t}{T_{\mathrm{THz}}}} \,. \tag{4.3}$$

These two contributions at times $t_1(\mathbf{k})$ and $t_2(\mathbf{k})$, which are $\mathbf{k}$ dependent, can be interpreted as independent polarization bursts that add up coherently with a relative phase between them which is defined by the spectrum-projecting kernel, $\mathrm{e}^{2\pi \mathrm{i} * 5 \frac{t}{T_{\mathrm{THz}}}}$ (red and blue oscillating lines). The latter oscillates five times faster than the $\mathbf{k}(t)$ trajectory with period $T_{\mathrm{THz}} = 1/f_{\mathrm{THz}}$. The peak and node structure is defined by the coherent addition of these two terms

$$\mathrm{e}^{2\pi \mathrm{i} * 5 \frac{t_1(\mathbf{k})}{T_{\mathrm{THz}}}} + \mathrm{e}^{2\pi \mathrm{i} * 5 \frac{t_2(\mathbf{k})}{T_{\mathrm{THz}}}} = \mathrm{e}^{2\pi \mathrm{i} * 5 \frac{t_1(\mathbf{k})}{T_{\mathrm{THz}}}} \left[1 + \mathrm{e}^{2\pi \mathrm{i} * 5 \frac{t_2(\mathbf{k}) - t_1(\mathbf{k})}{T_{\mathrm{THz}}}} \right] . \tag{4.4}$$

The time difference $\Delta t(\mathbf{k}) \equiv t_2(\mathbf{k}) - t_1(\mathbf{k})$ assumes values between 0 and T_{THz}, hence creating exactly 6 $\mathbf{k}$ points where the first and second burst are in phase, interfering constructively ($\Delta t(\mathbf{k}) = \frac{m}{5} T_{\mathrm{THz}}$), and 5 $\mathbf{k}$ values where the bursts are out of phase creating a node ($\Delta t(\mathbf{k}) = \frac{m+1/2}{5} T_{\mathrm{THz}}$), with integer m. Generally, $p_{\mathbf{k}}(f_n)$ exhibits $(n+1)$ lobes separated by n nodes. We call the resulting $\mathbf{k}$-dependent interference patters crystal-momentum combs, or $\mathbf{k}$-combs for short, in analogy to frequency combs created by multiple time-domain pulses [107, 108].

At the K point, the symmetry center of the lightwave trajectories, even order $\mathbf{k}$ combs exhibit a peak while the odd ordered ones feature a node. This implies a dominantly odd (even) symmetry for odd (even) ordered $\mathbf{k}$ combs, which is supported by the reduced model. In WSe_2, this symmetry is broken when $P_{\mathbf{k}}(t)$ is driven to regions of the band structure where the inversion symmetry does not apply and $E^{\mathrm{eh}}_{\mathbf{k}} \neq E^{\mathrm{eh}}_{-\mathbf{k}}$.

The symmetry of the $\mathbf{k}$ combs greatly affects the HSB intensity defined by Eq. (4.1). For inversion symmetric systems where $E^{\mathrm{eh}}_{\mathbf{k}} = E^{\mathrm{eh}}_{-\mathbf{k}}$ and $d_{\mathbf{k}} = d_{-\mathbf{k}}$, odd-order sidebands do not exist [62] because antisymmetric $\mathbf{k}$ combs make the total sum of $I(f_n)$ in Eq. (4.1) vanish. Only the even part of the $\mathbf{k}$ combs, $p^{\mathrm{even}}_{\mathbf{k}}(f_n) \equiv \frac{1}{2}[p_{\mathbf{k}}(f_n) + p_{-\mathbf{k}}(f_n)]$, contributes to the emission, allowing only even ordered sidebands. In monolayer WSe_2, the inversion symmetry

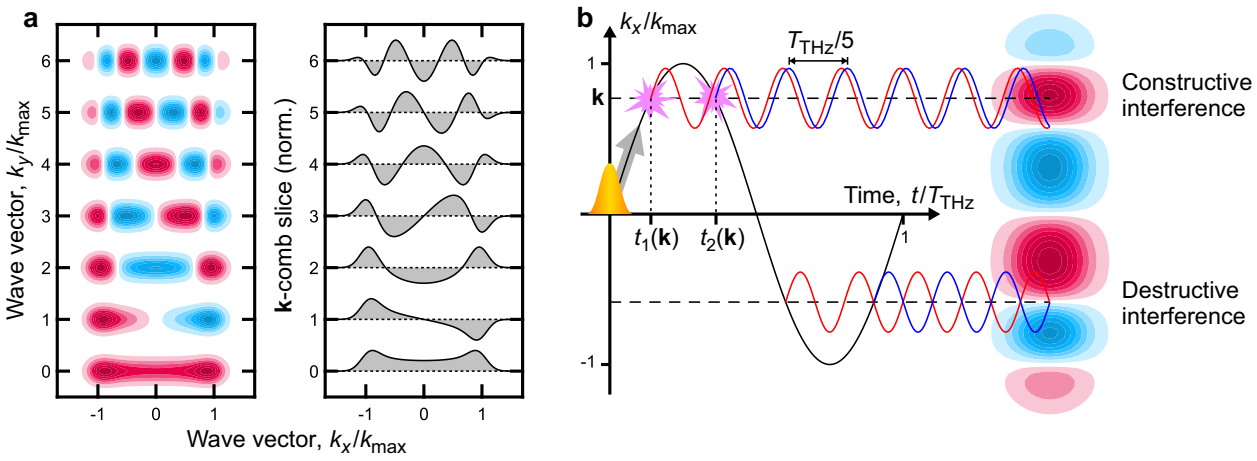

Figure 4.3: Crystal-momentum combs. **a**, Analytically computed crystal-momentum combs (**k** combs) of order $n = 0$ to 6 for a Gaussian $P^{\text{rot}}_{\mathbf{k}}$ translated along a sinusoidal path in momentum space with maximum displacement k_{max}. Left, two-dimensional $p_{\mathbf{k}}(f_n)$, **k** combs are shifted in k_y for better visibility. Red indicates positive, blue negative values. Right, slices of $p_{\mathbf{k}}(f_n)$ through $k_y = 0$. **b**, Schematic illustrating the origin of **k** combs on the example of the 5th order. A wave packet of microscopic polarization (orange wave packet) is translated along a sinusoidal path in momentum space (black line) via lightwave driving. The wave packet crosses a given wave vector **k** twice per translation cycle at times $t_1(\mathbf{k})$ and $t_2(\mathbf{k})$, each time (pink sparks) creating a burst of emission. Depending on the relative timing of the burst, they can either interfere constructively (top dashed line) or destructively (bottom dashed line), creating an interference pattern in momentum space (red–blue contours on the right), the **k** comb.

is broken [109]. Comparing QDCE computed even-ordered **k** combs $p_{\mathbf{k}}(f_n)$ (Fig. 4.2, blue color map) with their even contributions $p^{\text{even}}_{\mathbf{k}}(f_n)$(Fig. 4.2, red color map), verifies their dominantly even symmetry. On the other hand, the even contributions of odd orders $n = 1, 3, 5$ in Fig. 4.2 vanishes within the K valley but peaks sharply beyond a certain point. Near the K point, all matrix elements are symmetric and asymmetric features (such as $E^{\text{eh}}_{\mathbf{k}} \neq E^{\text{eh}}_{-\mathbf{k}}$) only become relevant near the M point where the even parts of the odd-order **k** combs are located. For odd orders to appear, $P_{\mathbf{k}}(t)$ needs to be translated to such regions. In other words, the odd order **k** combs need to extend into the asymmetric regions for odd order HSBs to appear. For this reason, the emission of odd HSBs strictly originates from the outermost comb line. Even though the $p^{\text{even}}_{\mathbf{k}}(f_n)$ of even HSBs are not localized in the same way, the outermost **k**-comb line still defines a sharp leading edge which determines the HSB emission

strength. It is important to note that the $\mathbf{k}$ combs are projections of $P_{\mathbf{k}}(t)$ (which oscillate with energy $E^{\mathrm{eh}}_{\mathbf{k}}/h$) onto the HSB energy hf_n. Their amplitudes decrease quickly if $P_{\mathbf{k}}(t)$ does not support energies that equal the HSB energy.

For both even and odd orders, the outermost comb line is a good guiding point to locate HSB emission in momentum space. Classically, this line is expected to be located at the point of maximum excursion $\frac{|e|E_{\mathrm{THz}}}{hf_{\mathrm{THz}}}$ as described by Eq. (3.27). To take into account changes due to many-body effects and dephasing, we quantify the outermost comb line for order n by

$$k(n) = \frac{|e|E_{\mathrm{THz}}}{hf_{\mathrm{THz}}} C_n(E_{\mathrm{THz}}, f_{\mathrm{THz}}) \ , \tag{4.5}$$

where the direction is dictated by the lightwave with peak field strength E_{THz} and central frequency f_{THz}, and C_n captures the deviations from the classically expected wave vector. Typical values of C_n for $n = 4$ and 5 are between 0.5 and 1.5 as shown in Fig. 4.4. The correction factor is almost constant as function of the THz field strength (Panels a and c), while it is strongly dependent on the THz frequency (Panels b and d). At low frequencies where the THz period T_{THz} is long, scattering and dephasing can prevent $P_{\mathbf{k}}(t)$ from reaching the classically expected maximum excursion. In contrast, the correction factor increases at higher frequencies and is expected to eventually saturate in the limit where T_{THz} becomes large compared to the lifetime of $P_{\mathbf{k}}(t)$.

To quantify the resolution of our approach, we follow the width of the outermost comb line and compare it to the width of the entire $\mathbf{k}$ comb. If the n-th order $\mathbf{k}$ comb were evenly split into $(n + 1)$ lines, the resolution would increase by a factor of $(n + 1)$. Figure 4.5 compares this simple estimate (blue line) to the actual resolution of combs generated by a lightwave with peak field strength $E_{\mathrm{THz}} = 11.4$ MV/cm and central frequency $f_{\mathrm{THz}} = 42$ THz based on a QDCE computation (black dots), corroborating the super-resolution properties of the $\mathbf{k}$ combs. The resolution improvements grow approximately linear with the sideband

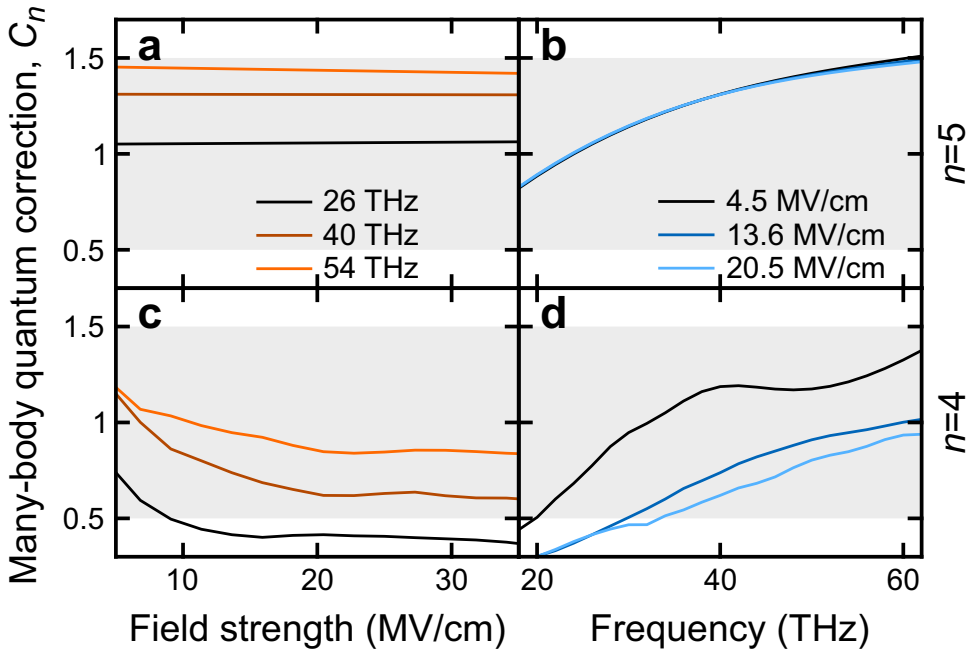

Figure 4.4: Many-body corrections for tomographic mapping. **a** and **b**, Many-body corrections C_n for the 5th order HSB based on the position of the outermost line of the **k** comb as function of the THz peak field strength (a) and the THz center frequency (b) for three selected cases. **c** and **d**, Many-body corrections C_n for the 4th order HSB based on the **k**-comb width as function of the THz peak field strength (c) and the THz center frequency (d) for three selected cases.

order n.

4.4 Tomography of electronic bands

4.4.1 Field-strength scan

To demonstrate the band-structure tomography in practice, we use experimental HSB spectra recorded in Rupert Huber's group (University of Regensburg). They optically excited the $1s$–A exciton resonance in a monolayer sample of WSe_2 with a 100 fs long pulse and a photon energy centered at $hf_{\mathrm{opt}} = 1.665$ eV. A co-propagating linearly polarized and 100 fs long multi-terahertz transient with central frequency of $f_{\mathrm{THz}} = 42$ THz was used to accelerate the excited $P_{\mathbf{k}}(t)$ along the Γ–K direction. The momentum of the outermost comb line $k(n)$ was controlled by scanning the (vacuum) peak field strength $E_{\mathrm{THz}}^{\mathrm{peak}}$ between 7 and 19 MV/cm.

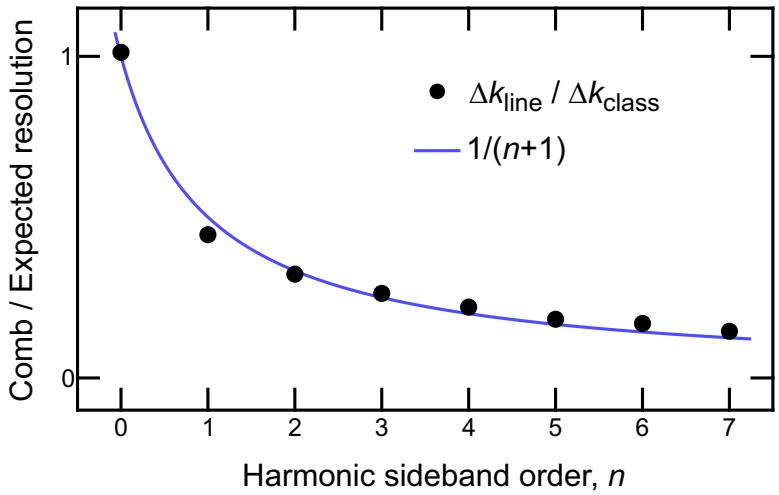

Figure 4.5: Resolution of crystal-momentum comb tomography. The ratio $\Delta k_{\text{line}}/\Delta k_{\text{class}}$ (black points) between the width of the outermost $\mathbf{k}$-comb line Δk_{line} and the expected resolution based on the classical wave-packet excursion range Δk_{class} is shown for a peak THz field strength of $E_{\text{THz}} = 11.4$ MV/cm and center frequency $f_{\text{THz}} = 42$ THz as function of the sideband order n. The improvement in resolution with the sideband order n is compared to the function $1/(n+1)$ (blue line).

For more details about the experiment, we refer the reader to the Supplementary Material of Ref. [110] as well as Ref. [111]. A subset of the recorded HSB spectra are shown in Fig. 4.6a. The spectra cover the entire visible range and show strong changes as a function of $E_{\text{THz}}^{\text{peak}}$. While the 3rd HSB only emerges for the highest fields, the 5th order intensity (Fig. 4.6c) increases sharply at $E_{\text{THz}}^{\text{peak}} = 7$ MV/cm, peaks at 13 MV/cm, and decreases for the highest fields, clearly exhibiting non-perturbative behavior.

To connect this particular $E_{\text{THz}}^{\text{peak}}$ dependence with the $\mathbf{k}$ combs, we compare the experiment to QDCE computations. The computed spectra (Fig. 4.6b) are compared quantitatively and agree well with the experiment (Fig. 4.6a). The computed intensity dependence of the 5th HSB (Fig. 4.6c, shaded area) perfectly reproduces the onset, peak, and drop of the experimental data (red dots). The QDCE computations provide access to the $p_{\mathbf{k}}^{\text{even}}(f_5)$ (Fig. 4.6d, red color map) which assign a crystal momentum $k(5)$ (Fig. 4.6d, blue lines) as function of $E_{\text{THz}}^{\text{peak}}$. Figure 4.6e shows the electron–hole energy $E_{\mathbf{k}}^{\text{eh}}$ (shaded area) together with the inverted $E_{-\mathbf{k}}^{\text{eh}}$ (dotted line) to make the band asymmetries ($E_{\mathbf{k}}^{\text{eh}} \neq E_{-\mathbf{k}}^{\text{eh}}$) easier to

recognize. Comparing the sideband intensity (Fig. 4.6c) with $E^{\mathrm{eh}}_{\mathbf{k}}$, it is evident that the 5th HSB precisely sets on when the 5th order **k** comb, $k(5)$, reaches the band asymmetry (blue arrow), corroborating the super-resolution connection between the position of the outermost comb line and odd-ordered HSB intensities.

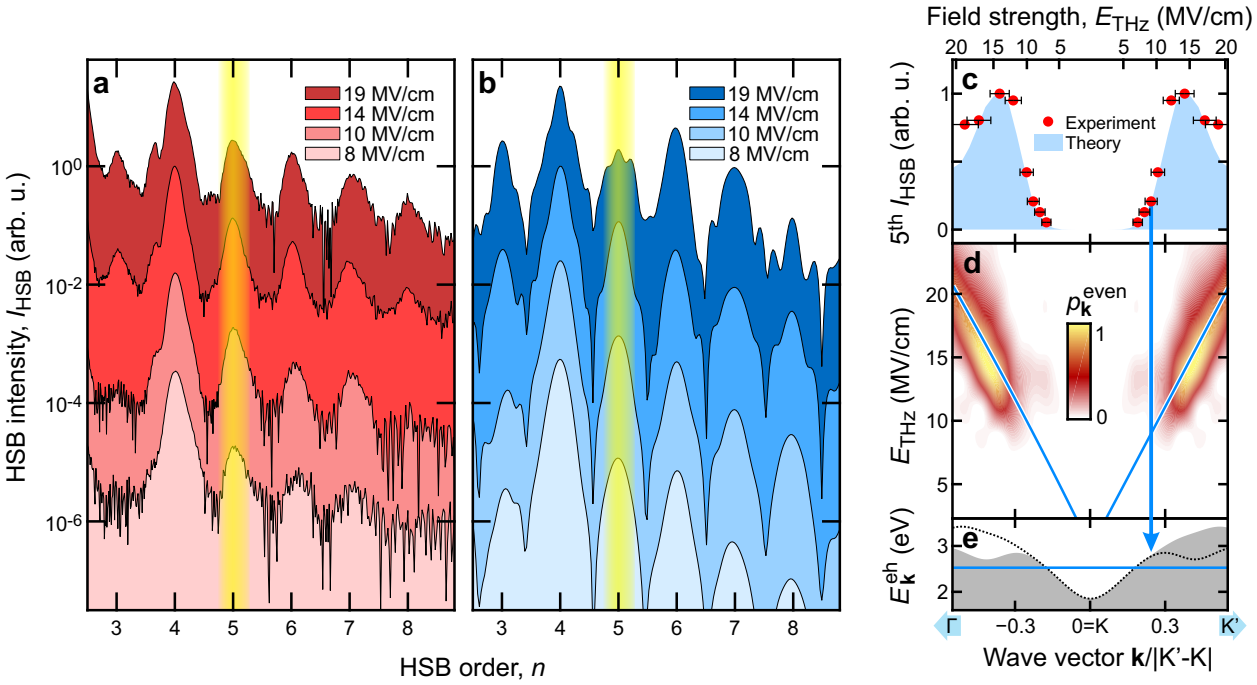

Figure 4.6: Crystal-momentum comb tomography with a field-strength scan of the 5th HSB. **a** and **b**, Measured (a) and computed (b) HSB intensity spectra I_{HSB} at different peak field strengths E_{THz} (shifted for visibility) and fixed center frequency $f_{\mathrm{THz}} = 42$ THz. The 5th order HSB is highlighted by the yellow transparent bar. **c**, Field-strength dependent (top axis) 5th-order HSB intensity is shown for the measured (red dots with error bars) and computed (shaded area) results. The respective $k(5)$ assignment is shown on the bottom axis. **d**, The $k_y = 0$ slice of the symmetric part of the 5th order **k** comb, $|p^{\mathrm{even}}_{\mathbf{k}}(f_5)|$, as function of E_{THz}. The blue line marks the position of the outermost line, $k(5)$. **e**, Electron–hole energy $E^{\mathrm{eh}}_{\mathbf{k}}$ (gray area) along the K–K' direction and $E^{\mathrm{eh}}_{-\mathbf{k}}$ (dotted line) are connected (blue arrow) to the HSB intensity via the **k** combs.

When increasing $E^{\mathrm{peak}}_{\mathrm{THz}}$ further, the **k** comb is shifted clearly into the asymmetric region, leading to an increase in intensity. However, at the highest $E^{\mathrm{peak}}_{\mathrm{THz}}$, the central energy of the polarization is far offset from the energy of the 5th HSB which eventually reduces the HSB intensity again. The sharply peaked $E^{\mathrm{peak}}_{\mathrm{THz}}$ dependence of the 5th HSB intensity is a signature of the super-resolution aspects introduced by the odd-ordered **k** combs.

The even orders show a similar behavior. Figure 4.7 provides the **k** comb analysis for the 4th order HSB which exhibits a sharp increase in intensity when $E^{\mathrm{eh}}_{\mathbf{k}}$ at $k(4)$ is resonant with the energy of the 4th HSB (Fig. 4.7b, blue horizontal line). Due to the symmetry of the even **k** combs, the 4th order can also detect the band within the symmetric region of $E^{\mathrm{eh}}_{\mathbf{k}}$ and does not require asymmetries.

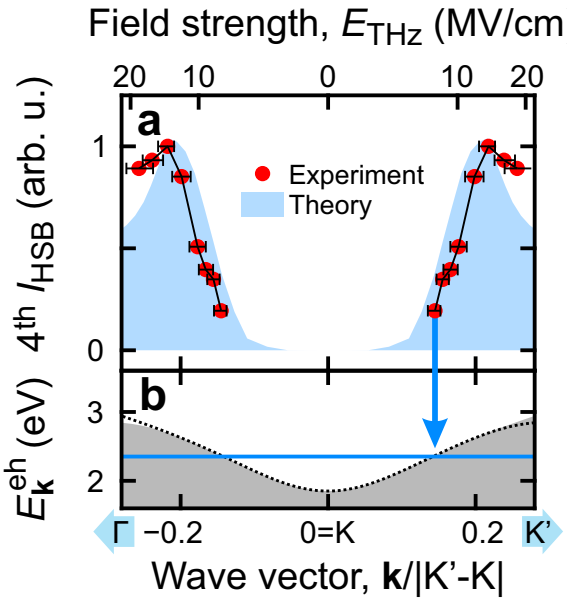

Figure 4.7: Crystal-momentum comb tomography with a field-strength scan of the 4th HSB. **a**, Field-strength dependent (top axis) 4th-order HSB intensity is shown for the measured (red dots with error bars) and computed (shaded area) results. The respective $k(4)$ assignment is shown on the bottom axis. **b**, Electron–hole energy $E^{\mathrm{eh}}_{\mathbf{k}}$ (gray area) along the K–K' direction and $E^{\mathrm{eh}}_{-\mathbf{k}}$ (dotted line) are connected (blue arrow) to the HSB intensity via **k**-comb tomography.

To summarize, by varying the field strength and scanning $k(n)$ along a fixed sideband energy, the onset of sideband intensity identifies the band itself for even orders, and the onset of asymmetries for odd orders. Repeating this process for different THz frequencies f_{THz} scans the sideband energy which yields access to the full band structure.

4.4.2 Frequency scan

Experimentally, our collaborators have measured HSB spectra at a fixed field strength of $E^{\mathrm{peak}}_{\mathrm{THz}} = 14$ MV/cm while varying the central frequency f_{THz} over one full octave, from 27 to

54 THz. The field strength was chosen to provide efficient HSB generation while still being below the threshold where interband excitation of the lightwaves becomes relevant and high harmonic generation sets on. A subset of the experimental spectra are shown in Fig. 4.8a and are compared to QDCE results in Fig. 4.8b. Figure 4.8c shows the measured (red dots) and computed (shaded area) intensity of the 5th order HSB as function of f_{THz}. Similar to the field-strength scan in Fig. 4.6c, the f_{THz} dependence of the HSB intensity displays a clear onset, peak, and drop. By scanning f_{THz}, both $k(n)$ and the sideband energy change. Figure 4.8d shows the f_{THz}-dependent $p_{\mathbf{k}}^{\mathrm{even}}(f_5)$ (red color map) and $k(5)$ (blue line) relative to the band gap $E_{\mathbf{k}}^{\mathrm{eh}}$ (black line). The sideband intensity peaks for $f_{\mathrm{THz}} = 42$ THz where the sideband energy is close to the energy of the polarization ($E_{\mathbf{k}}^{\mathrm{eh}}$ at $k(5)$) and also overlaps with the asymmetric region, fulfilling the two necessary conditions for odd-order HSB emission. The HSB intensity quickly drops both at lower f_{THz} because the polarization energy becomes too far offset from the sideband energy, and at higher f_{THz} because the $\mathbf{k}$ comb does not reach the asymmetric region. Overall, this results in a narrow f_{THz}-dependent peak of the 5th order HSB.

4.4.3 Full reconstruction

The combination of experimental measurement and theoretical guiding enables super-resolution lightwave tomography. The $\mathbf{k}$ combs localize HSB emission from a set of experimental parameters (E_{THz}, f_{THz}) to a narrow region in ($\mathbf{k}$, energy) space. By scanning both E_{THz} and f_{THz}, the entire band energy $E_{\mathbf{k}}^{\mathrm{eh}}$ can be mapped tomographically.

We computed HSB intensities $I(f_n)$ for a comprehensive scan of (E_{THz}, f_{THz}) to demonstrate what our tomographic approach can achieve. The emission of each sideband order generated from (E_{THz}, f_{THz}) is mapped to ($\mathbf{k}$, energy)-space by assigning the coordinate $[k(n), E_n^{\mathrm{HSB}}]$. The mapped intensities for orders $n = 3, 4, 5, 6$ are shown in Figs. 4.9a–d together with the band gap $E_{\mathbf{k}}^{\mathrm{eh}}$ (sold lines) and $E_{-\mathbf{k}}^{\mathrm{eh}}$ (dotted lines). The band structure clearly follows the edge of the intensity, corroborating that the onset of HSB emission is defined by

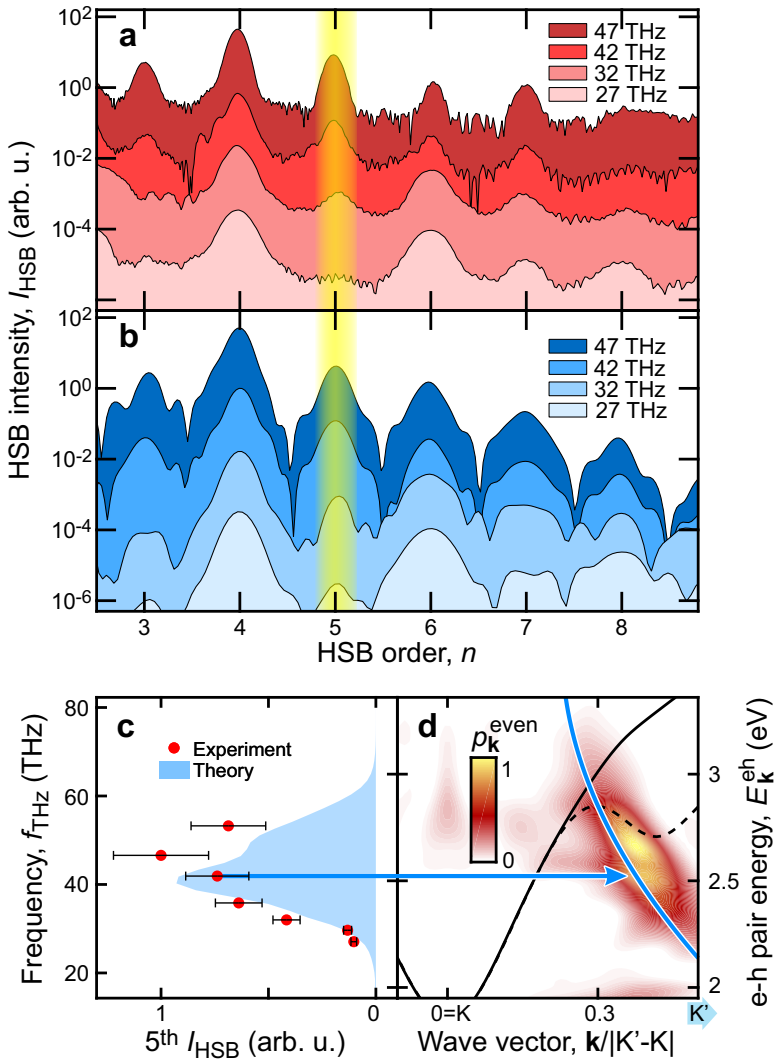

Figure 4.8: Crystal-momentum comb tomography with a frequency scan of the 5th HSB. **a** and **b**, Measured (a) and computed (b) HSB intensity spectra I_{HSB} at different center frequencies f_{THz} (shifted for visibility) and fixed peak field strength $E_{\mathrm{THz}} = 14$ MV/cm. The 5th order HSB is highlighted by the yellow transparent bar. **c**, Field-strength dependent (left axis) 5th-order HSB intensity is shown for the measured (red dots with error bars) and computed (shaded area) results. The respective $k(5)$ assignment is shown on the right axis. **d**, The $k_y = 0$ slice of the symmetric part of the 5th order **k** comb, $|p_{\mathbf{k}}^{\mathrm{even}}(f_5)|$, as function of the sideband energy $h(f_{\mathrm{opt}} + 5 * f_{\mathrm{THz}})$. The blue line marks the position of the outermost line, $k(5)$, and is compared to the electron–hole energy $E_{\mathbf{k}}^{\mathrm{eh}}$ (black solid line) along the K–K' direction and $E_{-\mathbf{k}}^{\mathrm{eh}}$ (black dashed line). The blue arrow points to the conditions that create peak HSB emission.

the crossing of $k(n)$ with $E_{\mathbf{k}}^{\mathrm{eh}}$. While the even orders $n = 4$ and 6 capture the band structure near the K point, the odd orders $n = 3$ and 5 provide additional sensitivity to the band symmetry and reveal $E_{\mathbf{k}}^{\mathrm{eh}} \neq E_{-\mathbf{k}}^{\mathrm{eh}}$ conditions away from the K point.

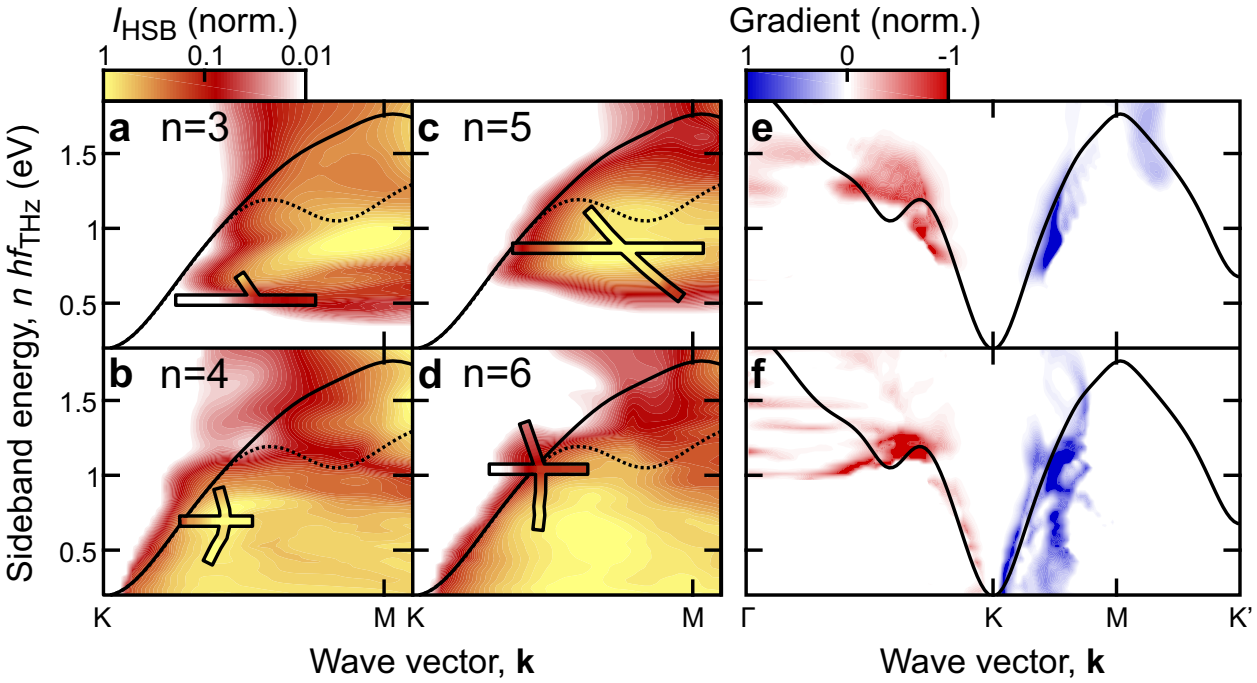

Figure 4.9: Super-resolution lightwave tomography. **a** to **d**, Contours show computed HSB intensities of the 3rd (a), 4th (b), 5th (c), and 6th (d) order based on a two-dimensional (E_{THz}, f_{THz}) scan and mapped into energy–momentum space via crystal-momentum comb tomography. The intensities are compared the electron–hole energies $E^{\mathrm{eh}}_{\mathbf{k}}$ (solid line) and $E^{\mathrm{eh}}_{-\mathbf{k}}$ (dotted line) as well as experimentally measured one-dimensional scans of E_{THz} and f_{THz} (colored lines in black boxes). **e** and **f**, The electron–hole energy $E^{\mathrm{eh}}_{\mathbf{k}}$ (solid line) is compared to the computed gradients of the $R_{5\mathrm{th}/3\mathrm{rd}}$ (e) and $R_{6\mathrm{th}/4\mathrm{th}}$ (f) ratios along the wave vector (blue color map) and energy (red color map) directions; only the first gradient peaks are shown.

The one-dimensional experimental E_{THz} and f_{THz} scans discussed in Figs. 4.6 and 4.8, respectively, are shown in Figs. 4.9a–d as colored traces surrounded by black lines (cross shaped). A single factor has been multiplied to the experimental intensities in order to align the units between experiment and theory. Consistent with the earlier discussion, the experimental intensities almost perfectly fit into the computed intensity landscapes.

According to Eq. (4.1), also the dipole $d_{\mathbf{k}}$ affects the HSB intensity. In order to avoid distortions in the mapped intensities due to the $\mathbf{k}$ dependence of $d_{\mathbf{k}}$, we construct the ratio $R_{5\mathrm{th}/3\mathrm{rd}} \equiv I(f_5)/I(f_3)$ between the two analyzed odd sideband orders. The edges of the intensity map are quantified in a gradient analysis. Fig. 4.9e shows the first positive peak of $\frac{\partial}{\partial k} R_{5\mathrm{th}/3\mathrm{rd}}$ in the blue color map and the first negative peak of $\frac{\partial}{\partial \mathrm{energy}} R_{5\mathrm{th}/3\mathrm{rd}}$ in the red color

map. The revealed features closely track the band gap $E_{\mathbf{k}}^{\mathrm{eh}}$ (black line) in the asymmetric region. While the $\mathbf{k}$ gradient is more sensitive to vertical features of $E_{\mathbf{k}}^{\mathrm{eh}}$ to the right of the K point, the energy gradient captures the more flat dispersion to the left of K. The same analysis is performed for the ratio of the even orders, $R_{\mathrm{6th/4rd}}$ (Fig. 4.9f). The even orders also track the symmetric part of $E_{\mathbf{k}}^{\mathrm{eh}}$ close to the K point.

The mapping presented in Fig. 4.9 heavily relies on a quantitative theory analysis of the experiment in order to obtain accurate many-body corrections $C_n(E_{\mathrm{THz}}, f_{\mathrm{THz}})$ for a precise mapping of the measured intensities to $(k(n), E_n^{\mathrm{HSB}})$. However, super-resolution tomography also works without extensive QDCE computations. Figure 4.10 presents the same gradient analysis of the 5th/3rd and 6th/4th intensity ratios as Fig. 4.9e and f, but assuming a constant $C_n = 1.3$. The mapping only uses the parameters E_{THz}, f_{THz}, and f_{opt} that are known from experiment and map intensities onto $[k(n), hf_{\mathrm{opt}} + nhf_{\mathrm{THz}}]$. Even without elaborate many-body inputs, the analysis locates important band structure features. Compared to the full analysis (Fig. 4.9e and f), a constant C_n introduces only minor aberrations in the gradient signal, making a purely experimental super-resolution tomography feasible.

4.5 Lightwave tomography beyond the band structure

The analysis in the previous section is mostly focused on the reconstruction of the band energy. However, we already saw that other material properties such as the microscopic dipole and many-body effects mediated by the Coulomb interaction affect the tomography and the HSBs. Conversely, this means that HSBs contain information about such material properties that can be extracted.

Figure 4.11a compares the experimentally measured (red line) and computed (black line) HSB spectrum for a THz field with a peak field strength of $E_{\mathrm{THz}} = 9.1$ MV/cm and a center frequency of $f_{\mathrm{THz}} = 42$ THz. The quantitative agreement between experiment and theory suggest that the QDCE computations accurately capture all relevant aspects of the material

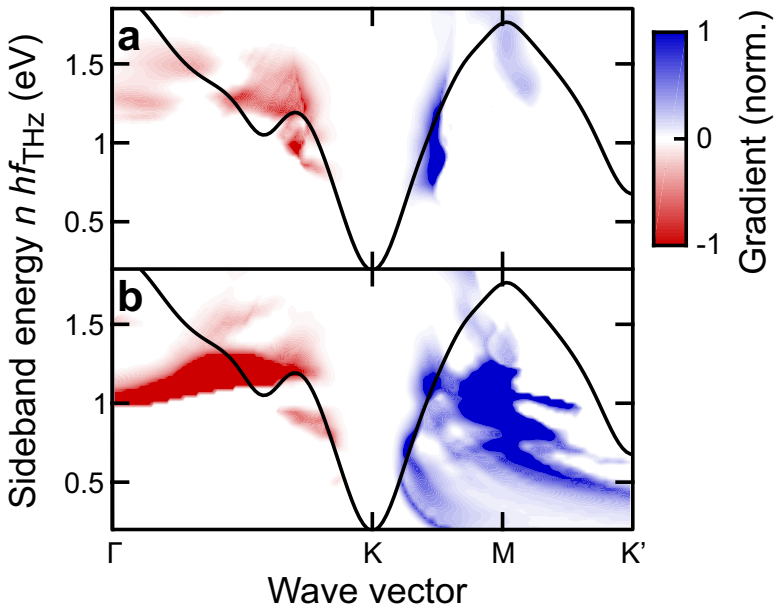

Figure 4.10: Super-resolution lightwave tomography with constant correction factor. **a** and **b**, The electron–hole energy $E^{\mathrm{eh}}_{\mathbf{k}}$ (solid line) is compared to the computed gradients of the $R_{5\mathrm{th}/3\mathrm{rd}}$ (a) and $R_{6\mathrm{th}/4\mathrm{th}}$ (b) ratios along the wave vector (blue color map) and energy (red color map) directions; only the first gradient peaks are shown. A constant $C_n = 1.3$ is assumed for the tomography.

and experiment. We artificially modify the accurate dipole matrix elements (Fig. 4.11b, black line) by adding (dashed line) or removing (dotted line) dipole contributions between the K and M point. The computed spectra for the modified dipoles (Fig. 4.11a dashed and dotted lines) mostly affect the intensity of the 6th order HSB and lead to deviations from experiment.

A similar approach can be used to demonstrate the sensitivity of the HSB spectra to Coulomb effects (quantified by the excitonic binding energy). Figure 4.12 compares the same measured (red line) and computed (black line) HSB spectrum as for the dipole discussion. By changing the Coulomb interaction, the binding energy is tuned from its nominal value of 200 meV (black line) to 0 meV (shaded area), 50 meV (dotted line), and 325 meV (dashed line). For lower binding energy, the 3rd, 4th, and 5th HSB decrease in intensity by up to one order of magnitude while the 6th order remains almost unchanged. For a stronger binding energy of 325 meV, the changes are opposite and intensities increase.

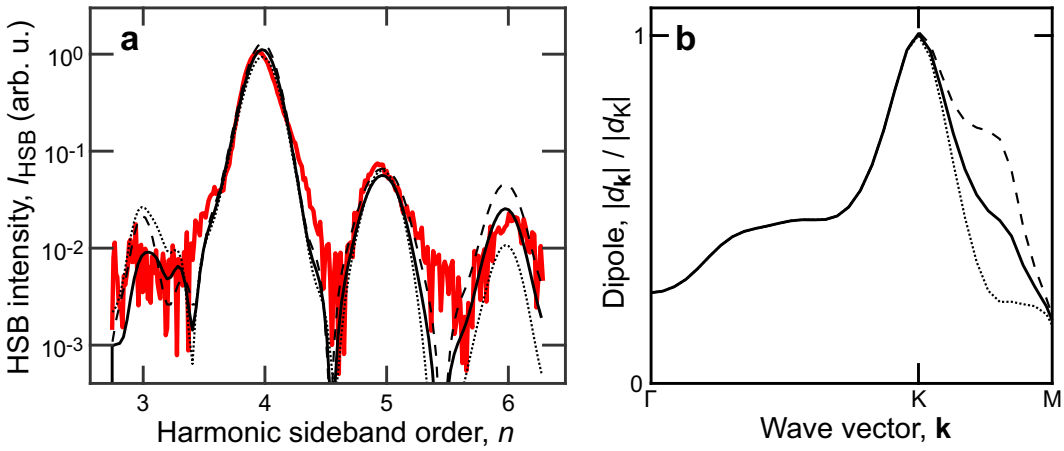

Figure 4.11: Effect of the dipole matrix elements on HSB spectra. **a**, Measured (red line) versus computed HSB spectra using the actual dipole matrix elements (solid line) compared to dipole matrix elements that were locally increased (dashed line) or decreased (dotted line). The measured and computed HSB spectra are generated from a THz pulse with peak field strength $E_{\mathrm{THz}} = 9.1$ MV/cm and center frequency $f_{\mathrm{THz}} = 42$ THz. **b**, Slice along the Γ–K direction of the absolute value of the dipole matrix elements used for the computations in (a).

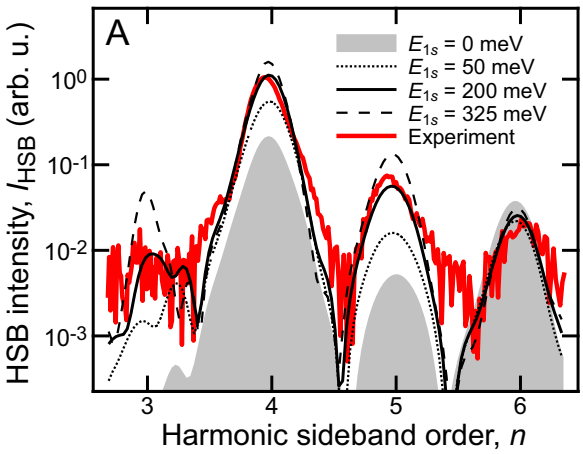

Figure 4.12: Effect of Coulomb interaction strength on HSB spectra. Measured (red line) versus computed HSB spectra with varying Coulomb-interaction strengths quantified via the exciton binding energy. Black line shows computed results using the actual interaction strength leading with an exciton binding energy of $E_{1s} = 200$ meV. The results are compared to cases with no excitons (shaded area) and excitons with a binding energy of 50 meV (dotted line) and 325 meV (dashed line). The measured and computed HSB spectra are generated from a THz pulse with peak field strength $E_{\mathrm{THz}} = 9.1$ MV/cm and center frequency $f_{\mathrm{THz}} = 42$ THz.

The two examples of Figs. 4.11 and 4.12 clearly show that HSB spectra are sensitive to both details of the microscopic dipole and the magnitude of the Coulomb interaction.

While we were not able to directly map those quantities in a similar tomographic approach as for the band structure so far, insights can be gained from quantitative theory–experiment comparisons of the spectra.

4.6 Conclusion and outlook

In this Chapter, we demonstrated super-resolution lightwave tomography by reconstructing the electronic band structure of WSe_2 from a set of HSB measurements. The tomographic approach is based on crystal-momentum combs which emerge from the near-harmonic driving of coherent excitons and precisely map the emission of sidebands to narrow regions in momentum space. The trajectory of the lightwave driven excitons in solids is strongly affected by many-body effects and consequently impacts the crystal-momentum comb mapping. We solved the lightwave SBEs introduced in Chapter 3 to quantify the effect of interactions on the lightwave driving to improve the quality of the mapping and the resulting tomography.

Super-resolution lightwave tomography allows for an all-optical reconstruction of the electronic band structure and provides experimental access to materials and structures where ARPES fails due to its requirement to collect photoelectrons. Lightwave tomography only requires light to get to and out of the sample which enables characterization in situ and under operational conditions. Furthermore, the tomography can be performed on microscopically small samples or regions by focusing the HSB-generating lightwaves to a narrow spot. In the future, this could allow lightwave tomography to track changes of the electronic structure in devices or nanostructures in real time during their operation. Because of this, lightwave tomography has the potential to become an important tool in the discovery, development, and characterization of novel quantum materials, functionalities, and devices.

We expect that lightwave tomography can be further improved in the future. A next logical step is to correlate the tomography of more than two HSB orders and performing tomography for different band combinations. By asymmetrically driving the system, for

example with unipolar pulses [112], directional information can be gained to feed into the tomography. As a long-term goal, we also hope to directly access dipole and Coulomb matrix elements which we already demonstrated the HSB are sensitive to (Section 4.5).

Chapter 5

Lightwave Attoclocking of Quantum Correlations

This Chapter is in parts adapted from J. Freudenstein, M. Borsch, M. Meierhofer, D. Afanasiev, C. P. Schmid, F. Sandner, M. Liebich, A. Girnghuber, M. Knorr, M. Kira, and R. Huber, "Attosecond clocking of correlations between Bloch electrons", Nature **610**, 7931 (2022).

5.1 Introduction

Correlations between delocalized Bloch electrons in solids determine the optical [113] and electronic [114] properties of materials and lead to the emergence of intriguing effects such as topological phase transitions [45, 115], and room-temperature stable quantum states [116–118]. To leverage such effects, for example in quantum-information applications [119, 120], they need to be switched or otherwise manipulated as a function of time. This requires a detailed understanding of the dynamics of correlations. Transitions among electronic correlations occur on the order of millielectronvolts [45, 113–115, 121, 122] (meV) and take place at attosecond time scales [123–132]. While attosecond pulses that provide the desired temporal resolution Δt in pump–probe-type experiments exist, they exhibit energy uncertainties ΔE of tens of electron volts (eV) due to the time–energy uncertainty relation $\Delta t \cdot \Delta E > h$ with

the Planck constant h. This makes attosecond pulses virtually blind to the relevant meV transitions of correlations and prevents a direct detection of the correlation dynamics with attosecond precision.

In this Chapter, a detailed theory–experiment investigation is presented that demonstrates how low-frequency lightwaves are utilized to clock the electron–hole pair dynamics with attosecond precision to detect correlations. The lightwave SBEs developed in Chapter 3 provide insights into the microscopic dynamics which is intuitively visualized and analyzed using Wigner functions to display coherent excitons in phase space. The Wigner functions directly show the effect of correlations on the electron–hole dynamics and its connection to the attoclocking approach. We demonstrate the detection of tunable correlations and microscopic scattering via the attoclocking approach and predict that attoclocking can detect phase transitions such as the excitonic Mott transition [41, 133, 134].

5.2 Idea of lightwave chronoscopy

The attoclocking approach (illustrated in Fig. 5.1) is based on the idea of the quasiparticle collider [59] that uses the oscillations of an intense few-cycle lightwave as a temporal measuring stick. A resonant interband excitation creates coherent electron–hole (e–h) pairs at a tunable excitation time t_{ex} relative to the lightwave. The e–h pairs are initially created with zero relative momentum $\hbar k$ and displacement x. The strong lightwave exerts a force (Fig. 5.1, shaded area) that acts on the oppositely charged electrons and holes and separates them by increasing their relative displacement and momentum. When the lightwave changes polarity, electrons and holes are accelerated back towards each other. If the timing of the excitation t_{ex} is right, the electron and hole trajectories recollide (zero displacement) at which point they recombine and emit their excess kinetic energy as broadband HSB radiation. At less optimal t_{ex}, recollisions are not efficient or do not take place within the lifetime of the coherent excitons, resulting in lower or no HSB emission. The optimum recollision conditions

are experimentally determined by recording the HSB emission as function of t_{ex}.

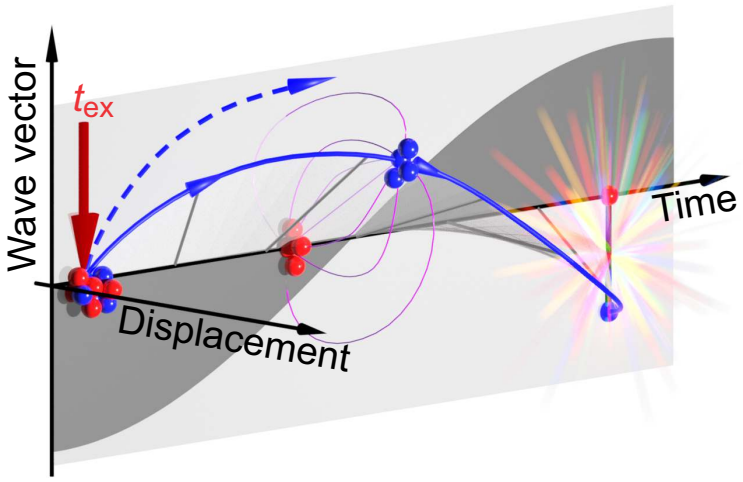

Figure 5.1: Schematic of phase-space trajectories during attoclocking of quasiparticle collisions. Electron–hole pairs (blue and red spheres) are generated by a resonant pulse at time t_{ex} (red arrow) and accelerated by a force that is exerted by an intense THz waveform (shaded area). The field first separates the electron and hole by changing their crystal momentum $\hbar k$ and relative displacement x in real space. After the field switches sign, electron and hole are accelerated towards each other where, for ideal conditions and upon recollision ($x = 0$), they emit light in the form of harmonic sidebands (sparks). The trajectory that electron and hole take in phase space (solid blue line) is influenced by the Coulomb interaction (purple field lines). Without interactions, electron and hole would follow a different trajectory (blue dashed line) with different recollision and HSB characteristics.

The motion of the e–h pairs is first and foremost determined by the single-particle dispersion $E^{\mathrm{eh}}_{\mathbf{k}}$. In a single-particle picture, the lightwave drives the momentum of e–h pairs, the velocity with which their relative displacement changes is given by $\mathbf{v}_{\mathbf{k}} = \frac{1}{\hbar}\nabla_{\mathbf{k}} E^{\mathrm{eh}}_{\mathbf{k}}$. Many-body correlations modify the trajectories and recollision times. The Coulomb interaction between electrons and holes (purple lines) acts as a restoring force. In order to reach large momenta for optimum recollision and HSB emission, an earlier t_{ex} is required to allow for enhanced action of the lightwave during the separation to compensate for the Coulomb interaction. At the same time, many-body effects also lead to scattering among electrons and holes which limits their lifetime. If excitonic coherence decays before electron and hole recollide, HSB emission does not occur.

Differences in the dynamics of free versus correlated electrons manifest themselves as

shifts Δt of the optimum excitation time t_{ex} which can be accessed experimentally. Importantly, measuring the timing of peak HSB emission to determine the optimum t_{ex} relative to the lightwave is not limited by any uncertainty relations and is the key to our attoclocking approach. Measurement of the optimum t_{ex} is only limited by the stability of the experimental setup and is demonstrated to achieve massively subcycle precision (relative to the lightwave's cycle length).

5.3 Clocking correlations in tungsten diselenide

While the effect of Coulomb correlations on the e–h dynamics can easily be studied in theory by explicitly changing the interaction strength, an experimental realization needs to find alternative ways to modify the Coulomb strength. Transition metal dichalcogenides (TMDs) offer a versatile testbed as they exhibit vastly different Coulomb interactions in their bulk vs monolayer forms. For our investigations, we chose tungsten diselenide (WSe_2) whose monolayers feature an exciton binding energy of approximately 300 meV, five times larger than the 60 meV binding energy of their bulk counterparts.

Our experimental collaborators prepared samples of both bulk and monolayer WSe_2 on a diamond substrate. They used a linearly polarized and 9 fs long near-infrared (NIR) pulse to exclusively excite the $1s$-A exciton resonance of monolayer WSe_2 (at 1.665 eV). The excited coherent excitons are then driven by a linearly polarized THz pulse (as described above) and the HSB spectra recorded as a function of t_{ex}. For more information about the experimental details and challenges, we refer the reader to Ref. [135]. To quantitatively analyze the experiment, we perform QDCE computations as outlined in Chapter 3, that use the same sample structure, pump spectrum, and lightwave transients as the experiment.

Figure 5.2a shows the computed integrated HSB intensity I_{HSB} (integrated over energy range of 2.0 to 2.64 eV which covers HSB orders 4 to 9) as function of the excitation time t_{ex} for bulk (orange line) and monolayer (blue line) WSe_2. The HSBs are generated by a

lightwave (shaded area) with peak field strength $E_{\mathrm{THz}} = 4.9$ MV/cm and center frequency $f_{\mathrm{THz}} = 25$ THz. As discussed in the previous section, the relative timing between the lightwave's cycle and the excitation time t_{ex} determines the efficiency of e–h recollisions and subsequent emission of HSBs. As a result, I_{HSB} is strongly modulated. The intensities peak shortly after the lightwave's field crests every half cycle, marking the optimum t_{ex}. Comparison of I_{HSB} for monolayer (blue) and bulk (orange) computations reveals a systematic shift between their optimum t_{ex} for all peaks. Figure 5.2b shows a zoom-in of the three largest I_{HSB} peaks (lines) and compares them to experimentally measured intensities (dots). We find a quantitative agreement in the HSB intensities and the experimental measurement confirms the predicted delay between the optimum t_{ex} of monolayer and bulk samples.

To quantify the delay changes, we define the subcycle delay δ_{sc} as the delay difference between the lightwave's field crests and the closest maximum of I_{HSB} (Fig. 5.2c). A careful analysis of the experimental measurement errors results in a timing uncertainty of approximately 300 as (error bars in Fig. 5.2c) which clocks the favourable recollision events with a precision of 7.5 millicycle (about 130 times better than the lightwave's cycle length). The experiment finds that the difference between monolayer and bulk subcycle delay $\Delta t \equiv \delta_{\mathrm{sc}}^{\mathrm{ML}} - \delta_{\mathrm{sc}}^{\mathrm{bulk}}$ for each peak is consistently negative and when averaged over all cycles results in a value of -1.2 ± 0.3 fs, in agreement with our computations.

5.4 Visualizing the electron–hole dynamics

The QDCE computations provide insights into the microscopic origins of the Δt shifts that experiments cannot access. Coherent e–h excitations, or coherent excitons, are described by the microscopic polarization $P_{\mathbf{k}}$ as introduced in Chapter 3. To understand the differences between the monolayer and bulk dynamics, we apply a band-pass filter defined in Appendix E

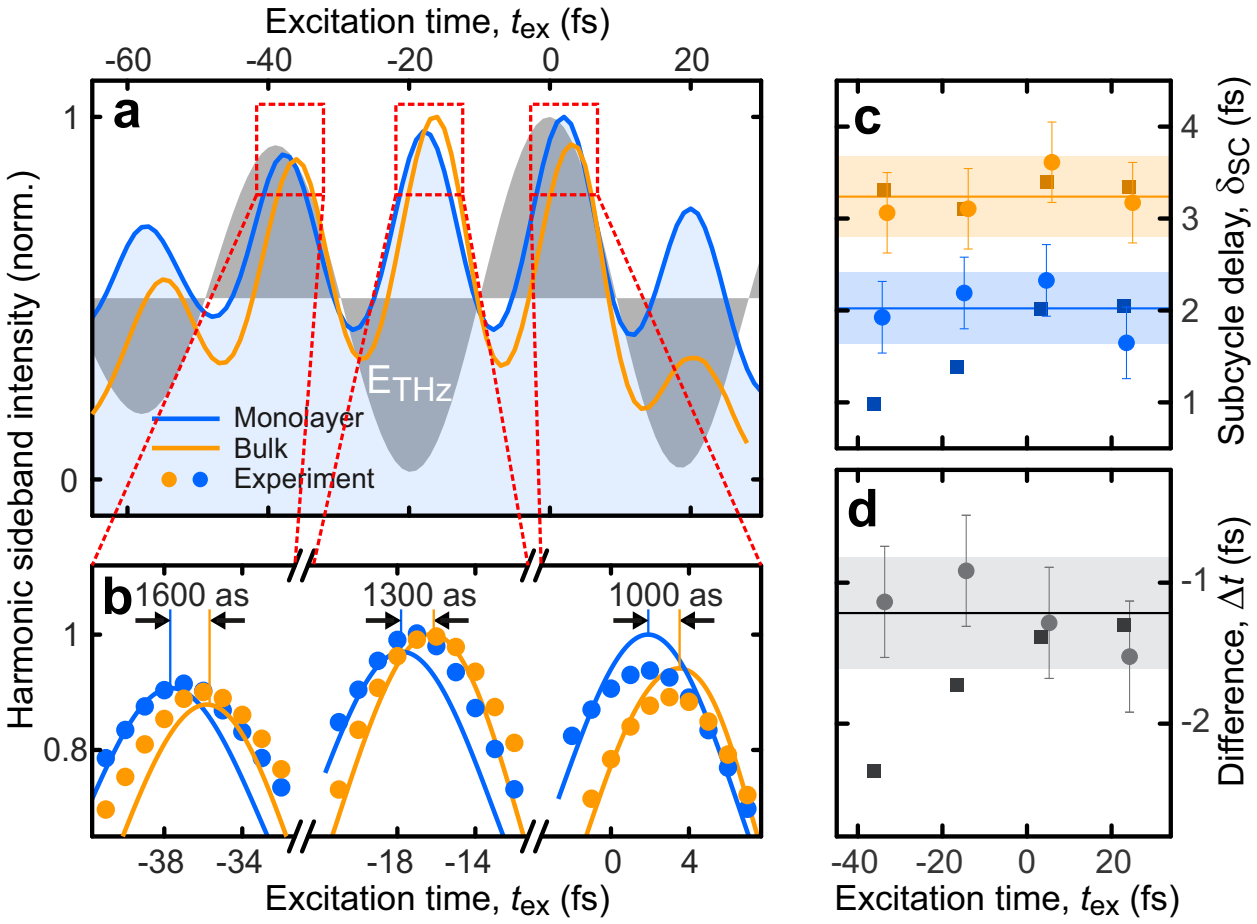

Figure 5.2: Clocking quasiparticle collisions in bulk and monolayer WSe_2. **a**, Computed HSB intensity I_{HSB} (integrated from 2.0 to 2.64 eV) from 60 nm thick bulk (orange line) and monolayer WSe_2 (blue line) as function of the excitation time t_{ex} relative to the THz driving field (shaded area) with 4.9 MV/cm peak field strength and 25 THz center frequency which is linearly polarized along the K–K' direction. **b**, Close-up of the I_{HSB} peaks near $t_{ex} = -37$ fs (left), $t_{ex} = -17$ fs (middle), and $t_{ex} = 2$ fs (right) comparing the computed results (lines) to experimentally measured I_{HSB} (circles). The difference between the excitation times at which the computed bulk and monolayer intensities peak is labelled. **c**, Computed (squares) and measured (circles with error bars) subcycle delay δ_{SC} between the optimal t_{ex} and nearest THz field maximum for bulk (blue) and monolayer (orange) WSe_2. The horizontal lines and shaded areas indicate the average values and the standard error, respectively. **d**, Computed (squares) and measured (circles with error bars) difference Δt between monolayer and bulk subcycle delays shown in **c**. The horizontal line and shaded area indicate the average value and standard error over the four measured points.

to the microscopic polarization $P_{\mathbf{k}}$

$$P_{\mathbf{k}}^{\mathrm{HSB}}(t) \equiv \int \mathrm{d}t'\, P_{\mathbf{k}}(t') G(t - t') \,, \tag{5.1}$$

to only include the parts of the coherences that contribute to HSB emission. The kernel $G(t)$ is chosen to only include frequencies that are contained in the integrated HSB intensity I_{HSB}. We then transform this frequency-filtered microscopic polarization $P_{\mathbf{k}}^{\mathrm{HSB}}$ into the quantum-equivalent of a phase-space distribution using the Wigner function transformation [136]

$$W(\mathbf{r},\mathbf{k}) \equiv \frac{1}{\mathcal{N}\pi^2}\int \mathrm{d}^2q \left[P_{\mathbf{k}+\mathbf{q}}^{\mathrm{HSB}}\right]^* P_{\mathbf{k}-\mathbf{q}}^{\mathrm{HSB}} \mathrm{e}^{-2\mathrm{i}\mathbf{q}\cdot\mathbf{r}} \,, \tag{5.2}$$

where $\hbar\mathbf{k}$ is the microscopic momentum, $\mathbf{r}$ is the relative e–h displacement of a distribution of coherent excitons, and $\mathcal{N}$ is a normalization constant. This four-dimensional function cannot be immediately plotted. However, the relevant lightwave dynamics along the direction of the driving field is extracted by projecting the distribution into 2D space

$$W(x,k) \equiv \int \mathrm{d}y\, \mathrm{d}k_y\, W(x,y,k,k_y) \,, \tag{5.3}$$

by integrating over the displacement $\mathbf{r}$ and wave vector $\mathbf{k}$ in y direction. The phase-space dynamics can be reduced to a simple (x,k) trajectory by computing centroids

$$\langle x\rangle \equiv \int \mathrm{d}x\, x\, W(x,k) \,, \text{and } \langle k\rangle \equiv \int \mathrm{d}k\, k\, W(x,k) \,. \tag{5.4}$$

In this picture, we recover the recollision interpretation of sideband emission as sidebands are being emitted when electron and hole return to zero displacement. More specifically, we find that the HSB intensity is proportional to the $x = 0$ contribution of the Wigner function. This straightforwardly connects the microscopic dynamics to the HSB emission dynamics as demonstrated in Fig. 5.3.

Figure 5.3a shows the emitted HSB intensity as function of time for monolayer (black line) and bulk (red line) WSe_2, which can be computed from $P_{\mathbf{k}}^{\mathrm{HSB}}$ and Eq. (3.20). A distribution of coherent excitons is created by a NIR pulse (orange line) at time t_{ex} after a maximum of the lightwave's transient (shaded area) corresponding to a good excitation time

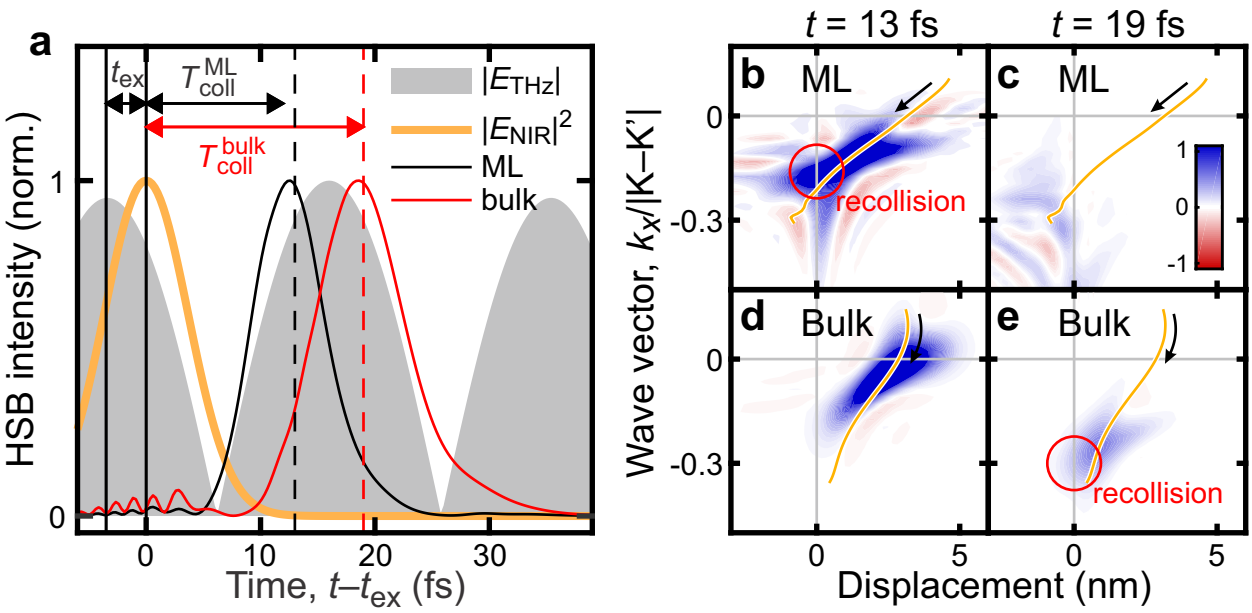

Figure 5.3: Synchronization of e–h recollisions and HSB emission. **a**, Computed time-resolved HSB emission intensity for monolayer (black line) and bulk (red line) WSe_2 from electron–hole pairs that are excited by an 8.6 fs NIR pulse (yellow line) shortly after the the maximum of a driving THz waveform (shaded area). Peak of the HSB emission (vertical dashed lines) is reached at $T_{\rm coll}^{\rm ML} = 12.6$ fs after the excitation for monolayer and at $t_{\rm coll}^{\rm bulk} = 18.6$ fs for bulk WSe_2. **b**–**e**, Snapshots of the HSB Wigner functions $W(x,k)$ at times $t = 12.6$ fs and $t = 18.6$ fs for monolayer and bulk WSe_2 are shown together with the centroid motion (orange line). Red circles mark recollision contributions ($x = 0$).

of the monolayer sample. Despite exciting both monolayer and bulk samples at the same time and driving the coherent excitons with the same lightwave, the HSB emission emerges at different time delays. For monolayer WSe_2, the HSB emission peaks at $T_{\rm coll}^{\rm ML} = 12.6$ fs after the excitation, significantly earlier than the bulk sample at time $T_{\rm coll}^{\rm bulk} = 18.6$ fs. The Wigner functions as defined in Eq. (5.3) are plotted in Fig. 5.3b–e for both monolayer and bulk computations at the respective $T_{\rm coll}$, together with their centroid motion defined by Eq. (5.4) (orange lines). At time $T_{\rm coll}^{\rm ML}$ of peak HSB emission of the monolayer sample, the monolayer $W(x,k)$ (Fig. 5.3b) exhibits a clear $x = 0$ contribution of recolliding electron–hole pairs (red circle). At a later time (Fig. 5.3c), the distribution has passed $x = 0$ and no more HSB emission occurs. On the other hand, the bulk $W(x,k)$ at time $T_{\rm coll}^{\rm ML}$ (Fig. 5.3d) has not yet reached $x = 0$. Recollision, and consequently HSB emission, are delayed until time $T_{\rm coll}^{\rm bulk}$

(Fig. 5.3e) when also the bulk $W(x,k)$ reaches $x = 0$. This demonstrates the connection of electron–hole collisions in the phase-space picture to HSB emission.

In addition to changes in the Wigner function's centroid motion, also the shape of $W(x,k)$ exhibits significant differences between bulk and monolayer WSe_2. While the bulk $W(x,k)$ is almost positive definite, the monolayer $W(x,k)$ contains significant negative contributions which are attributed to the quantumness of the respective state. Such states cannot be represented in semiclassical models and their appearance highlights the necessity of full many-body quantum theories such as the one employed in this Thesis to accurately describe lightwave-electronic processes.

5.5 Quantifying the effect of Coulomb correlations on the subcycle delay

So far, the microscopic dynamics and its connection to measurable subcycle delays was discussed and compared to experiments in monolayer vs bulk samples. In this Section, we show that the differences are dominantly attributed to the stronger Coulomb correlations in monolayer compared to bulk WSe_2. The two WSe_2 samples differ not only in the strength of correlations, but also with respect to other material properties such as small changes in the band structure which can influence the subcycle delay.

To quantify how much the subcycle delay is shifted by the Coulomb strength vs changes in the crystal structure, we vary a single parameter at a time in our QDCE computations. To tune the interaction strength, we multiply the Coulomb matrix elements $V^{\lambda,\nu}_{\mathbf{k},\mathbf{k}'}$ in Eqs. (3.14) and (3.15) by a suppression factor s_C which we track via the absolute value of the $1s$ exciton binding energy E_{1s}. The computations (Fig. 5.4) show that δ_{sc} decreases at a rate of approximately -9 as/meV with increasing E_{1s} for both the bulk (orange line) and the monolayer sample (blue line). The almost constant shift of 1.5 fs between the two curves originates from changes to the band structure between the two samples.

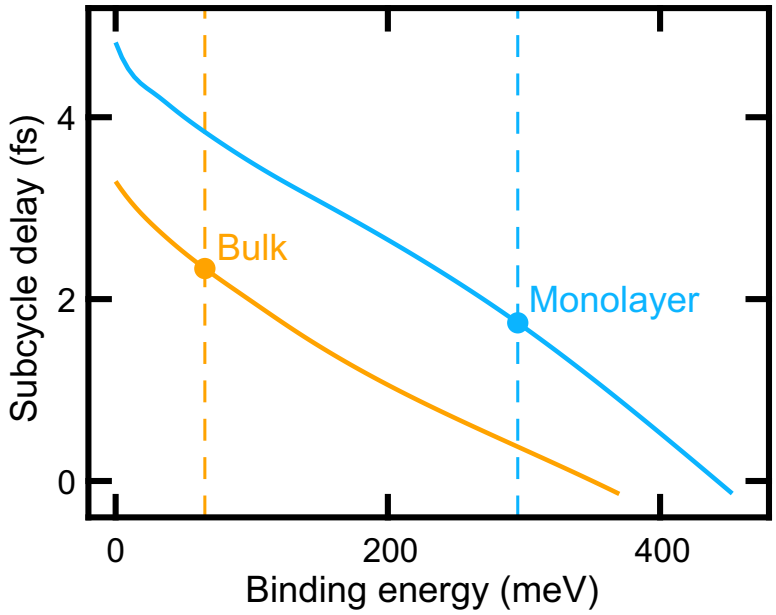

Figure 5.4: Effect of Coulomb correlations on the subcycle delay. Computed subcycle delay for bulk (orange) and monolayer (blue) WSe_2 as a function of the binding energy which is changed by artificially reducing the Coulomb interaction strength in the computations. The exciton binding energy for bulk (60 meV) and monolayer (295 meV) WSe_2 is marked by the orange and blue vertical dashed lines, respectively.

By reducing the Coulomb strength in the monolayer sample to match the bulk binding energy of $E_{1s} = 60$ meV, the subcycle delay increases from $\delta_{\mathrm{sc}}^{\mathrm{ML}} = 1.7$ fs to 3.8 fs. This amounts to a delay shift of 2.1 fs that is expected from pure changes of the interaction strength, which is 1.5 fs above the actual bulk $\delta_{\mathrm{sc}}^{\mathrm{bulk}}$. From this we can conclude that the delay shift caused by changes of the interaction strength is about 40% larger than the shift induced by differences in the band structure. Therefore, the experimentally observed Δt between monolayer and bulk WSe_2 is dominated by changes of the Coulomb interaction strength.

5.6 Tuning correlations

While studying the effect of the Coulomb strength isolated from other factor is trivial in computations, this is a much more challenging endeavor in experiments. To directly access

the effect of the interaction strength also in experiment, we turn to the excitation density. Equation (3.13a) shows that the renormalization term in the Rabi energy, which induces correlations, is prefaced by the so called Pauli-blocking factor $(1 - f_{\mathbf{k}}^{\mathrm{e}} - f_{\mathbf{k}}^{\mathrm{h}})$ with the electron (e) and hole (h) occupations $f_{\mathbf{k}}^{\mathrm{e/h}}$ at wave vector $\mathbf{k}$. In the limit of low densities, this factor equals one and the renormalization term has its full effect. At elevated carrier densities ($f_{\mathbf{k}}^{\mathrm{e/h}} > 0$), the Pauli blocking factor shrinks, effectively reducing the strength of the Coulomb matrix elements $V_{\mathbf{k},\mathbf{k}'}$. By performing experiments at different excitation levels, which can be controlled by the intensity of the NIR field, the effect of the interaction strength on the sub-cycle delay is directly observable.

Limitations in the stability of the experiment did not allow to simply measure the shifts of the subcycle delay as a function of the excitation density. Instead, we devised a series of measurements in which the valleytronic properties of WSe_2 are used to measure a set of relative delay shifts to reveal the density dependence. The strong spin-orbit coupling and broken inversion symmetry of WSe_2 creates inequivalent K and K' points which couple differently to the helicity of circularly polarized light [109, 137]. Resonant excitations of monolayer WSe_2 with circularly polarized light only excites coherent excitons in one of the two valleys. Linearly polarized light on the other hand (which can be viewed as a superposition of both left and right circularly polarized photons) excites both valleys simultaneously with the excitation split evenly between them. As a result, by keeping the NIR-pulse intensity constant, a circularly polarized pulse excites approximately twice as high $f_{\mathbf{k}}^{\mathrm{e/h}}$ compared to a linearly polarized pulse, consequently leading to a stronger reduction of the Coulomb matrix elements $V_{\mathbf{k},\mathbf{k}'}$.

Our experimental collaborators measured and constructed subcycle delay differences Δt between monolayer and bulk samples for excitation with a linearly polarized pulse, Δt^{lin}, and circular excitation, Δt^{circ}. By assuming that the bulk delay $\delta_{\mathrm{sc}}^{\mathrm{bulk}}$ is unchanged as function of the excitation density (which our computations show is true within the experimental

resolution), the difference

$$\Delta t^{\mathrm{circ}} - \Delta t^{\mathrm{lin}} = \delta t_{\mathrm{sc}}^{\mathrm{ML}}(circ) - \delta t_{\mathrm{sc}}^{\mathrm{ML}}(lin) \ , \tag{5.5}$$

directly tracks the shift in the subcycle delay that is caused by Pauli blocking from densities differing by approximately a factor of two.

Figure 5.5 compares the computed (black line) and measured (red dots with error bars) $\Delta t^{\mathrm{circ}} - \Delta t^{\mathrm{lin}}$ difference as function of the total excitation density (among both valleys). As expected, the difference is positive. Circularly polarized light creates an effectively weaker interaction, and a weaker interaction leads to a larger subcycle delay compared to linear excitation. Furthermore, the difference increases with the excitation density because the relative change of the Pauli-blocking factor that the difference compares increases.

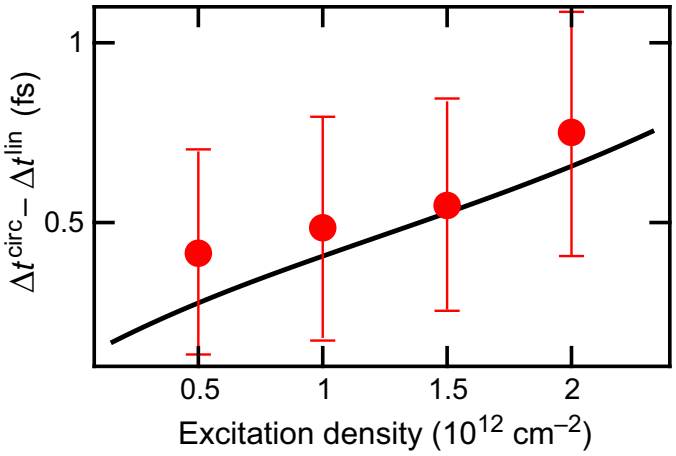

Figure 5.5: Attoclocking of tunable many-body correlations. Difference between bulk and monolayer subcycle delay differences for linearly (Δt^{lin}) and circularly (Δt^{circ}) polarized NIR pulses as function of the excitation density. Measured differences (red circles with error bars) are based on averages over five subcycle delays and compared to computed results (black line).

In conclusion, the interaction strength is tuned by the excitation density, even in experiment, and our attoclocking approach tracks the resulting reduction in correlation strength due to Pauli blocking.

5.7 Attoclocking of phase transitions

Since the attoclocking approach directly detects changes to the strength of correlations, it seems plausible that also other correlation effects such as phase transitions can be investigated. We test this idea for the present system of monolayer WSe_2 by studying the excitonic Mott transition. Figure 5.6 shows the computed subcycle delay δ_{sc} for different Fermi levels which we tune by predicting the electronic fermion degeneracy μ. Experimentally, this could be achieved by electronic doping or pre-exciting the system with a third pulse [138]. The computations predict a discontinuity of δ_{sc} at the Mott transition ($\mu = 1$, vertical dashed line) between the insulating ($\mu < 1$) and metallic phase ($\mu > 1$) of the semiconductor. Furthermore, the two phases are separated by a gap which could be easier to detect experimentally than the discontinuity.

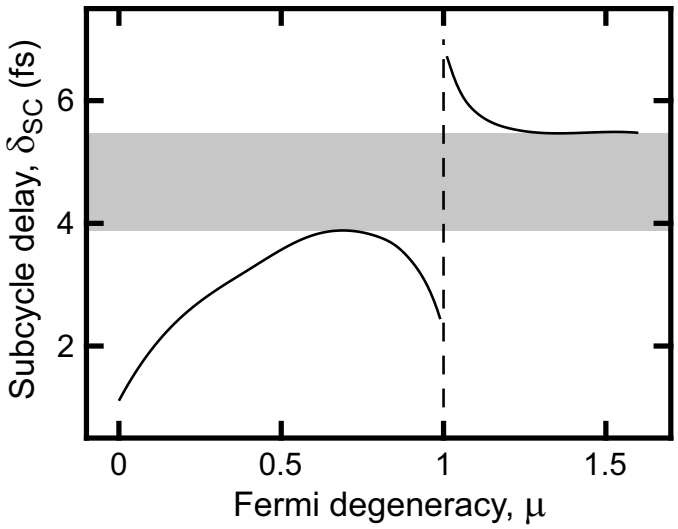

Figure 5.6: Attoclocking of an excitonic Mott transition. Computed subcycle delay δ_{SC} for monolayer WSe_2 as a function of a predicted electronic fermion degeneracy μ. The vertical line marks the Mott transition ($\mu = 1$) and the shaded area marks a gap of subcycle delays that separates the insulating phase ($\mu < 1$) from the metallic phase ($\mu > 1$).

5.8 Attoclocking beyond the subcycle delay

The previous sections used the subcycle delay as a simple measure to connect correlation effects directly to an experimentally observable quantity. It takes the very rich dataset of HSB emission spectra as a function of the excitation time t_{ex} and condenses it into a single number. However, as already discussed in Section 4.5, the HSB spectra are extremely sensitive to both the microscopic properties of the material as well as details of the dynamics. By comparing QDCE computations quantitatively with experimentally recorded HSB spectra, further insights into the microscopic properties are gained. Figure 5.7a (bottom) shows the two-dimensional HSB spectrogram (HSB intensity as a function of the photon energy and the excitation time) measured for a 100 fs long lightwave with peak field strength $E_{\mathrm{THz}} = 6.2$ MV/cm and center frequency $f_{\mathrm{THz}} = 25$ THz. The computed spectrogram (top), using the experimental waveform as an input, achieves an outstanding level of agreement with the experiment, even in absolute units. Both a spectral slice (Fig. 5.7b) and a slice along the t_{ex} direction (Fig. 5.7c) capture all features of the experiment accurately. The effect of the Coulomb strength and dipole matrix elements on HSB spectra has already been shown in Section 4.5 as an extension to lightwave tomography. Similar connections can be found for the measurements of this Section. The time-resolved spectra are sensitive to dynamical processes during the THz generation, which makes them particularly suitable to reveal dephasing and excitation-induced dephasing effects.

QDCE predicts that the back-coupling of higher order correlations (doublets) to the microscopic polarization $P_{\mathbf{k}}$ introduces a scattering with diffusive character that creates a state-dependent dephasing, as discussion in Section 3.4.3. For the experimental conditions considered here, QDCE predicts the lifetime of the $1s$-A exciton to be $\tau = 21.9$ fs while the lifetime of higher order excitons and continuum states are as short as a few fs. This microscopic scattering is especially important in lightwave electronic processes since the lightwave driving of the resonantly excited $1s$ states excites them to higher order excitonic states which experience shorter lifetimes. Effectively, this leads to a strongly time-dependent

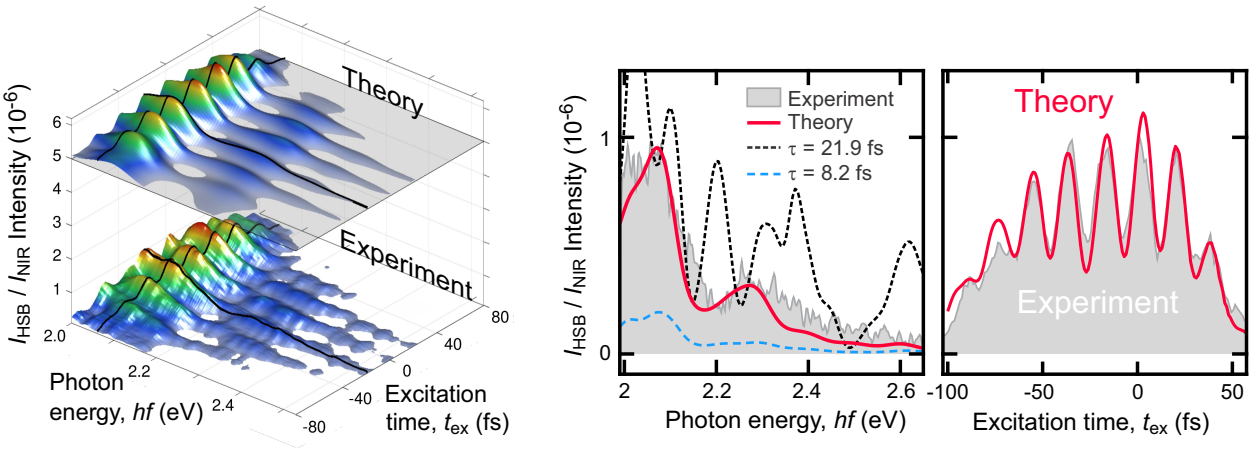

Figure 5.7: Quantitative analysis of many-body aspects in HSB spectrograms of monolayer WSe_2. **a**, Two-dimension HSB spectrogram of WSe_2 as a function of the photon energy hf and the excitation time t_{ex} for a THz waveform with 6.2 MV/cm peak field strength and center frequency of 25 THz. The HSB intensity I_{HSB} is given relative to the intensity of the incident NIR pulse, I_{NIR}, for theory (top, shifted for clarity) and experiment (bottom). The black lines indicate cuts through the spectrogram shown in **b** and **c**. **b**, The measured (shaded area) and computed (red line) HSB spectrum at excitation time $t_{ex} = -19$ fs are compared to computations using a constant phenomenological dephasing with dephasing times $\tau = 21.9$ fs (black dashed line) and $\tau = 8.2$ fs (blue dashed line). **c**, The measured (shaded area) and computed (red line) HSB intensity as function of the excitation time t_{ex} at a fixed photon energy of 2.06 eV.

lifetime.

To illustrate the importance of the microscopic scattering, we compare a spectral slice of the full QDCE computation (Fig. 5.7b, red line) with two computations that use a simplified, constant dephasing model with lifetimes of $\tau = 21.9$ fs (Fig. 5.7b, black dashed line) and $\tau = 8.2$ fs (Fig. 5.7b, blue dashed line). Evidently, only the full QDCE computation accurately reproduces the experiment (Fig. 5.7b, shaded area). The long-lifetime model exhibits many more spectral features while the short lifetime produces a much too low intensity. From this analysis, we can conclude that microscopic scattering in the form of excitation-induced dephasing (EID) clearly shapes the HSB spectra and can be accessed with the help of quantitative theory–experiment comparisons.

5.9 Conclusion and Outlook

We introduced the concept of attosecond chronoscopy to uncover meV-scale many-body correlations of lightwave-driven Bloch electrons directly in the time domain. The correlations of excitonic states were revealed by forcing electron–hole pairs that constitute coherent excitons onto recolliding trajectories and tracking their optimum excitation time for HSB emission. Correlation differences between excitons in bulk and monolayer WSe_2, as well as the tunable reduction of correlations via Pauli-blocking effects were demonstrated. In the future, our attoclocking concept could be extended to study correlation effects of more complex quasiparticles such as biexcitons and dropletons and be used as a correlation probe to study topological and quantum phase transitions. To this end, experimental demonstration of attoclocking of the excitonic Mott transition as proposed in Section 5.7 could be the next logical step.

To understand the intricate many-body dynamics, we employed Wigner functions introduced in Section 5.4 for an intuitive depiction of the full microscopic state in phase space. The Wigner functions reveal that many-body correlations modify the average electron–hole trajectory and also affected the internal state as evidenced by shape changes. In the future, this approach could prove useful in visualizing and innovating new ideas for lightwave processing of quantum information encoded in the microscopic state.

Chapter 6

Prospects and Efficiency of Lightwave Valleytronics

6.1 Introduction

Lightwave electronics promises information processing with PHz clock rates by using the oscillating field of light as a bias to drive electronic states. If such transitions can be driven faster than scattering, even the quantum properties of electronic state can be utilized to possibly enable quantum-information processing in solids. The first lightwave-induced transport at PHz rates was demonstrated in bulk fused silica where carriers were coherently transported across a distance of 500 nm between two gold electrodes [60]. This distance was later extended to multiple microns [139, 140] and contributions to the current originating from intraband transport and polarization-induced currents at the interface with electrodes were distinguished [141]. By using short and asymmetric lightwaves, completely directional transport was achieved [140, 142, 143] where extreme nonlinear effects can restrict coherent charge transport to within the field maximum.

The first steps towards lightwave-based quantum-information processing was achieved by flipping the valley-pseudospin of an excitonic coherence in monolayer WSe_2 on femtosecond time scales [62], much faster than scattering processes that limit the lifetime of quantum

information. The valley pseudospin appears as an additional binary degree of freedom for quasiparticles such as electrons, holes, and excitons in some material classes [109, 137]. This is most famously the case in monolayers of TMDs whose band structures exhibit valleys at the high-symmetry points K and K' in the hexagonal Brillouin zone. The broken inversion symmetry of the crystal structure in combination with time-reversal symmetry creates optical selection rules that couple the helicity of circularly polarized light to the valley-degree of freedom. Light with right-handed, σ^+, (left-handed, σ^-) polarization creates excitations in the K (K') valley, and vice versa, electron–hole recombinations at the K (K') valley emit light with σ^+ (σ^-) polarization. This valley-dependent optical selection rule has been probed in helicity-dependent PL measurements [144–146] and gives direct optical access to the valley-degree of freedom which the field of valleytronics [119, 120] tries to functionalize, for example in designing LEDs [137, 147] and photodetectors [109, 137, 148] for circularly polarized light.

The selection rules give a direct path to converting information encoded in the helicity of light to electronic states and vice versa. However, information processing, manipulation of the valley-degree of freedom, has been explored to a lesser degree so far. In 2016, two groups [149, 150] created a superposition between excitations of the K and K' valley by exciting a monolayer TMD with linearly polarized light. The polarization angle of the superposition state could subsequently be rotated via the optical Stark effect [150–152] or the valley-Zeeman effect [149, 153–157], an operation that resembles a phase gate for qubits.

Based on the first demonstration of ultrafast lightwave switching of the valley-degree of freedom in WSe_2 [62], we theoretically investigate the feasibility and limitations of such switching processes which have the potential for applications in classical and quantum-information processing with PHz clock rates. In order to realize PHz technologies, a hierarchy of milestones need to demonstrated:

1. A single operation can be performed sufficiently fast.

2. A single operation can be performed efficiently.

3. Multiple operations can be chained together into a sequence of operations.

4. The final state can be read out efficiently.

In the subsequent sections, we theoretically investigate several of these steps. We present conditions for efficient lightwave switching of the valley-degree of freedom, present how the lightwaves can be used to precisely control the light reflected from valleytronic materials, and introduce how frequency combs in the reflection spectra of multiple sequenced operations can be analyzed to deduce the temporal structure of the underlying switching sequence.

6.2 Efficiency and optimization of lightwave-valleytronic switching

For this study, we focus on valleytronic materials with a hexagonal lattice structure such as two-dimensional transition metal dichalcogenides and hexagonal boron nitride. The band structure of these materials exhibits valleys at the K and K' point that each host a series of excitonic states [116, 158]. We use the $1s$-excitonic state in each valley as the target states of our lightwave-switching investigations. Their large oscillator strengths let them efficiently interact with light and the optical selection rules make them directly addressable using circularly polarized light.

We study a setup (Fig 6.1a) in which a valley-polarized state is initialized by exciting a valleytronic material with a σ^+-polarized pump pulse that is resonant with the $1s$-excitonic resonance. This excites a wave packet of coherent excitons (described by the microscopic polarization $P_{\mathbf{k}}$ as introduced in Chapter 3) in the $1s$ state (Fig. 6.1b). A subsequent strong lightwave then drives the excitonic wave packet from the K to the K' point, thereby switching the valley polarization. This switch can be detected in the reflected light as a switch of the circular polarization.

Coherent lightwave switching of the valley polarization was first demonstrated by Langer

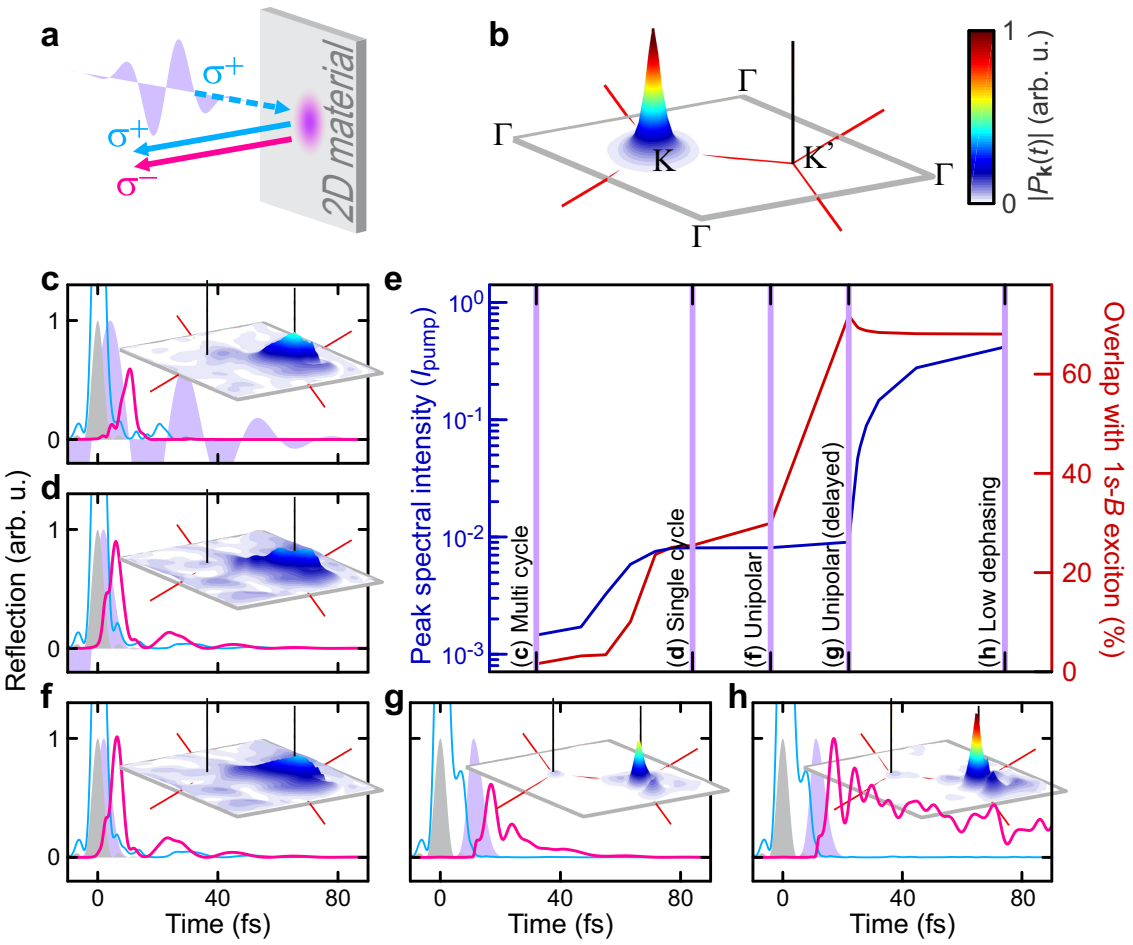

Figure 6.1: Efficiency and optimization of lightwave valleytronic switching. **a**, A σ^+-polarized pump pulse (blue dashed arrow) prepares an initial state by resonantly exciting the 1s-exciton resonance. A subsequent strong lightwave (purple shaded area) switches the valley-degree of freedom which can be detected by a change of the circular polarization of the reflected light (solid arrows) from σ^+ (blue) to σ^- (red). **b**, Microscopic polarization $P_{\mathbf{k}}$ of the 1s-excitonic state of the K valley shown in a rhombic primitive cell (gray lines) with corners at the Γ points (labelled). Red lines show the boundaries of the hexagonal Brillouin zone. The K and K' points are labelled and marked by vertical black lines. **c**, **d**, and **f**–**h**, Reflection dynamics for different realizations of the valleytronic switch. Intensity of the reflected σ^+ (blue line) and σ^--polarized light (red line) after excitation with a σ^+-polarized pump pulse (gray-shaded area) and driving with a linearly polarized lightwave (purple-shaded area) is shown. The inset shows the excitonic wave packet at peak displacement using the same color bar as Panel **a**. **e**, Peak spectral intensity of the σ^--polarized reflected light compared to the pump intensity I_{pump} (blue line on left axis) and overlap between the switched state and target 1s-excitonic state at the K' valley (red line on right axis). The vertical lines mark the cases shown in Panels **c**, **d**, and **f**–**h**. The data between the vertical lines is based on computations for which the parameters have been changed continuously to move from one realization to the next.

et al. [62] in monolayer tungsten diselenide by observing polarization contributions of opposite helicity in harmonic sideband orders. We solve the microscopic quantum dynamics using the semiconductor Bloch equations and compute the optical response as described in Chapter 3. Figure 6.1c shows the optical response (blue line, σ^+-polarized reflection, red line, σ^--polarized reflection) of the valleytronic switch demonstrated by Langer et al. using a multi-cycle lightwave with a pulse length of 50 fs (purple shaded area) and exciting the system near the node of the lightwave with a few-fs long pump pulse (gray shaded area). During the excitation, the reflected light is purely σ^+ polarized. Once the excitonic wave packet is driven to the K' valley (inset shows wave packet at peak displacement), the helicity of the reflected light changes to σ^-. However, the mutli-cycle lightwave can only achieve a transient switch because the oscillating field will drive the wave packet back towards the K valley. As a result, the reflected light only shows a short burst of σ^- emission.

We use two measures to quantify the efficiency of lightwave valleytronic switching:

1. "Spectral efficiency": Peak spectral intensity of the reflected σ^--polarized light compared to the intensity of the σ^+-polarized pump pulse. This measure quantifies how efficiently σ^+-polarized photons are converted into σ^--polarized photons.

2. "Overlap": Overlap between the excitonic wave packet after switching and the $1s$-excitonic state of the K' valley. This measure quantifies the quality of the switch with regards to how much the switched state resembles the target $1s$ state at the K' valley.

For the multi-cycle pulse and the experimental conditions in Langer et al., we find a spectral efficiency in the order of 10^{-3} and an overlap of 1.6% (Fig. 6.1e, blue and red line at the first vertical line).

To achieve a permanent switch of the valley polarization, the pulse length of the lightwave can be reduced to produce single-cycle shape so that the coherent excitons created at the node of the lightwave are only driven by a single half cycle. Figure 6.1d shows computed results for such a single-cycle lightwave. Similar to the multi-cycle lightwave, the polarization

of the reflected light switches with a sharp burst of σ^--polarized light. However, the single-cycle lightwave has a small contribution of lasting σ^- emission which increases the spectral efficiency approximately by a factor of 5 and achieves an overlap of up to 25% (Fig. 6.1e, second vertical line).

Even better control over the valleytronic switch can be achieved by unipolar lightwaves, pulses of light whose electric field only points in one direction and allow for a unidirectional driving of the excitonic wave packets. In the far field, the electric area (electric field strength integrated over time) has to vanish [159], demanding lightwaves to have both positive and negative polarity. However, lightwaves can be shaped into effectively unipolar pulses [112] with a high-amplitude positive peak that is flanked by two long, low-amplitude negative peaks. Furthermore, unipolar pulses could exist in one-dimensional wave guides [160]. Figure 6.1f shows lightwave switching for a perfectly unipolar pulse which achieves very similar efficiencies as the single-cycle pulse (Fig. 6.1e, third vertical line). The efficiency of the current configuration is inherently limited by the pump pulse overlapping with the lightwave, creating a streaked excitonic wave packet that is much broader than the target $1s$ state. However, with a unipolar pulse, pump and lightwave can be temporally separated (Fig. 6.1g) creating a narrow wave packet that resembles the target state much better (Fig. 6.1g, inset). While the spectral efficiency remains almost unchanged, the overlap increases dramatically (Fig. 6.1e, fourth vertical line).

At this point, the main limitation is set by scattering processes that limit the lifetime of coherent excitons and lead to non-radiative losses that reduce the spectral efficiency. The computations in Fig. 6.1c, d, f, and g assume a $1s$ dephasing time of about 60 fs. Reducing the dephasing can greatly enhance the spectral efficiency. For cryogenic temperatures and low excitation powers, dephasing times of up to 1.6 ps have been observed in monolayer $MoSe_2$ [161, 162]. By increasing the dephasing time to 1.6 ps, our computations show a very strong and long lasting σ^- emission (Fig. 6.1h, red line) which boosts the spectral efficiency by a factor of about 46 to a value of 42%. Under these conditions, the spectral intensity of

the reflected light with switched helicity becomes comparable to the intensity of the pump pulse.

6.3 Lightwave control of emission

Using unipolar pulses and valleytronic materials with long coherence lifetimes, the valley polarization can be switched efficiently and the reflected light can reach intensities comparable to the intensity of the pump field. Lightwave switching can be used to precisely control the polarization of the reflected light. Figure 6.2a shows the optical response under the optimized conditions identified in the previous section. After resonant excitation (gray shaded area), the emission without a switching operation (thick blue line) would be purely σ^+ polarized. When an appropriately chosen lightwave (purple shaded area) is applied, the reflected light changes from σ^+ polarization (thin blue line) to σ^- (thin red line). The emission spectrum of the reflected light (Fig. 6.2g, red line) is dominated by a single line at the $1s$ resonance of the K' valley and its intensity is comparable to the σ^+ reflection expected without lightwave switching (Fig. 6.2g, thick light-blue line). The microscopic dynamics of the lightwave switching is most intuitively visualized in phase space using a Wigner-function representation

$$W(\mathbf{r},\mathbf{k}) \equiv \frac{1}{\pi^2}\int \mathrm{d}^2q\,[P_{\mathbf{k}+\mathbf{q}}]^* P_{\mathbf{k}-\mathbf{q}}\mathrm{e}^{-2\mathrm{i}\mathbf{q}\cdot\mathbf{r}}\,, \tag{6.1}$$

of the microscopic polarization $P_{\mathbf{k}}$ where $\hbar\mathbf{k}$ is the crystal momentum and $\mathbf{r}$ is the displacement between the electrons and holes that form coherent excitons. The four-dimensional Wigner function can be reduced to

$$W(x,k_x) \equiv \int \mathrm{d}y\,\mathrm{d}k_y\,W(x,y,k_x,k_y)\,, \tag{6.2}$$

by integrating over $\mathbf{k}$ and $\mathbf{r}$ in y direction and the phase-space dynamics can be further reduced to a simple (x, k_x) trajectory by computing the centroids

$$\langle x \rangle \equiv \int \mathrm{d}x\, x\, W(x, k_x) \text{ , and } \langle k_x \rangle \equiv \int \mathrm{d}k_x\, k_x\, W(x, k_x) \,. \tag{6.3}$$

As discussed in Section 5.4, a microscopic state is bright and emits light when its Wigner function has a contribution at $x = 0$. Figure 6.2b shows snapshots of $W(x, k_x)$ before (black contours near K point) and after lightwave switching (blue–red contours and black contours near K' point) together with its centroid motion (red line) during the switch. The general shape of the centroid can be understood from a semiclassical picture. The lightwave leads to a shift in k_x. The displacement x on the other hand changes with a rate that is given by the group velocity $\mathbf{v}_\mathbf{k} = \frac{1}{\hbar}\nabla_\mathbf{k} E^{\mathrm{eh}}_\mathbf{k}$ of the electron–hole dispersion $E^{\mathrm{eh}}_\mathbf{k}$. When the Wigner function is translated towards K', it first encounters a positive group velocity which increases x. As it transitions into the K' valley, the group velocity changes its sign and electron and hole approach each other again. Ideal switching not only achieves a translation of the excitonic wave packet to the K' point, but also $x = 0$ to realize an optically bright state.

The emission dynamics of the reflected light can be precisely controlled by the use of a second lightwave. For example, by switching the excitonic wave packet back towards its initial state, a short burst of σ^- light is generated (Fig. 6.2c, red line) that is spectrally broad (Fig. 6.2g, dark-blue line) where the length of the light burst is determined by the timing between the two lightwaves. In phase space (Fig. 6.2d), this operation creates a closed loop with the Wigner function returning to its initial state.

A burst-like emission can also be achieved by utilizing the band dispersion in an intriguing way. If the switching is attempted with a lightwave that is too weak, the Wigner function in momentum space is only translated partway to the K' point. However, if the Wigner function that acquired a positive displacement ends up in a region of the band structure with negative group velocity (Fig. 6.2f), the dispersion will move the state towards negative displacement

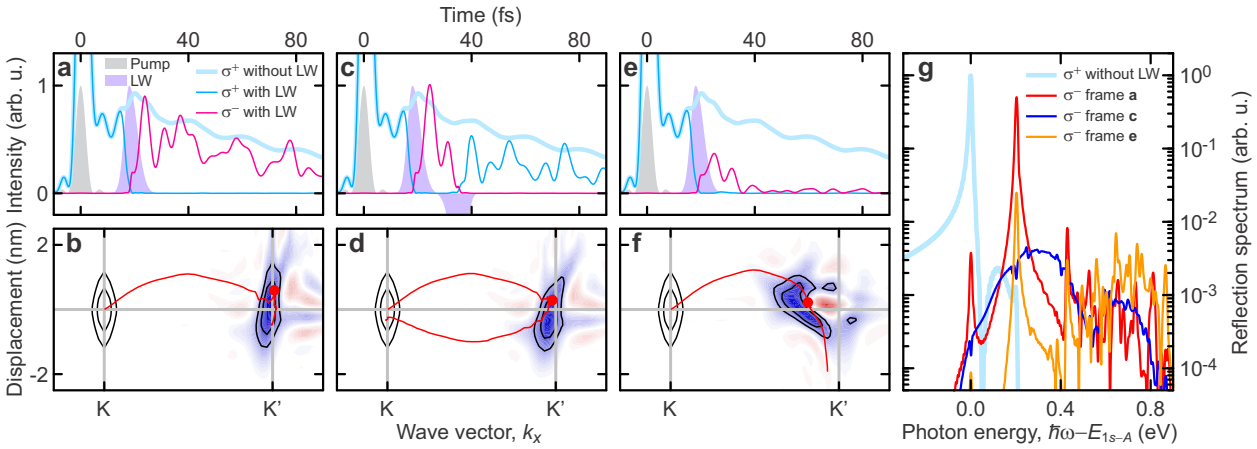

Figure 6.2: Emission modes of reflected light. **a**, **c**, and **e**, Reflection dynamics for different lightwaves (LWs). Spectral intensity of the reflected σ^+ (thin blue line) and σ^--polarized light (red line) after excitation with a σ^+-polarized pump pulse (gray-shaded area) and driving with a linearly polarized lightwave (purple-shaded area) is compared to the σ^+ reflection without switching by a lightwave (thick blue line). **a**, Unipolar pulse for optimum switching; **c**, Two sequenced, unipolar pulses with opposite polarity; **e**, Unipolar pulse with lower intensity compared to case **a**. **b**, **d**, and **f**, The normalized Wigner function $W(x, k_x)$ as function of the electron–hole displacement x and the wave vector k_x of the initial $1s$-excitonic state (black contours near K) are compared to the switched state at peak displacement (black contours and blue–red color map). The red line shows the trajectory of the centroid $[\langle x\rangle(t), \langle k_x\rangle(t)]$; the red dot marks the centroid of the switched state. **g**, The intensity of the σ^+-polarized reflection spectrum (light-blue line) is compared to the σ^--polarized reflection spectra resulting from the temporal dynamics shown in Panels **a**, **c**, and **e** (red, blue, and orange lines).

and create a short emission burst (Fig. 6.2e) when it crosses $x = 0$. Spectrally (Fig. 6.2g, orange line), the emission shows both a narrow emission line (near 0.2 eV) and a broad high energy feature (between 0.4 and 0.8 eV). The high-energy contribution is connected to the short emission burst that is caused by the Wigner function crossing $x = 0$ higher in the bands. The narrow emission line is created by a small contribution of the Wigner function that arrived at K' with $x = 0$ and survives in the $1s$-excitonic state with persistent emission.

6.4 Multi-switch operations

The conditions we identified in Section 6.2 to switch the valleytronic state with lightwaves are efficient enough to allow for sequencing of multiple switch operations within the lifetime

of coherent excitons. Figure 6.3 studies the sequencing of switch pulses with alternating polarity that are 20 fs apart to realize $N = 1, 2, 3, 4$ back-and-forth switches. The coherent excitons (Fig. 6.3a, color map) that are prepared at the K point by a σ^+-polarized pump pulse (Fig. 6.3a, blue shaded area) are precisely driven between the K and K' points by a sequence of unipolar lightwaves (Fig. 6.3a, purple shaded area). In the time domain (Fig. 6.3b), σ^--polarized light is emitted whenever the excitonic wave packet is located at the K' point. As a result, the reflected light appears as a sequence of N, 20 fs long pulses that are spaced 40 fs apart. Because of the finite switching efficiency, coherences are lost with every switch. As a result, the amplitude of each consecutive light pulse is decreased. In the spectral domain (Fig. 6.3c), the sequence of multiple pulses leads to equally spaced frequency lines similar to that of a frequency comb. For such interference patters to occur, the phases of the individual pulses need to be locked relative to each other.

6.4.1 Frequency-comb analysis

For a sequence of equally spaced switch operations, the coherent emission for a given helicity as function of time can be approximated as a train of N pulses

$$E_{\text{train}}(t) = \sum_{n=0}^{N-1} C^n \mathrm{e}^{-\mathrm{i}n\Delta\phi_{\text{CEP}}} E_{\text{pulse}}(t - n\Delta t) \ , \tag{6.4}$$

where each consecutive pulse is delayed by Δt, decreases in amplitude by a factor of C, and exhibits a shift of its carrier-envelope phase (CEP) by $\Delta\phi_{\text{CEP}}$. $E_{\text{pulse}}(t)$ is the amplitude of the first pulse in the sequence. The spectrum of the this sequence can be computed analytically and results in

$$E_{\text{train}}(\omega) = E_{\text{pulse}}(\omega) * g(\omega) \ , \tag{6.5}$$

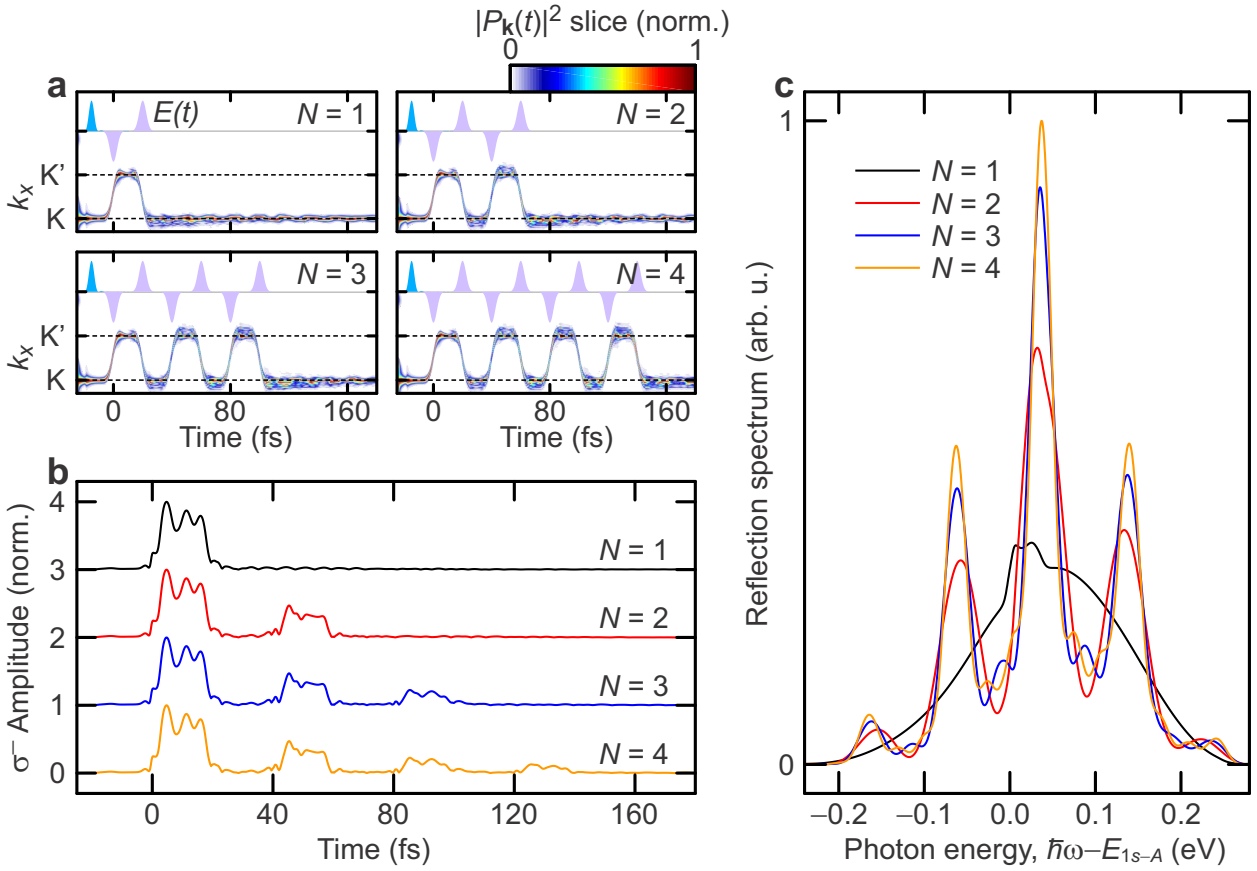

Figure 6.3: Sequencing of multiple switch operations. **a**, After excitation with a σ^+-polarized pump (blue shaded area), a sequence of $N = 1, 2, 3, 4$ pairs of switching pulses (purple shaded area) is applied to switch the valley-degree of freedom by driving coherent excitons (color map shows slice of $P_{\mathbf{k}}$ through the K and K' points along the k_x direction that is normalized at each time) back and forth between K and K' as a function of time. **b**, Normalized amplitude of the reflected σ^--polarized light for $N = 1, 2, 3, 4$. The curves are shifted vertically to increase visibility. **c**, Reflected intensity spectra of the σ^--polarized light for $N = 1, 2, 3, 4$.

where $E_{\text{pulse}}(\omega)$ is the Fourier transformation of the individual pulse $E_{\text{pulse}}(t)$ that is modulated by the periodic function

$$g(\omega) = \frac{1 - C^n - 2\mathrm{i}C^n \mathrm{e}^{\mathrm{i}N(\omega\Delta t - \Delta\phi_{\text{CEP}})/2} \sin\left[N(\omega\Delta t - \Delta\phi_{\text{CEP}})/2\right]}{1 - C^n - 2\mathrm{i}C^n \mathrm{e}^{\mathrm{i}(\omega\Delta t - \Delta\phi_{\text{CEP}})/2} \sin\left[\omega\Delta t - \Delta\phi_{\text{CEP}})/2\right]}\,, \tag{6.6}$$

which exhibits equally spaced frequency lines with periodicity $2\pi/\Delta t$ in ω. Instead of Dirac-delta-function like lines that appear in the limit of $C = 1$ and $N \to \infty$, a finite number of pulses with decreasing amplitudes create lines with a finite width and contrast. An example

$|g(\omega)|^2$ for $\Delta\phi_{\mathrm{CEP}} = 0.6\,\pi$, $C = 0.6$, and $N = 5$ is shown in Fig. 6.4.

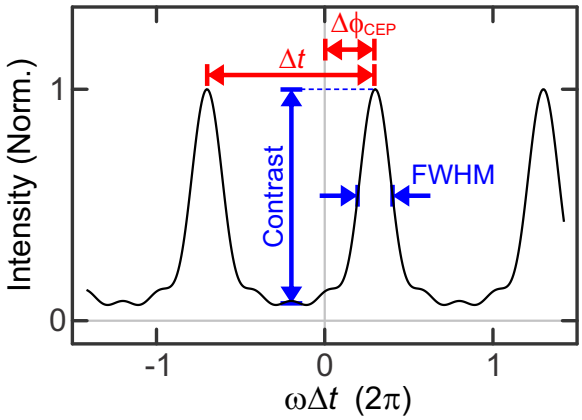

Figure 6.4: Frequency-comb analysis. A plot of $|g(\omega)|^2$ for $\Delta\phi_{\mathrm{CEP}} = 0.6\,\pi$, $C = 0.6$, and $N = 5$. A set of quantities are labelled that can be used to deduce information about the temporal signal that created the frequency comb.

Similar to frequency combs, the spacing of the frequency lines is determined by the temporal spacing Δt of the pulses and the shift of the lines relative to zero frequency is determined by $\Delta\phi_{\mathrm{CEP}}$. Furthermore, the contrast (relation of maximum and minimum intensities) and the width of the frequency lines are directly connected to C and N. As a result, temporal information about the pulse sequence can be obtained from a measurement of the reflection spectrum by analyzing the emergent frequency comb.

6.4.2 Fourier analysis of the frequency comb

The optical response in the time ($E(t)$) and frequency domain ($E(\omega)$) are connected by a Fourier transformation. However, experiments usually measure intensities $|E|^2$ that lack phase information contained in E. In general, information about the temporal emission dynamics $|E(t)|^2$ cannot easily be obtained from an intensity spectrum $|E(\omega)|^2$. Interestingly, this is different for the specific optical response created by the switching operations introduced earlier. Because the first emission burst in the sequence is larger than the remaining ones, a Fourier transformation of the intensity spectrum $|E(\omega)|^2$ back into the time domain closely reproduces the amplitude $|E(t)|$.

Figure 6.5a tests this approach using a sequence of $N = 16$ back-and-forth switches which creates a frequency comb in the spectral domain (Fig. 6.5c, black line). The Fourier transformation of the intensity spectrum (Fig. 6.5a, black line) closely resembles the actual amplitude $|E(t)|$ (Fig. 6.5a, gray line) of the reflected light and reproduces the emission sequence. For the comparison, we shifted the Fourier-transformed signal to align with the actual field. The lack of phase information of the reflection spectrum does not allow to settle the absolute timing of the emission, however, the relative timing of the individual bursts is reproduced.

To test this approach further, we modify the switching sequence to skip the fourth switch (Fig. 6.5b). The altered sequence leads to changes in the intensity spectrum (Fig. 6.5c, red line) and the skipped emission pulse (Fig. 6.5b, thick red line) is faithfully captured by the Fourier transformation of the intensity spectrum (Fig. 6.5b, thin red line).

6.5 Conclusion

In this Chapter, we theoretically studied the potential of lightwave valleytronics for information processing with PHz clock rates. The valley-degree of freedom of coherent excitons in valleytronic materials can be switched using strong lightwaves and detected by a change of the circular polarization of the reflected light. We found that the efficiency of valleytronic switching strongly depends on the shape of the lightwave as well as on material properties such as dephasing, both of which can be optimized to achieve emission from the switched state with high intensities. The optimized conditions were used to show that valleytronic switching can be applied to precisely control the light reflected from a valleytronic material. Furthermore, we showed that under such conditions, the developed switch is sufficiently efficient to sequence multiple switches within the lifetime of coherent excitons. For periodic switching of the valleytronic state, the reflected light emits a train of light pulses which create a frequency comb in the spectral domain and we outlined how this frequency comb

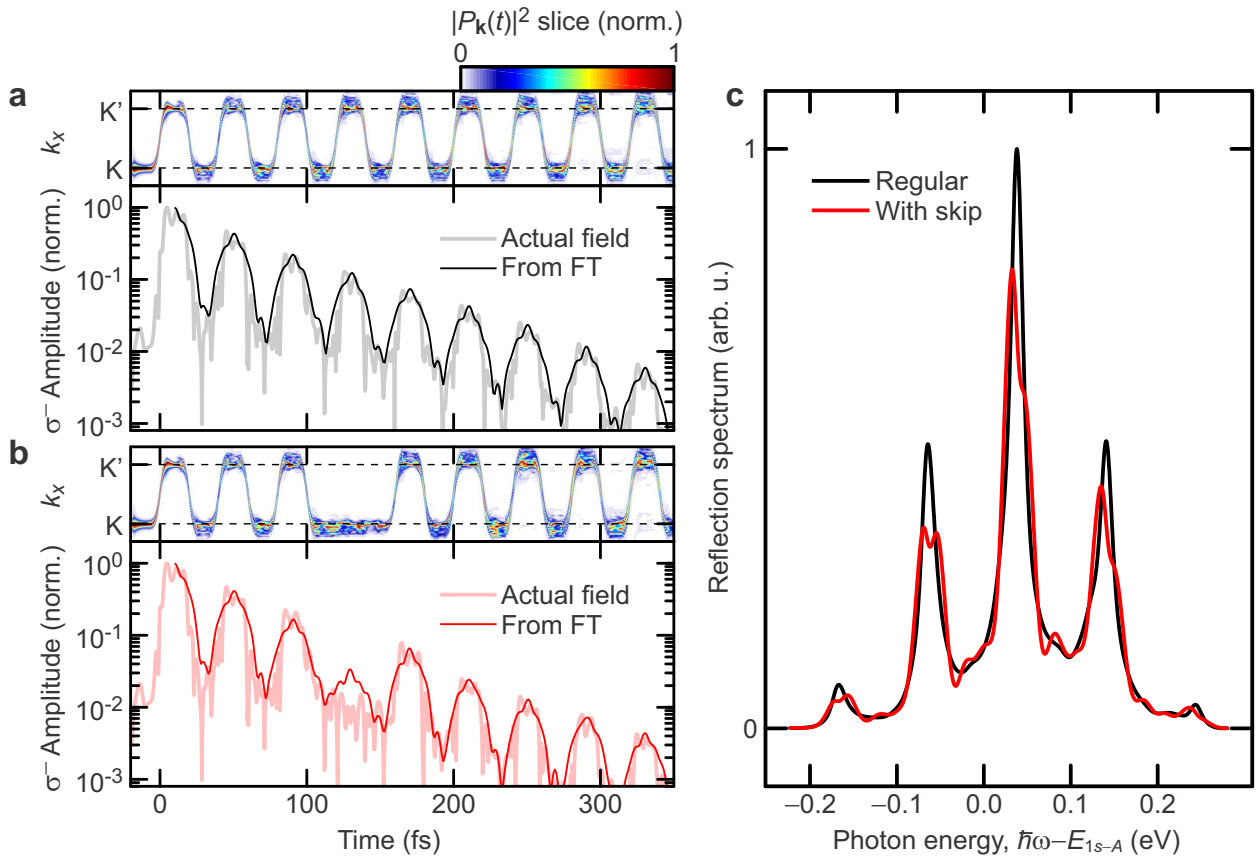

Figure 6.5: Fourier-analysis of emergent frequency combs. **a**, A sequence of $N = 16$ pairs of unipolar lightwaves with alternating polarity is used to drive coherent excitons (top, color map shows slice of $P_{\mathbf{k}}$ through the K and K' points along the k_x direction that is normalized at each time) between K and K' as function of time. The dynamics is compared to the σ^--polarized reflected field (shaded line) and the Fourier transformation of the reflected σ^--polarized intensity spectrum (thin line, shifted in time for alignment). **b**, Same analysis as Panel **a** but for a sequence of lightwaves that skips the fourth pair. **c**, Cross comparison of the reflected σ^--polarized intensity spectra with (black line) and without (red line) the 4th pair of switches.

could be used in future experiments to demonstrate successful sequencing of multiple valleytronic switches. In the future, this investigation should be extended to propose explicit excitation schemes and materials that can be realized and used in present-day experiments to demonstrate the sequencing of multiple valleytronic switches. In order to become applicable for information processing, algorithms have to be developed that utilize the valley-degree of freedom. To that end, development of a scheme for conditional switching would be an important step to realize useful classical or quantum gate operations.

Chapter 7

Microscopic Theory of Spatially Inhomogeneous Excitations and Nanostructures

7.1 Introduction

The QDCE approach described in Section 2 can straightforwardly be applied to derive a general set of equations of motion that describe any and all effects observable in condensed matter systems. The challenge posed to theorists is to find solutions of those equations. Analytic solutions only exist for a limited set of special cases. The only path to general solutions are given by numerical methods whose capabilities are restricted by the computational resources available. A brute-force approach of implementing the most general QDCE equations is not feasible as its demand on computational power easily exceeds that of the most powerful supercomputers.

To solve this predicament, the system in question and the equations that describe it have to be carefully studied and symmetries and approximations identified that reduce degrees of freedom and complexity. The random-phase approximation [69], which enforces position independence, significantly reduces the dimensionality of the problem and is commonly used such as in our description of lightwave-electronic processes in Chapter 3. The decision which

approximations to apply needs to be made on a case-by-case basis to find a reasonable balance between numerical feasibility and a correct description of the relevant physical processes.

In this Chapter, we derive a QDCE-based microscopic theory to describe spatially inhomogeneous excitations in semiconductors and nanostructures. The many-body state is represented by clusters in a Wigner-function form [136, 163, 164] which separates macroscopic spatial degrees of freedom from those of the microscopic ones encoding the internal quantum state. The theory is derived for a generic direct-gap semiconductor described by two parabolic bands. The separation of length scales by the Wigner function, combined with the reduced semiconductor model, allows for both numerical and analytical investigations to identify key physical effects relevant for spatially inhomogeneous systems which are discussed in Chapters 8 and 9.

7.2 Hamiltonian

Instead of the Hamiltonian in Eq. (2.2), we start from the reduced Hamiltonian

$$\hat{H} = \hat{H}_0 + \hat{H}_{\mathrm{e-e}} + \hat{H}_{\mathrm{LM}} \,, \tag{7.1}$$

which we represent in second quantization using the fermionic field operators

$$\hat{\Psi}^\dagger_\lambda(\mathbf{r}) \equiv \frac{1}{\mathcal{S}} \sum_{\mathbf{k}} \mathrm{e}^{-\mathrm{i}\mathbf{k}\cdot\mathbf{r}} a^\dagger_{\lambda,\mathbf{k}} \,, \quad \text{and} \quad \hat{\Psi}_\lambda(\mathbf{r}) \equiv \frac{1}{\mathcal{S}} \sum_{\mathbf{k}} \mathrm{e}^{\mathrm{i}\mathbf{k}\cdot\mathbf{r}} a_{\lambda,\mathbf{k}} \,, \tag{7.2}$$

that create and annihilate an electron at position $\mathbf{r}$ in the λ band, respectively, and satisfy the anti-commutation relations

$$\left\{\hat{\Psi}_\lambda(\mathbf{r}), \hat{\Psi}^\dagger_\nu(\mathbf{r}')\right\} = \delta_{\lambda,\nu}\delta(\mathbf{r}-\mathbf{r}') \,, \quad \left\{\hat{\Psi}_\lambda(\mathbf{r}), \hat{\Psi}_\nu(\mathbf{r}')\right\} = 0 \,, \quad \left\{\hat{\Psi}^\dagger_\lambda(\mathbf{r}), \hat{\Psi}^\dagger_\nu(\mathbf{r}')\right\} = 0 \,, \tag{7.3}$$

where $\{a, b\} \equiv ab + ba$ denotes the anticommutator between a and b. The single-particle Hamiltonian is given by

$$\hat{H}_0 = \sum_{\lambda} \int \mathrm{d}^3 r \, \hat{\Psi}^\dagger_\lambda(\mathbf{r}) \left[E_\lambda - \frac{\hbar^2}{2m_\lambda} \nabla^2_{\mathbf{r}} + U_\lambda(\mathbf{r}) \right] \hat{\Psi}_\lambda(\mathbf{r}) \, , \tag{7.4}$$

and describes parabolic bands $E_{\lambda,\mathbf{k}} = \frac{\hbar^2 \mathbf{k}^2}{2m_\lambda}$ with effective mass m_λ where $\lambda = v, c$ is the band index. The two bands are separated by a direct gap $E_{\mathrm{gap}} = E_c - E_v$. $U_\lambda(\mathbf{r})$ is an external potential. The light–matter Hamiltonian

$$\hat{H}_{\mathrm{LM}} = - \sum_{\lambda \neq \lambda'} \int \mathrm{d}^3 r \, \hat{\Psi}^\dagger_\lambda(\mathbf{r}) dE(\mathbf{r}, t) \hat{\Psi}_{\lambda'}(\mathbf{r}) \, , \tag{7.5}$$

includes the dipole interaction to describe interband excitations. We assume a constant dipole d and only take into account the field strength $E(\mathbf{r}, t)$ of the electric. The polarization dependence is neglected without loss of generality. Lightwave effects such as described in Section 3.5 are neglected here. Finally, the electron–electron interaction is fully included by

$$\hat{H}_{\mathrm{e-e}} = \frac{1}{2} \sum_{\lambda\lambda'} \int \mathrm{d}^3 r \, \mathrm{d}^3 r' \, \hat{\Psi}^\dagger_\lambda(\mathbf{r}) \hat{\Psi}^\dagger_{\lambda'}(\mathbf{r}') V(\mathbf{r} - \mathbf{r}') \hat{\Psi}_{\lambda'}(\mathbf{r}') \hat{\Psi}_\lambda(\mathbf{r}) \, , \tag{7.6}$$

with the Coulomb potential $V(\mathbf{r}) = \frac{|e|^2}{4\pi\varepsilon\varepsilon_0} \frac{1}{|\mathbf{r}|}$ between two electrons separated by the distance $\mathbf{r}$ with the electron charge e, the relative permittivity of the material ε and the vacuum permittivity ε_0.

7.3 Wigner representation of singlets and doublets

The many-body state can be represented in many different ways, depending on the set of basis states chosen, and must capture both the nanometer-scale correlations of quasiparticles and spatial changes on the scale of micrometers at the same time. These two length scales of correlations between two electrons at positions $\mathbf{r}_1$ and $\mathbf{r}_2$ are most easily separated by

introducing the relative coordinate $\mathbf{r} = \mathbf{r}_2 - \mathbf{r}_1$ and the center-of-mass (COM) coordinate $\mathbf{R} = (\mathbf{r}_1 + \mathbf{r}_2)/2$. Long-range spatial inhomogeneities are then described by $\mathbf{R}$ while the short range correlations are captured by $\mathbf{r}$. To ultimately separate these two coordinates we use a Wigner-function representation [136, 163, 164] which transforms $\mathbf{r}$ into momentum space with wave vector $\mathbf{k}$. Explicitly, we introduce the microscopic single-particle operator between bands λ and ν as

$$\hat{P}_{\mathbf{k}}^{\lambda,\nu}(\mathbf{R}) \equiv \int \mathrm{d}^3 r \, \hat{\Psi}_{\lambda}^{\dagger}(\mathbf{R} - F_{\lambda,\nu}\mathbf{r})\hat{\Psi}_{\nu}(\mathbf{R} + F_{\nu,\lambda}\mathbf{r})\mathrm{e}^{-\mathrm{i}\mathbf{k}\cdot\mathbf{r}} \, . \tag{7.7}$$

This definition applies the correct COM coordinates and takes into account the effective electron masses in the valence and conduction bands via the weights $F_{\lambda,\nu} \equiv \frac{|m_\nu|}{|m_\lambda|+|m_\nu|}$.

Singlet quantities equivalent to the microscopic polarization $P_{\mathbf{k}}$ and the electron and hole occupations $f_{\mathbf{k}}^{\mathrm{e}}$ and $f_{\mathbf{k}}^{\mathrm{h}}$ used in lightwave SBEs introduced in Section 3.4.1 are identified from Eq. (7.7) by

$$P_{\mathbf{k}}(\mathbf{R}) \equiv \left\langle \hat{P}_{\mathbf{k}}^{v,c}(\mathbf{R}) \right\rangle \, , f_{\mathbf{k}}^{\mathrm{e}}(\mathbf{R}) \equiv \left\langle \hat{P}_{\mathbf{k}}^{c,c}(\mathbf{R}) \right\rangle \, , f_{\mathbf{k}}^{\mathrm{h}}(\mathbf{R}) \equiv 1 - \left\langle \hat{P}_{\mathbf{k}}^{v,v}(\mathbf{R}) \right\rangle \, . \tag{7.8}$$

Introduction of the Wigner function allows for a simple interpretation of the singlets by adding a spatial coordinate $\mathbf{R}$ to the singlets that are otherwise familiar from the homogeneous investigations of Chapter 3. The Wigner-function approach is also extended for the exciton doublet

$$c_X^{\mathbf{k},\mathbf{k}',\mathbf{Q}}(\mathbf{R}) \equiv \frac{1}{S} \int \mathrm{d}^3 r \, \Delta \left\langle \hat{P}_{\mathbf{k}}^{\dagger}(\mathbf{R} - \mathbf{r}/2)\hat{P}_{\mathbf{k}'}(\mathbf{R} + \mathbf{r}/2) \right\rangle \mathrm{e}^{-\mathrm{i}\mathbf{Q}\cdot\mathbf{r}} \, , \tag{7.9}$$

which describes incoherent excitons. The definition is chosen such that the new quantity resembles the $c_X^{\mathbf{k},\mathbf{k}',\mathbf{Q}}$ defined for homogeneous systems [70] and generalizes it by adding a spatial coordinate.

7.4 Cluster dynamics

The equations of motion for the quantities defined in Eqs. (7.8) and (7.9) are computed from the Heisenberg equation of motion (2.4) by utilizing the fermionic anticommutation relations (7.3) for the field operators. The exact singlet dynamics is summarized in Appendix F and contains operators of the form

$$\mathrm{e}^{\mathrm{i}\alpha\nabla_{\mathbf{k}}\cdot\nabla_{\mathbf{R}}} = 1 + \mathrm{i}\alpha\nabla_{\mathbf{k}}\cdot\nabla_{\mathbf{R}} + \mathcal{O}(\alpha^2)\ . \tag{7.10}$$

Expanding the exponential function in a power series renders the equations of motion into a more physical form that is easier to interpret. For the remainder of this Chapter, we consider the lowest order terms in the power expansion as well as a selection of higher order terms which we found to dominate the spatial dynamics.

For the microscopic polarization, we find

$$\mathrm{i}\hbar\frac{\partial}{\partial t}P_{\mathbf{k}}(\mathbf{R}) = \widetilde{E}_{\mathbf{k}}(\mathbf{R})P_{\mathbf{k}}(\mathbf{R}) - \big[1 - f^{\mathrm{e}}_{\mathbf{k}}(\mathbf{R}) - f^{\mathrm{h}}_{\mathbf{k}}(\mathbf{R})\big]\Omega_{\mathbf{k}}(\mathbf{R}) - \mathrm{i}\Gamma^{vc}_{\mathbf{k}}(\mathbf{R}) \tag{7.11a}$$

$$- \frac{\hbar^2}{2M}\nabla^2_{\mathbf{R}}P_{\mathbf{k}}(\mathbf{R}) + \mathrm{i}\nabla_{\mathbf{R}}U_{\mathrm{eff}}(\mathbf{R})\cdot\nabla_{\mathbf{k}}(\mathbf{R}) + \dots\ , \tag{7.11b}$$

where the first line (Eq. 7.11a) closely resembles the SBEs for homogeneous systems with the renormalized kinetic energy $\widetilde{E}_{\mathbf{k}}(\mathbf{R})$, the renormalized Rabi energy $\Omega_{\mathbf{k}}(\mathbf{R})$, and a coupling to higher order clusters $\Gamma^{vc}_{\mathbf{k}}(\mathbf{R})$, as defined in Appendix G. The additional terms in Eq. (7.11b) contain gradients with respect to the position $\mathbf{R}$ which makes them sensitive to spatial variations within the system. The shown gradient terms resemble the Schrödinger equation of a particle in an external potential $U_{\mathrm{eff}}(\mathbf{R})$ and dominate the spatial dynamics of $P_{\mathbf{k}}(\mathbf{R})$. The full equations of motion up to the first order of the power expansion (7.10) as well as definitions for all symbols are shown in Appendix G.

A similar equation structure can be found for the electron occupation

$$\hbar\frac{\partial}{\partial t}f_{\mathbf{k}}^{\mathrm{e}}(\mathbf{R}) = 2\mathrm{Im}[P_{\mathbf{k}}(\mathbf{R})\Omega_{\mathbf{k}}^{*}(\mathbf{R})] + 2\mathrm{Im}\left[\sum_{\mathbf{q},\mathbf{Q}} V_{\mathbf{k}-\mathbf{q}} c_X^{\mathbf{q},\mathbf{k},\mathbf{Q}}(\mathbf{R})\right] \tag{7.12a}$$

$$- \frac{\hbar^2}{m_{\mathrm{e}}}\mathbf{k}\cdot\nabla_{\mathbf{R}} f_{\mathbf{k}}^{\mathrm{e}}(\mathbf{R}) + \nabla_{\mathbf{R}} U_{\mathrm{eff,e}}(\mathbf{R})\cdot\nabla_{\mathbf{k}} f_{\mathbf{k}}^{\mathrm{e}}(\mathbf{R}) + \dots \ , \tag{7.12b}$$

and the incoherent exciton doublet (in the main-sum approximation [70])

$$\begin{aligned}\hbar\frac{\partial}{\partial t}c_X^{\mathbf{k},\mathbf{k}',\mathbf{Q}}(\mathbf{R}) = {}& \mathrm{i}\Big[\widetilde{E}_{\mathbf{k}}(\mathbf{R}) - \widetilde{E}_{\mathbf{k}'}(\mathbf{R})\Big] c_X^{\mathbf{k},\mathbf{k}',\mathbf{Q}}(\mathbf{R}) + S[P_{\mathbf{k}}(\mathbf{R})] - \gamma_X c_X^{\mathbf{k},\mathbf{k}',\mathbf{Q}}(\mathbf{R}) \\ & + \mathrm{i}\big[1 - f_{\mathbf{k}'}^{\mathrm{e}}(\mathbf{R}) - f_{\mathbf{k}'}^{\mathrm{h}}(\mathbf{R})\big] \sum_{\mathbf{q}} V_{\mathbf{k}'-\mathbf{q}} c_X^{\mathbf{k},\mathbf{q},\mathbf{Q}}(\mathbf{R}) \\ & - \mathrm{i}\big[1 - f_{\mathbf{k}}^{\mathrm{e}}(\mathbf{R}) - f_{\mathbf{k}}^{\mathrm{h}}(\mathbf{R})\big] \sum_{\mathbf{q}} V_{\mathbf{k}-\mathbf{q}} c_X^{\mathbf{q},\mathbf{k}',\mathbf{Q}}(\mathbf{R}) \qquad (7.13a) \\ & - \frac{\hbar^2}{M}\mathbf{Q}\cdot\nabla_{\mathbf{R}} c_X^{\mathbf{k},\mathbf{k}',\mathbf{Q}}(\mathbf{R}) + \nabla_{\mathbf{R}} U_{\mathrm{eff,X}}(\mathbf{R})\cdot\nabla_{\mathbf{Q}} c_X^{\mathbf{k},\mathbf{k}',\mathbf{Q}}(\mathbf{R}) + \dots \ , \qquad (7.13b)\end{aligned}$$

where Eq. (7.12a) and (7.13a) resemble the homogeneous SBEs [70], and (7.12b) and (7.13b) introduce additional gradient terms with respect to the position $\mathbf{R}$, respectively. For these incoherent quantities, the dominant gradient terms resemble the Liouville equation of a classical distribution of particles in phase space moving in an external potential $U_{\mathrm{eff,e/X}}$. Since the *semiconductor Bloch equations* (SBEs) are usually discussed in the context of homogeneous conditions, we will refer to Eqs. (7.11–7.13) as the *inhomogeneous semiconductor Bloch equations* (inhomogeneous SBEs) from here on.

7.5 Numerical solution

We transform equations (7.11–7.13) for a strictly two-dimensional system into polar coordinates and apply a Fourier mode expansion of the form

$$W(\mathbf{k},\mathbf{R}) = W(k,\varphi_k,R,\varphi_R) = \sum_{m_k,m_R} |k^{m_k}R^{m_R}|\ W_{m_k,m_R}(k,R)\ \mathrm{e}^{\mathrm{i}(m_k\varphi_k + m_R\varphi_R)} \ , \tag{7.14}$$

which follows the numerical approach of "spectral methods" [97]. The resulting equations of motion of the scaled Fourier coefficients $W_{m_k,m_R}(k,R)$ are solved numerically using the 4th order Runge-Kutta method [97] for finite m_k and m_R and discretized k and R coordinates. For an extended discussion of the numerical implementation and challenges, we refer the reader to Ref. [165]. This Fourier-mode representation is particularly well suited for systems with rotational symmetry that are analyzed in Chapter 8. In those cases, only few $m_{k/R}$ states are required to converge numerical results.

Chapter 8

Spatial Dynamics of Coherent Excitons

8.1 Introduction

We study the effect of spatial inhomogeneities on ultrafast time scales by investigating the excitation dynamics of a spatially local excitation. GaAs quantum wells are chosen as a model system which are accurately described by a two-band model with parabolic bands as long as excitations near the optical gap are considered. Explicitly, we study the spatio-temporal dynamics of coherent excitons described by the microscopic polarization $P_{\mathbf{k}}(\mathbf{R})$ after excitation of the $1s$-excitonic resonance with an ultrashort and tightly focused Gaussian laser pulse. Spatial inhomogeneities are introduced by the excitation itself while the GaAs quantum well is assumed homogeneous in space. Our theoretical investigations include analytical and numerical studies of the inhomogeneous SBEs introduced in Chapter 7 and are focused on the macroscopic polarization density

$$P(\mathbf{R}) \equiv \frac{1}{\mathcal{S}} \sum_{\mathbf{k}} dP_{\mathbf{k}}(\mathbf{R}) \; , \tag{8.1}$$

with the quantization area $\mathcal{S}$, and the electron and hole density

$$n^{\mathrm{e/h}}(\mathbf{R}) \equiv \frac{1}{\mathcal{S}} \sum_{\mathbf{k}} f_{\mathbf{k}}^{\mathrm{e/h}}(\mathbf{R}) \; , \tag{8.2}$$

in space. These two distributions are physical observables and are, in principle, measurable by experiments.

8.2 Nonlinear effects on spatial distributions

The (homogeneous) SBEs have been applied and discussed in great detail, for example in Refs. [41, 47, 52, 59, 69, 70, 87, 112, 166, 167], but also in the Chapters 3–5 of this Thesis. As shown in Section 7.4, they appear as part of the inhomogeneous SBEs and describe the excitation dynamics locally, including nonlinear effects which can impact spatial distributions. In the linear regime, the polarization density $P(\mathbf{R})$ follows the spatial profile of the pump pulse $E(\mathbf{R})$, meaning that $P(\mathbf{R}) \propto E(\mathbf{R})$. Similarly, the carrier density is expected to follow $n(\mathbf{R}) \propto |E(\mathbf{R})|^2$. Nonlinear effects such as excitation-induced dephasing [167, 168] (EID) and excitation-induced shifts [167, 169] (EIS) emerge at elevated excitation densities. For a pump pulse with Gaussian profile, nonlinear effects are expected to be strongest in the center of the excitation spot (where $n(\mathbf{R})$ is largest) and weaker in the tail. EID can be observed as dephasing of the polarization density which increases as function of the carrier density. For an initially Gaussian spot of polarization, this means that polarization in the center decays faster than at the tail regions. This flattens the top of the distribution and changes the shape to deviate from the expected Gaussian shape, effectively broadening the excitation spot as a function of time. Another important nonlinear effect that influences the polarization distribution is EIS. Resonant excitations of the GaAs quantum well create a microscopic polarization that oscillates with the $1s$-resonance frequency. However, in the presence of carrier density, this frequency shifts. Again, for a Gaussian excitation, the nonlinear shift of the oscillation frequency is strongest in the center of the distribution. As a result, the polarization distribution will oscillate with different frequencies at different positions which induces a spatial chirp that accumulates over times.

It is important to note that the spatial changes described above are entirely explained

by nonlinear effects which only depend on the local density and are independent of the spatial scale. In contrast, the goal of this Chapter is to explore the effects that distributions experience on the shortest of length scales where the homogeneous SBEs break down. Those effects will exhibit a dependence on the length scale of spatial variations such as the size of the pump spot. This can be used as a condition to identify true inhomogeneous effects also in experiment.

8.3 Polarization dynamics

A careful numerical study of the inhomogeneous SBEs reveals that the spatial dynamics of $P(\mathbf{R})$ is clearly dominated by the first term of Eq. (7.11b). To better understand its effect, we isolate the term and consider the reduced equation of motion

$$\mathrm{i}\hbar\frac{\partial}{\partial t}P_{\mathbf{k}}(\mathbf{R}) = -\frac{\hbar^2}{2M}\nabla^2_{\mathbf{R}}P_{\mathbf{k}}(\mathbf{R})\ . \tag{8.3}$$

By summing over $\mathbf{k}$, the dynamics of the macroscopic polarization density yields

$$\mathrm{i}\hbar\frac{\partial}{\partial t}P(\mathbf{R}) = -\frac{\hbar^2}{2M}\nabla^2_{\mathbf{R}}P(\mathbf{R})\ , \tag{8.4}$$

which is equivalent to the free Schrödinger equation of a particle with mass M. We can conclude that the macroscopic polarization density in space behaves similar to a quantum mechanical wave packet.

From basic quantum mechanics it is known that a Gaussian wave packet with initial width ΔR evokes an expansion:

$$P(\mathbf{R}; t=0) \propto \mathrm{e}^{-\frac{\mathbf{R}^2}{2\Delta R^2}}\ , \tag{8.5}$$

$$\Rightarrow\quad \Delta R(t) = \Delta R\sqrt{1+\left(\frac{\hbar}{M\Delta R^2}t\right)^2}\ , \tag{8.6}$$

where $\Delta R(t)$ is the width of the distribution as a function of time. Furthermore, if the wave packet is modulated with a phase $\mathrm{e}^{\mathrm{i}\mathbf{k}\cdot\mathbf{R}}$, it is translated linearly as a function of time which can be associated with a momentum.

As discussed in Section 8.2, nonlinear effects such as EIS can induce a spatial chirp of the polarization wave packet. Due to the symmetry of our setup (excitation with a Gaussian, rotationally symmetric pulse) the spatial phase changes will be of the form $\mathrm{e}^{\mathrm{i}\varphi(R)}$ with radial symmetry. From a wave-packet point of view, this radial phase can be interpreted as a radial momentum which, depending on the sign, can lead to an expansive or contractive motion of the wave packet. For a Gaussian wave packet with $\varphi(R) = \alpha R^2/\Delta R^2$, where α determines the amount of chirp, Eq. (8.4) can be solved analytically and the width dynamics results in

$$P(\mathbf{R}; t = 0) \propto \mathrm{e}^{-\frac{\mathbf{R}^2}{2\Delta R^2} + \mathrm{i}\varphi(R)} , \tag{8.7}$$

$$\Rightarrow \quad \Delta R(t) = \Delta R \sqrt{1 + \alpha \frac{\hbar t}{M \Delta R^2} + (1 + \alpha^2) \left(\frac{\hbar t}{M \Delta R^2} \right)^2} . \tag{8.8}$$

The solution shows that the sign of α determines the direction of $\Delta R(t)$ changes at early times. At later times, the t^2 term under the square root dominates over the linear term leading to an expansion of the wave packet.

We can verify that the changes to the width are true inhomogeneous effects by observing the scaling of their magnitude with the pulse size

$$\frac{\Delta R(t) - \Delta R}{\Delta R} = \frac{\alpha \hbar t}{2M} \frac{1}{\Delta R^2} + \mathcal{O}\left(\frac{1}{\Delta R^4} \right) . \tag{8.9}$$

The effect increases as the pulse width decreases.

To verify this effect in the many-body dynamics, we solve the full inhomogeneous SBEs for a GaAs quantum well that is excited resonantly with an ultrafast, 300 fs long pulse and an initial width of $\Delta R = 610$ nm in a low density limit. A radial phase $\phi(R) = \mathrm{i}\alpha(1 - \mathrm{e}^{-R^2/\Delta R^2}) = \mathrm{i}\alpha R^2/\Delta R^2 + \mathcal{O}(R^4)$ is added to the pump pulse to optically excite

a polarization wave packet similar to (8.7). Figure 8.1 shows the relative change of the width of the macroscopic polarization density as a function of time t for different values of α. In agreement with the analytic prediction, $\alpha > 0$ leads to an immediate increase of the excitation-spot size, while the change is reversed for $\alpha < 0$. For the parameters chosen, $\alpha = 0$ does not induce any noticeable changes to the width. The ballistic expansion predicted in Eq. (8.6) is negligible within the time window of the computation.

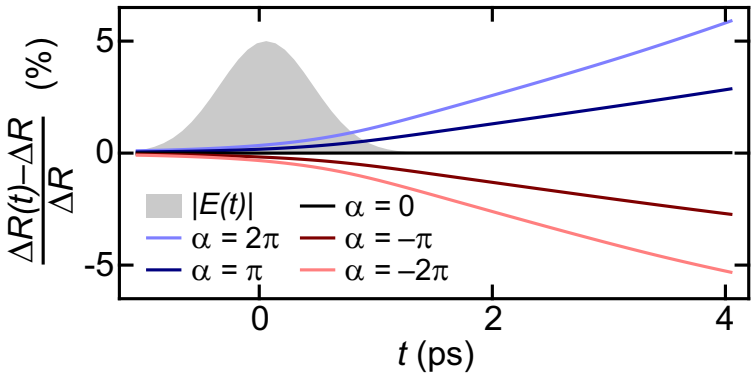

Figure 8.1: Effect of a radial phase on the dynamics of the polarization density. Computed relative change of the excitation spot size (polarization density) $\Delta R(t)$ as function of time t after excitation with a weak resonant pulse with envelope $E(t)$ and a radial phase parametrized by α.

8.4 Carrier dynamics

Numerical analysis of the inhomogeneous SBEs reveals that the spatio-temporal dynamics of the carrier occupations is dominated by the first term of (7.12b) which in its isolated form

$$\hbar\frac{\partial}{\partial t}f_{\mathbf{k}}(\mathbf{R}) = -\frac{\hbar^2}{m}\mathbf{k}\cdot\nabla_{\mathbf{R}}f_{\mathbf{k}}(\mathbf{R})\ , \tag{8.10}$$

describes the dynamics of a classical phase-space distribution of free particles with position $\mathbf{r}$, momentum $\hbar\mathbf{k}$, and mass m. Equation (8.10) is solved analytically by

$$f_{\mathbf{k}}(\mathbf{R};t) = \mathrm{e}^{-\frac{\hbar\mathbf{k}}{m}\cdot\nabla_{\mathbf{R}}t}f_{\mathbf{k}}(\mathbf{R};0) = f_{\mathbf{k}}(\mathbf{R}-\frac{\hbar\mathbf{k}}{m}t;0)\ . \tag{8.11}$$

Assuming an initial state with Gaussian spatial distribution of width ΔR and Gaussian momentum distribution of width Δk, the spatial width as a function of time is

$$f_{\mathbf{k}}(\mathbf{R};0) \propto \mathrm{e}^{-\frac{\mathbf{R}^2}{2\Delta R^2}-\frac{\mathbf{k}^2}{2\Delta k^2}} , \tag{8.12}$$

$$\Rightarrow \Delta R(t) = \Delta R\sqrt{1+\left(\frac{\hbar \Delta k}{m \Delta R}t\right)^2} . \tag{8.13}$$

This ballistic expansion of free carriers has the same time dependence as the macroscopic polarization in Eq. (8.6). However, the rate of expansion is determined by both the initial spatial width ΔR and the width in momentum Δk.

Figure 8.2 shows the evolution of the width of electron and hole densities after excitation with an ultrafast, 300 fs long resonant pulse with Gaussian profile and width $\Delta R = 610$ nm as computed from the singlet dynamics (inhomogeneous SBEs excluding the doublet dynamics). For resonant excitations of a quantum well, the excited momentum distribution $f_{\mathbf{k}}^{\mathrm{e/h}}(\mathbf{R})$ for both electrons and holes approximately follows the absolute-value squared of the $1s$-exciton wave function. Because the effective electron and hole masses in GaAs are

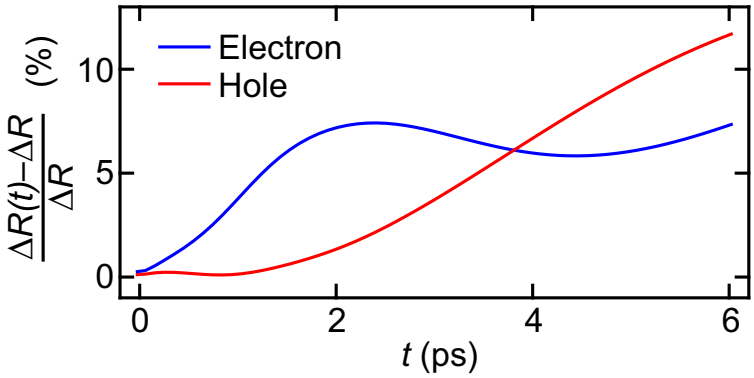

Figure 8.2: Plasma oscillations of the electron and hole distributions. Computed relative change of the excitation spot size (carrier density) $\Delta R(t)$ as function of time t for electrons (blue) and holes (red) after excitation with a resonant pulse. The calculation does not include polarization-to-population conversion which results in effectively free carriers after the microscopic polarization is decayed (0.5 ps lifetime).

drastically different from each other ($m_{\mathrm{e}} = 0.0665\, m_0$ and $m_{\mathrm{h}} = 0.235\, m_0$), the distribution of lighter electrons expands much faster than that of the heavier holes (Fig 8.2, $t < 1$ fs).

However, because electrons and holes are charged particles, the fast-advancing electrons create a ring with net negative charge, leaving behind a net positive charge of slower moving holes. For sufficiently large densities, the resulting Hartree forces induced by the attractive Coulomb interaction between electrons and holes (which are included in the inhomogeneous SBEs (F.2)) slow down the electron motion while holes are being accelerated (Fig 8.2, 1 fs $<$ t $<$ 3 fs). This leads to radial plasma oscillations of the excited electron–hole distribution in 2D. However, this behavior is only expected for a free electron–hole plasma as created by the pure singlet equations.

Correlations, described by the microscopic polarization $P_{\mathbf{k}}(\mathbf{R})$ and the exciton doublet $c_X^{\mathbf{k},\mathbf{k}',\mathbf{Q}}(\mathbf{R})$, act as a glue that binds electrons and holes together and prevents them from moving independent of each other. In fact, in the coherent limit [41] where the microscopic polarization $P_{\mathbf{k}}(\mathbf{R})$ does not dephase, densities strictly follow $f_{\mathbf{k}}^{\mathrm{e}}(\mathbf{R}) = f_{\mathbf{k}}^{\mathrm{h}}(\mathbf{R}) = |P_{\mathbf{k}}(\mathbf{R})|^2$. At resonant excitation of the system, a laser first excites electron–hole pairs that are bound to coherent excitons described by the microscopic polarization $P_{\mathbf{k}}(\mathbf{R})$. Scattering eventually leads to a dephasing of $P_{\mathbf{k}}(\mathbf{R})$, however, instead of loosing the correlations, they are converted into incoherent correlations described by the exciton doublet to form incoherent excitons. This process is known as polarization-to-population (P2P) conversion [70, 170].

To show the importance of the P2P conversion in our computations, Fig. 8.3 shows snapshots of the computed electron density at different times after the excitation. For the full computation including $c_X^{\mathbf{k},\mathbf{k}',\mathbf{Q}}(\mathbf{R})$ (Fig. 8.3, left), the excited electron spot remains almost unchanged, even at times beyond the $P_{\mathbf{k}}(\mathbf{R})$ life time of about 0.5 ps. By artificially switching off the P2P conversion in the computations and making $P_{\mathbf{k}}(\mathbf{R})$ dephase without generating $c_X^{\mathbf{k},\mathbf{k}',\mathbf{Q}}(\mathbf{R})$, the carriers are forced into a plasma state (Fig. 8.3, right) which exhibits a rapid ballistic expansion, consistent with the plasma behavior shown in Fig. 8.2. When homogeneous conditions are assumed, differences in the velocities of electrons and holes do not manifest themselves in local charging. As a result, P2P conversion can sometimes be neglected and QDCE efficiently limited to the singlet level, which reduces numerical

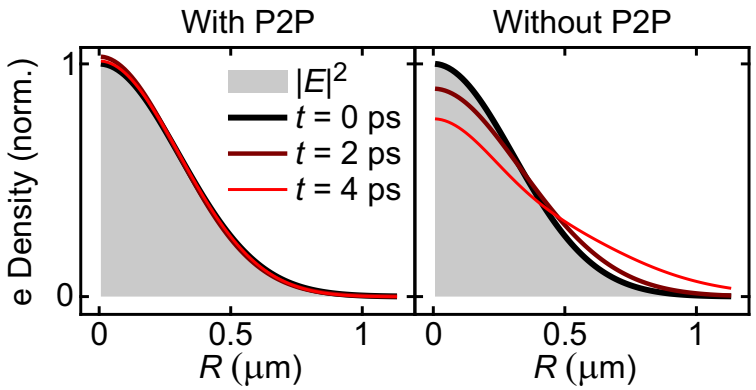

Figure 8.3: Effect of incoherent correlations on the electron dynamics. Computed electron density $n^{\mathrm{e}}(\mathbf{R})$ (lines) at times $t = 0$ fs, 2 fs, and 4 fs after resonant excitation compared to the spatial profile of the excitation spot (shaded area). Left, full computation; right, computation without P2P conversion and creation of incoherent doublet correlations.

complexity. However, when spatial variations are concerned, the inclusion of doublets become necessary to keep the electron and hole distributions in check, as evidenced by Fig. 8.3.

8.5 Theory–experiment comparison

To benchmark the inhomogeneous SBEs under real conditions, we compare our computations to experiments performed in the group of Steven Cundiff (University of Michigan). Specifically, the ultrafast spatial dynamics of an excitation spot was measured by employing a pump–probe scheme with two ultrashort, diffraction limited laser pulses, resonantly pumping and probing the 1s exciton in a system of GaAs quantum wells. By scanning the time delay and position of the probe pulse relative to the fixed delay and position of the pump pulse, the width of the excitation spot as a function of time was measured. For more details about the experiment we refer the reader to Ref. [171]. A subset of the experimental measurements is presented in Fig. 8.4 (gray squares with error bars) which shows the relative change of the excitation-spot width as a function of time using diffraction-limited spots with a width of 600 nm (top) and 12 μm (bottom). The smaller excitation spot (Fig. 8.4, top) shows a transient reduction in size by up to 2% before increasing via a diffusive expansion. The same measurement with identical pump intensities but larger spot size (Fig. 8.4, bot-

tom) does not show this effect. The dependence on the spot size suggests that the observed transient reduction of the width is directly induced by the spatial inhomogeneities of the excitation.

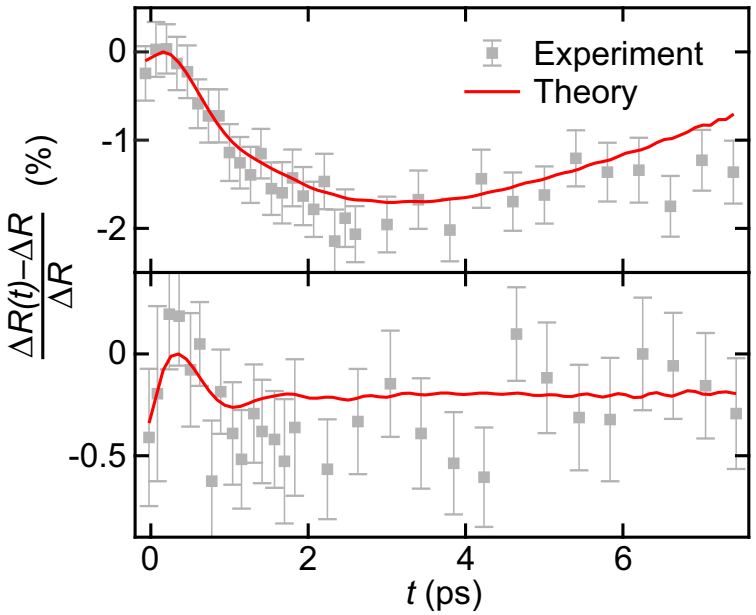

Figure 8.4: Theory–experiment comparison of excitation-spot dynamics for resonant excitation. Computed (red line) and measured (gray squares with error bars) change of the excitation-spot width $\Delta R(t)$ after excitation with a resonant pump focused to a spot size of 600 nm (top) and 12 μm (bottom).

The red lines in Figure 8.4 show inhomogeneous SBE computations including the P2P conversion to exciton doublets under conditions similar to the experiment. The computations reproduce the experimental results closely by postulating a radial phase of $\alpha = -3\pi$ in the excited polarization. As discussed in Section 8.3, this produces a shrinking of the excitation spot. Once all polarization is converted into incoherent excitons by P2P conversion, the shrinking ends and expansion takes over.

The experimental data has been recorded for later times than shown in Fig. 8.4 and exhibits a diffusive expansion where the spot-size changes follow a $\sqrt{t}$ dependence. Diffusive expansion of incoherent excitons is created by relaxation of the exciton distribution towards a local thermal equilibrium. The required exciton–phonon interaction to describe such processes microscopically are currently not included in our doublet equations. As a result, our

model produces a ballistic expansion ($\propto t$) and is therefore only valid at early times before the exciton distribution thermalizes.

8.6 Conclusion

We have investigated the effects of spatially inhomogeneous excitations of semiconductors by analytic and numerical studies of the inhomogeneous SBEs and a theory–experiment comparison. At the beginning of this Chapter, we derived the inhomogeneous SBEs using the QDCE approach and a Wigner-function representation for singlets and doublets that intuitively separates the relevant length scales of macroscopic spatial variations and microscopic many-body correlations.

We found that the spatial dynamics of the microscopic polarization follows that of a quantum-mechanical wave packet and demonstrated that spatial chirp controls its motion. This connection could open interesting avenues for solid-state based quantum-information processing. Chapter 6 discussed how quantum information could be encoded in the valley degree of freedom of 2D TMDs and manipulated by lightwaves. Combining this approach with local excitations could make it possible to create multiple valleytronic qubits and move them in space by inducing appropriate spatial chirp. This way, qubits could even be brought onto crossing paths to allow them to interfere and interact with each other, creating entangled states.

While conceptually intriguing, such ideas will face extreme challenges in experimental realizations. However, comprehensive theories such as the ones developed in this Thesis can help test such concepts and determine their feasibility. Section 8.4 already determined that meaningful investigations need to include clusters up to at least the doublet level. Combining the theory used in this Chapter with that developed in Chapter 3 for lightwave electronics would be an important step to explore the potential of lightwave quantum-information processing using multiple excitation-spot qubits.

Chapter 9

Spatial Dynamics of Incoherent Excitons

This Chapter is in parts adapted from Z. Li, M. Florian, K. Datta, Z. Jiang, M. Borsch, Q. Wen, M. Kira, and P. B.Deotare, "Enhanced exciton-drift transport through suppressed diffusion in one-dimensional guides", ACS Nano (in print, 2023).

9.1 Introduction

In conventional electronics, the electric charge of electrons and holes in semiconductors is employed to switch carrier transport by applying an electric bias. Besides scattering of charge carriers, with the lattice which manifests as resistance and produces heat, the charge of electrons and holes also creates parasitic capacitances that reduce efficiency and practically limit the speed of electronics. Excitons pose an alternative for future IT applications. As charge-neutral carriers, they are not subject to parasitic capacitances while still maintaining efficient transport properties [172–174]. The exciton mobility characterizes how fast excitons move when subjected to an accelerating force and is an important material property to judge the viability of exciton-based IT applications.

We first derive the macroscopic dynamics of incoherent exciton densities from the microscopic equations developed in Chapter 7 to describe exciton transport in nanostructure

potentials. We then discuss how the exciton mobility can be measured from exciton diffusion or strain-induced exciton drift. Finally, we discuss the application and limitations of these two approaches to measured the exciton mobility in WSe_2.

9.2 Drift–diffusion kinetics of incoherent excitons

In this Section we apply the microscopic theory developed in Chapter 7 to understand the macroscopic dynamics of incoherent excitons excited in two-dimensional TMDs on nanosecond time scales where excitonic drift and diffusion take place. Specifically, we discuss how the dynamics of excitons is influenced by strain to enable precise guiding of exciton motion in strain-engineered nanostructures.

In QDCE, incoherent excitons are represented by the exciton doublet $c_X^{\mathbf{k},\mathbf{k}',\mathbf{Q}}(\mathbf{R})$, as introduced in Section 7.3. At the nanosecond time scales, all coherences have vanished and the dynamics follows

$$\begin{aligned} \mathrm{i}\hbar\frac{\partial}{\partial t}c_X^{\mathbf{k},\mathbf{k}',\mathbf{Q}}(\mathbf{R}) = (E_{\mathbf{k}'}-E_{\mathbf{k}})c_X^{\mathbf{k},\mathbf{k}',\mathbf{Q}}(\mathbf{R}) + \sum_{\mathbf{q}}\Big[V_{\mathbf{k}-\mathbf{q}}c_X^{\mathbf{q},\mathbf{k}',\mathbf{Q}}(\mathbf{R}) - V_{\mathbf{k}'-\mathbf{q}}c_X^{\mathbf{k},\mathbf{q},\mathbf{Q}}(\mathbf{R})\Big] + \mathrm{i}\Gamma^{\mathbf{k},\mathbf{k}',\mathbf{Q}}(\mathbf{R}) \\ - \mathrm{i}\frac{\hbar^2}{M}\mathbf{Q}\cdot\nabla_{\mathbf{R}}c_X^{\mathbf{k},\mathbf{k}',\mathbf{Q}}(\mathbf{R}) + \mathrm{i}\nabla_{\mathbf{R}}U(\mathbf{R})\cdot\nabla_{\mathbf{Q}}c_X^{\mathbf{k},\mathbf{k}',\mathbf{Q}}(\mathbf{R}) + \mathcal{O}\Big(\big[f^{\mathrm{e/h}}\big]^2\Big)\,, \end{aligned} \tag{9.1}$$

where we assume that excitons were formed well below the excitonic Mott transition under dilute conditions ($f_{\mathbf{k}}^{\mathrm{e/h}}(\mathbf{R}) \ll 1$) and $U(\mathbf{R})$ is an external potential that excitons move in. The exciton doublet $c_X^{\mathbf{k},\mathbf{k}',\mathbf{Q}}(\mathbf{R})$ contains all possible electron–hole correlations, including the exciton populations we are interested in and correlations between electrons and holes that do not form bound electron–hole pairs, correlated electron–hole plasma states [41, 175]. To distinguish between the different forms of electron correlations we transform $c_X^{\mathbf{k},\mathbf{k}',\mathbf{Q}}(\mathbf{R})$ into the exciton basis [70]

$$N_{\mathbf{Q}}^{\alpha,\beta}(\mathbf{R}) \equiv \sum_{\mathbf{k},\mathbf{k}'}\phi_\alpha(\mathbf{k})\phi_\beta^*(\mathbf{k}')c_X^{\mathbf{k},\mathbf{k}',\mathbf{Q}}(\mathbf{R})\,, \tag{9.2}$$

where $\phi_\alpha(\mathbf{k})$ is an exciton wave function with quantum number α. The diagonal elements $N_{\mathbf{Q}}^{\alpha,\alpha}(\mathbf{R})$ (scaling proportional to $f_{\mathbf{k}}^{\mathrm{e/h}}(\mathbf{R})$) describe the distribution of α-excitons with center-of-mass momentum $\hbar\mathbf{Q}$ at position $\mathbf{R}$. The off-diagonal elements $N_{\mathbf{Q}}^{\alpha,\beta\neq\alpha}(\mathbf{R})$ describe coherent transitions between states α and β as well as correlated electron–hole plasma which scales with the product $f_{\mathbf{k}}^{\mathrm{e}}(\mathbf{R})f_{\mathbf{k}}^{\mathrm{h}}(\mathbf{R})$. Under dilute conditions ($f_{\mathbf{k}}^{\mathrm{e/h}}(\mathbf{R}) \ll 1$), $c_X^{\mathbf{k},\mathbf{k}',\mathbf{Q}}(\mathbf{R})$ is dominated by exciton populations which quickly relax into $1s$-exciton states. Applying the transformation of Eq. (9.2), the exciton dynamics (9.1) in the dilute limit yields

$$\hat{D}N_{\mathbf{Q}}(\mathbf{R}) = \Gamma_{\mathbf{Q}}(\mathbf{R}), \quad \text{with} \quad \hat{D} \equiv \frac{\partial}{\partial t} + \frac{\hbar}{M}\mathbf{Q}\cdot\nabla_{\mathbf{R}} - \frac{1}{\hbar}[\nabla_{\mathbf{R}}U(\mathbf{R})]\cdot\nabla_{\mathbf{Q}}\,, \tag{9.3}$$

for the $1s$-exciton population $N_{\mathbf{Q}}(\mathbf{R}) \equiv N_{\mathbf{Q}}^{1s,1s}(\mathbf{R})$, where $\Gamma_{\mathbf{Q}}(\mathbf{R})$ is the projection of $\Gamma_{\mathbf{k},\mathbf{k}',\mathbf{Q}}(\mathbf{R})$ onto the $1s$ state.

For the scattering $\Gamma_{\mathbf{Q}}(\mathbf{R})$, we introduce a phenomenological relaxation model which drives the system towards a local thermal equilibrium (LTE) defined by a Boltzmann distribution

$$\Gamma_{\mathbf{Q}}^{\mathrm{rlx}}(\mathbf{R}) = -\frac{1}{\tau}\big[N_{\mathbf{Q}}(\mathbf{R}) - N_{\mathbf{Q}}^{\mathrm{LTE}}(\mathbf{R})\big], \quad N_{\mathbf{Q}}^{\mathrm{LTE}}(\mathbf{R}) \equiv \frac{\hbar^2 N(\mathbf{R})}{2Mk_BT(\mathbf{R})}\mathrm{e}^{-\hbar^2\mathbf{Q}^2/[2Mk_BT(\mathbf{R})]}\,, \tag{9.4}$$

with relaxation rate τ, the macroscopic exciton density $N(\mathbf{R}) = \frac{1}{\mathcal{S}}\sum_{\mathbf{Q}} N_{\mathbf{Q}}(\mathbf{R})$ with normalization area $\mathcal{S}$, and a position dependent temperature $T(\mathbf{R})$. The relaxation model can be applied because the microscopic relaxation processes occur on sub-picosecond time scales, much faster than the nanosecond time scales concerned here [176].

By integrating Eq. (9.3) over all momenta $\mathbf{Q}$, the macroscopic dynamics can be computed from

$$\frac{\partial}{\partial t}N(\mathbf{R}) = -\nabla_{\mathbf{R}}\cdot\mathbf{j}(\mathbf{R}) + \frac{1}{\hbar}\nabla_{\mathbf{R}}U(\mathbf{R})\cdot\mathbf{I}(\mathbf{R}) + \Gamma(\mathbf{R})\,, \tag{9.5}$$

where we defined

$$\mathbf{j}(\mathbf{R}) \equiv \int \mathrm{d}^2Q \, \frac{\hbar\mathbf{Q}}{M} N_{\mathbf{Q}}(\mathbf{R}) \, , \tag{9.6a}$$

$$\mathbf{I}(\mathbf{R}) \equiv \int \mathrm{d}^2Q \, \nabla_{\mathbf{Q}} N_{\mathbf{Q}}(\mathbf{R}) \, , \tag{9.6b}$$

$$\Gamma(\mathbf{R}) \equiv \int \mathrm{d}^2Q \, \Gamma_{\mathbf{Q}}(\mathbf{R}) \, . \tag{9.6c}$$

The integral $\mathbf{I}(\mathbf{R})$ vanishes after applying Gauss' integral theorem. Also, $\Gamma(\mathbf{R})$ vanishes because the relaxation model conserves the particle number by definition. The macroscopic current density $\mathbf{j}(\mathbf{R})$ is the only non-vanishing term and can be solved by defining the deviation of the actual distribution from the LTE state $\delta N_{\mathbf{Q}}(\mathbf{R}) \equiv N_{\mathbf{Q}}(\mathbf{R}) - N_{\mathbf{Q}}^{\mathrm{LTE}}(\mathbf{R})$ which converts Eq. (9.5) to

$$\delta N_{\mathbf{Q}}(\mathbf{R}) = -\tau \Gamma_{\mathbf{Q}}(\mathbf{R}) = -\tau \hat{D} N_{\mathbf{Q}}(\mathbf{R}) = -\tau \hat{D} \big[N_{\mathbf{Q}}^{\mathrm{LTE}}(\mathbf{R}) + \delta N_{\mathbf{Q}}(\mathbf{R}) \big] \, , \tag{9.7}$$

with the help of the relaxation model (9.4). The implicit equation (9.7) can be solved iteratively by inserting the equation back into its right-hand side, resulting in the explicit series

$$\delta N_{\mathbf{Q}}(\mathbf{R}) = \sum_{n=1}^{\infty} (-\tau)^n \hat{D}^n N_{\mathbf{Q}}^{\mathrm{LTE}}(\mathbf{R}) \, . \tag{9.8}$$

This equation describes how spatial variations in the exciton density and temperature lead to deviations of $N_{\mathbf{Q}}(\mathbf{R})$ compared to the LTE distribution. In the limit where the relaxation time τ is much faster than the time scale of spatial changes, it is sufficient to only include the lowest order in τ. Using $\delta N_{\mathbf{Q}}(\mathbf{R}) = -\tau \hat{D} N_{\mathbf{Q}}^{\mathrm{LTE}}(\mathbf{R})$ and $\delta N_{\mathbf{Q}}(\mathbf{R}) = N_{\mathbf{Q}}(\mathbf{R}) - N_{\mathbf{Q}}^{\mathrm{LTE}}(\mathbf{R})$, the integral defining the current density (9.6a) has the analytic solution

$$\mathbf{j}(\mathbf{R}) = -\frac{\tau}{M} k_B T \nabla_{\mathbf{R}} N(\mathbf{R}) - N(\mathbf{R}) \Big[\frac{\tau}{M} k_B (\nabla_{\mathbf{R}} T(\mathbf{R})) + \frac{\tau}{M} \nabla_{\mathbf{R}} U(\mathbf{R}) \Big] \, . \tag{9.9}$$

This renders Eq. (9.5) into the well-known convection–diffusion equation

$$\frac{\partial}{\partial t}N(\mathbf{R}) = \nabla_{\mathbf{R}} \cdot [D(\mathbf{R})\nabla_{\mathbf{R}}N(\mathbf{R})] - \nabla_{\mathbf{R}} \cdot [N(\mathbf{R})(\mathbf{v}_S(\mathbf{R}) + \mathbf{v}_D(\mathbf{R}))] \; , \tag{9.10}$$

where we identified the diffusivity

$$D(\mathbf{R}) \equiv \mu k_B T(\mathbf{R}) \; , \tag{9.11}$$

the exciton mobility $\mu \equiv \tau/M$, the drift velocity

$$\mathbf{v}_D(\mathbf{R}) \equiv -\mu \nabla_{\mathbf{R}} U(\mathbf{R}) \; , \tag{9.12}$$

created by gradients of the exciton potential $U(\mathbf{R})$, and the Seebeck velocity

$$\mathbf{v}_S(\mathbf{R}) \equiv \mu k_B \nabla_{\mathbf{R}} T(\mathbf{R}) \; , \tag{9.13}$$

following the temperature gradients.

9.3 Exciton mobility

The mobility defines how easily particles in solids can be moved when a force is applied. More specifically, a particle with mobility μ that is accelerated by a force F responds by moving with a constant drift velocity

$$v_D = \mu F \; . \tag{9.14}$$

In the case of charged particles like electrons and holes, the mobility is easily measured by applying an electric bias and measuring the resulting current. This does not work for neutral particles like excitons. However, there are two alternative approaches. First, the Einstein

relation

$$D = \mu k_B T \,, \tag{9.15}$$

which appears in the drift–diffusion equation (9.11), directly relates the mobility to diffusion. By measuring the exciton diffusion at a known temperature, the mobility follows from the ratio of diffusivity and temperature. Second, strain induces changes to the band structure which are reflected in the exciton wave functions and energies. Local strain creates a spatial exciton potential $U(\mathbf{R})$ that exerts an accelerating force on the excitons via Eq. (9.12). With proper strain engineering, excitons can be accelerated by a constant force, creating excitonic drift. By relating the drift velocity for a known force, definition (9.14) can directly be applied to extract the exciton mobility.

9.4 Measuring exciton mobility in tungsten diselenide

We compare the exciton convection–diffusion equation derived in Section 9.2 to measurements performed in the group of Parag Deotare (University of Michigan) who devised an experimental setup to observe the spatio-temporal dynamics of an exciton density and measure excitonic drift and diffusion. They furthermore designed strain-based exciton guides in two-dimension WSe_2 which create exciton potentials. For a detailed discussion of the experimental setup as well as the device design and fabrication, we refer the reader to Refs. [177, 178].

The exciton potential $U(\mathbf{R})$ can directly be inferred from spatially-resolved photoluminescence (PL) measurements of the exciton energy. Figure 9.1 shows a one-dimensional scan of the spectral PL shift (black dots) across an exciton guide as function of the position. Over a length of 4 μm (shaded area), the PL energy decreases almost linearly. As a result, excitons are accelerated by a force of approximately $F = 2.8$ meV/μm in this region.

Figure 9.2a shows the time dynamics of an exciton distribution excited at time $t = 0$ by

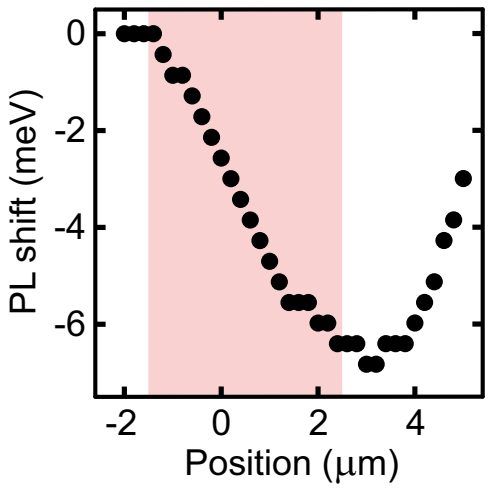

Figure 9.1: Strain-induced shift of the exciton energy. Dots mark the spatially resolved photoluminescence (PL) measurement along a nanostructure which tracks changes to the exciton energy. The shaded area indicates a region of approximately linear slope.

a narrow excitation spot centered at $x = 0$. The centroid motion (blue line) shows a clear drift towards positive values, following the strain-induced exciton potential (Fig. 9.1) from which a drift velocity can be extracted. At the same time, the distribution spreads (black lines marking the width of the distribution) due to exciton diffusion. By fitting the variance of the distribution $\sigma(t)$ to a linear model $\sigma^2(t) - \sigma^2(0) = 2Dt$, as expected for diffusion, the diffusivity is obtained.

Similar measurements and analyses were performed on five different samples with varying amounts of strain resulting in different forces F exerted on the exciton distribution. Figure 9.3 shows the measured drift velocity (black squares on left axis) and diffusivity (red points on right axis) as function of the force F for the five samples. The drift velocity shows a linear dependence with the force, consistent with Eq. (9.14). From its slope, the exciton mobility is estimated to be $\mu = 169 \pm 39$ cm^2/(eV s). The diffusivity is almost constant and independent of F. However, its value is about 20 times smaller than the value predicted by the Einstein relation of Eq. (9.15) based on the measured mobility at room temperature (red dashed line). To visualize this discrepancy, we numerically solve the convection–diffusion equation (9.10) for conditions similar to the measurement shown in Fig. 9.2a. We implement

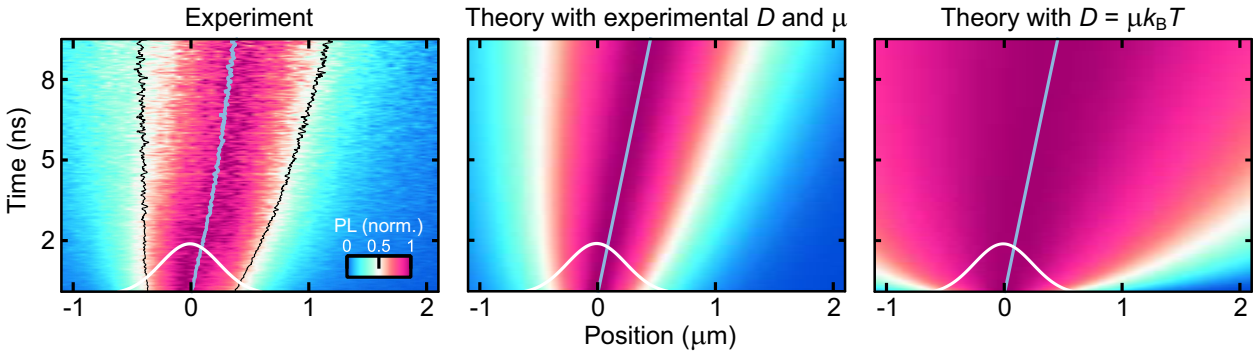

Figure 9.2: Spatio-temporal map of the exciton dynamics along a nanostructure potential. Left, measured photoluminescence (PL) as function of the position along the nanostructure and time after excitation with a diffraction-limited spot (white line). From the centroid (blue line) and width (black lines) of the distribution, the diffusivity D and mobility μ can be estimated. Middle, Numerical solution of the convection–diffusion equation using the estimated D and μ from measurement (left frame). Right, Numerical solution of the convection–diffusion equations using the μ estimated from measurement and D following from the Einstein relation. The data is normalized at each time point.

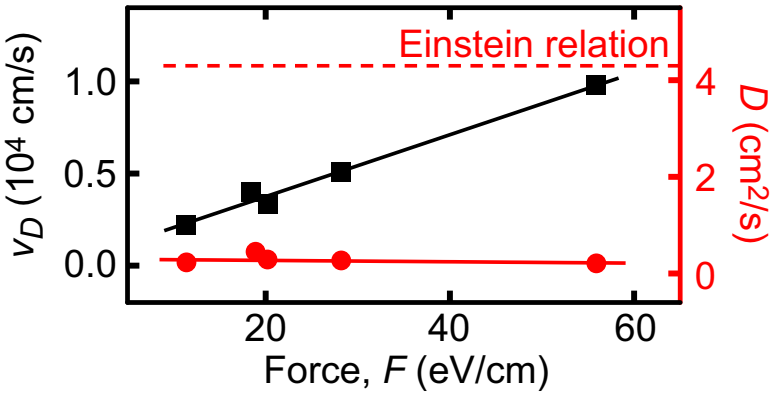

Figure 9.3: Drift velocity v_{D} (black squares) and diffusivity D (red dots) estimated from measurements for five samples with varying strain-induced forces F. The mobility μ can be estimated from a linear fit of the drift velocity (black line). The observed average diffusivity among all samples (solid red line) is much smaller than the diffusivity predicted by the Einstein relation (dashed red line) based on the estimated μ.

an excitonic potential $U(\mathbf{R})$ consistent with the experimental PL measurement, use the measured μ, and explicitly set D to match the experiment. The exciton dynamics computed from an initial ($t = 0$) Gaussian distribution (Fig. 9.2b) visually matches the experiment (Fig. 9.2a). However, if the diffusivity is chosen to be consistent with the Einstein relation (Fig. 9.2c), the dynamics is dominated by a rapid diffusion not observed in the experiment.

This suggests that the Einstein relation is violated in WSe_2.

The violation of the Einstein relation can be explained by the presence of defect states which TMDs are known to have in abundance [179, 180], including saturable trap states that capture excitons [181]. The exciton density is highest at the center of the distribution where it can saturate defect states. In the tails of the distribution, defect states remain unoccupied because the exciton density is low. Diffusion spreads the density into the tail regions where excitons are easily trapped into immobile states, effectively slowing down the expansion. In contrast, the centroid motion is dominated by the center of the distribution where exciton density is high and defects saturated, leaving the drift motion mostly unaffected. This way, saturable defect states can lead to a decrease of the apparent diffusivity, explaining the violation of the Einstein relation.

To quantitatively analyze the effect of defects on the exciton dynamics, the convection–diffusion equation (9.10) was extended phenomenologically to include a capture model with immobile saturable defect states. This model reproduces the violation of Einstein relation observed in the experiment. For a comprehensive description and analysis of the model as well as a detailed examination of the shape of the distribution with theory–experiment comparisons we refer the reader to Ref. [178]. The reference also discusses a further extension of the model to include Auger processes that locally heat the exciton gas to explain experiments at higher excitation densities where additional drift contributions from the Seebeck effect (Eq. (9.13)) become important.

9.5 Conclusion

We derived equations of motion to describe the macroscopic dynamics of incoherent excitons in nanostructures which resulted in the convection–diffusion equation and discussed how the exciton mobility can be extracted from measurements of excitonic drift and diffusion. A comparison to experiments revealed that the Einstein relation in WSe_2 is violated and that

saturable defect states significantly slow down exciton diffusion, rendering estimates of the exciton mobility based on diffusion measurements incorrect.

The violation of the Einstein relation was explained by introducing phenomenological scattering models that extend the convection–diffusion equation. In the future, defect states and the related scattering processes could be described microscopically. A more detailed understanding of the microscopic processes could motivate new concepts and strategies to minimize or possibly circumvent scattering and increase the efficiency of exciton transport.

Chapter 10

Conclusion

In this Thesis, I have developed a comprehensive many-body quantum theory that combines the quantum-dynamic cluster expansion theory to efficiently describe emerging many-body correlations with *ab inito* input from density-functional theory to quantitatively describe many-body excitations in quantum materials. The developed theory was applied to analytically and numerically study lightwave-electronic processes and spatially inhomogeneous excitations in semiconductors alongside extensive theory–experiment comparisons. Below, each of our main results is briefly summarized with an outlook for future directions and contextualized with regards to the development of future lightwave-electronics based technologies.

We developed a new lightwave-based tomographic approach to reconstruct the band structure of quantum materials from a set harmonic sideband spectra by utilizing emergent crystal-momentum combs to connect the sideband intensity to the band structure. The approach was demonstrated in monolayer WSe_2 and can be used complementary to traditional ARPES measurements to probe quantum materials with high spatial resolution under operational conditions and in ambient. In the future, this approach could be further refined to use unidirectional and time-resolved lightwave excitations to obtain even more detailed band-structure information. Additionally, an extension to reconstruct other material properties such as the dipole, phonon, and Coulomb matrix elements is conceivable.

We also used two-dimensional harmonic-sideband spectrograms, extending the concept of quasiparticle colliders, to directly clock correlations of quasiparticle states in the time domain. This attoclocking approach was demonstrated by resolving differences in the correlation strengths of excitons in samples of monolayer and bulk WSe_2. We furthermore showed that the correlation strength can be tuned and changes be detected in attoclocking delays. Based on this observation, we predicted that the excitonic Mott transition can be observed this way. In the future, our attoclocking approach could be expanded to detect further quantum-phase transitions and probe correlations of higher-order quasiparticles such as trions, biexcitons, or dropletons. In the context of lightwave electronic applications, the attoclocking approach could be used to probe correlated states with spatial and temporal resolution during a device's operation. Together with lightwave tomography, it forms the basis of a new ecosystem of lightwave-based tools to characterize and probe materials for, and the functionality of, future solid-state technologies and creates a bridge between theoretical modelling and experiments.

We theoretically investigated the feasibility and efficiency of lightwave valleytronics. Specifically, we optimized lightwave excitations to switch the valley degree of coherent excitons in two-dimensional quantum materials, discussed how a valleytronic switching can be characterized from its light emission, and described how emergent frequency combs could be used to experimentally verify the temporal sequencing of multiple valleytronic switches. Coherent switching of the valley-degree of freedom provides an intriguing platform for lightwave-driven information processing and PHz electronics. Future work could include a search of valleytronic materials to find the best candidates for experimental tests to our predictions. At the same time, further theoretical work is needed to formulate new excitation schemes to realize classical or even quantum gates for information processing.

Finally, we introduced a Wigner-function representation of clusters to describe the spatial degree of freedom in a fully microscopic theory. We found that coherent excitons behave like quantum-mechanical particles with respect to their spatial dynamics while charge carri-

ers and incoherent excitons behave more like classical particles. We furthermore found that defects in semiconductors can lead to non-trivial contributions to the spatial dynamics. Non-thermal distribution as well as scattering processes can affect the macroscopic dynamics of drift and diffusion of excitons. Further work is needed to understand the effects of scattering and defects states to their fullest extend. However, the insights into the spatial dynamics of local excitations that were gained could already be used to control and manipulate excitation spots in future applications. For example, multiple local excitations in a valleytronic material could be an interesting platform to explore. While the valley-degree of freedom can be manipulated with lightwave excitations, manipulation of the spatial degree of freedom could enable gate operations between multiple local excitations. To this end, a full description of the lightwave dynamics with spatial degrees of freedom would be desirable.

Appendices

Appendix A

Multi-Band SBEs

The multi-band SBEs are given by

$$\mathrm{i}\hbar\frac{\partial}{\partial t}P_{\mathbf{k}}^{\lambda,\nu} = \left[E_{\nu,\mathbf{k}}^{\mathrm{ren}} - E_{\lambda,\mathbf{k}}^{\mathrm{ren}}\right]P_{\mathbf{k}}^{\lambda,\nu} + \mathrm{i}|e|\mathbf{E}(t)\cdot\left[\nabla_{\mathbf{k}} - \mathrm{i}\left(\boldsymbol{\mathcal{A}}_{\mathbf{k}}^{\nu} - \boldsymbol{\mathcal{A}}_{\mathbf{k}}^{\lambda}\right)\right]P_{\mathbf{k}}^{\lambda,\nu} \tag{A.1}$$

$$- \sum_{\alpha\neq\nu} P_{\mathbf{k}}^{\lambda,\alpha}\Omega_{\mathbf{k}}^{\alpha,\nu}(t) + \sum_{\alpha\neq\lambda} P_{\mathbf{k}}^{\alpha,\nu}\Omega_{\mathbf{k}}^{\lambda,\alpha}(t) + \Gamma_{\mathbf{k}}^{\lambda,\nu}\ , \tag{A.2}$$

with the renormalized kinetic energy

$$E_{\lambda,\mathbf{k}}^{\mathrm{ren}} \equiv E_{\lambda,\mathbf{k}} - \sum_{\mathbf{k}'} V_{\mathbf{k},\mathbf{k}'}^{\lambda,\lambda} P_{\mathbf{k}'}^{\lambda,\lambda}\ , \tag{A.3}$$

the renormalized Rabi energy

$$\Omega_{\mathbf{k}}^{\lambda,\nu}(t) \equiv \mathbf{d}_{\mathbf{k}}^{\nu,\lambda}\cdot\mathbf{E}(t) + \sum_{\mathbf{k}'} V_{\mathbf{k},\mathbf{k}'}^{\nu,\lambda} P_{\mathbf{k}'}^{\lambda,\nu}\ . \tag{A.4}$$

All doublet terms are collected in $\Gamma_{\mathbf{k}}^{\lambda\nu}$. We assumed $V_{\mathbf{k},\mathbf{k}',\mathbf{q}}^{\lambda,\nu,\nu',\lambda'} = \delta_{\lambda,\lambda'}\delta_{\nu,\nu'}V_{\mathbf{k},\mathbf{k}',\mathbf{q}}^{\lambda,\nu,\nu,\lambda}$ and define $V_{\mathbf{k},\mathbf{k}'}^{\lambda,\nu} \equiv V_{\mathbf{k},\mathbf{k}',\mathbf{k}-\mathbf{k}'}^{\lambda,\nu,\nu,\lambda}$.

Appendix B

Macroscopic Current

The SBEs are coupled to Maxwell's equations via the macroscopic current density $\mathbf{J}$ which is connected to the macroscopic polarization density via

$$\mathbf{J} = -|e|\frac{\partial}{\partial t}\langle \mathbf{r} \rangle = \frac{\partial}{\partial t}\mathbf{P} \, . \tag{B.1}$$

The macroscopic polarization density can be identified from the Hamiltonian (3.4) and is given by

$$\mathbf{P} = \frac{1}{\mathcal{S}}\left\langle \hat{\mathbf{P}}_d + \hat{\mathbf{P}}_{\mathcal{A}} + \hat{\mathbf{P}}_{\nabla} \right\rangle \, , \tag{B.2}$$

with

$$\hat{\mathbf{P}}_d = \sum_{\lambda \neq \nu, \mathbf{k}} a^{\dagger}_{\lambda,\mathbf{k}} a_{\nu,\mathbf{k}} \, \mathbf{d}^{\lambda,\nu}_{\mathbf{k}} \, , \; \hat{\mathbf{P}}_{\mathcal{A}} = -|e| \sum_{\lambda,\mathbf{k}} a^{\dagger}_{\lambda,\mathbf{k}} a_{\lambda,\mathbf{k}} \, \boldsymbol{\mathcal{A}}^{\lambda}_{\mathbf{k}} \, , \; \hat{\mathbf{P}}_{\nabla} = -\mathrm{i}|e| \sum_{\lambda,\mathbf{k}} a^{\dagger}_{\lambda,\mathbf{k}} (\nabla_{\mathbf{k}} a_{\lambda,\mathbf{k}}) \, . \tag{B.3}$$

The expectation value $\langle \hat{\mathbf{P}} \rangle_d$ can be evaluated directly and yields the interband polarization density

$$\mathbf{P}^{\text{inter}} \equiv \frac{1}{\mathcal{S}}\left\langle \hat{\mathbf{P}}_d \right\rangle = \frac{1}{\mathcal{S}} \sum_{\lambda \neq \nu, \mathbf{k}} P^{\lambda,\nu}_{\mathbf{k}} \, \mathbf{d}^{\lambda,\nu}_{\mathbf{k}} \, . \tag{B.4}$$

The two remaining contributions can be computed in the current form by evaluating the Heisenberg equation of motion

$$\mathbf{J}^{\mathrm{rest}} = \frac{\partial}{\partial t}\frac{1}{\mathcal{S}}\left\langle \hat{\mathbf{P}}_{\mathcal{A}} + \hat{\mathbf{P}}_{\nabla} \right\rangle = -\frac{1}{\mathcal{S}}\frac{\mathrm{i}}{\hbar}\left\langle \left[\hat{\mathbf{P}}_{\mathcal{A}} + \hat{\mathbf{P}}_{\nabla}, \hat{H}\right]\right\rangle \ . \tag{B.5}$$

This yields the total macroscopic current density

$$\mathbf{J} = \frac{\partial}{\partial t}\mathbf{P}^{\mathrm{inter}} + \sum_{\lambda,\mathbf{k}} P^{\lambda,\lambda}_{\mathbf{k}}\, \widetilde{\mathbf{j}}^{\lambda}_{\mathbf{k}} - \sum_{\lambda,\mathbf{k}} P^{\lambda,\lambda}_{\mathbf{k}}\, \frac{|e|^2}{\hbar}\mathbf{E}(t) \times \mathbf{\Omega}^{\lambda}_{\mathbf{k}} \tag{B.6}$$

$$- \sum_{\lambda\neq\nu,\mathbf{k}} P^{\lambda,\nu}_{\mathbf{k}}\, |e|\left[\mathrm{i}(\boldsymbol{\mathcal{A}}^{\lambda}_{\mathbf{k}} - \boldsymbol{\mathcal{A}}^{\nu}_{\mathbf{k}}) - \nabla_{\mathbf{k}}\right]\Omega^{\lambda,\nu}_{\mathbf{k}} + \mathbf{J}[\Delta\langle 2\rangle] \ , \tag{B.7}$$

with the microscopic current $\widetilde{\mathbf{j}}^{\lambda}_{\mathbf{k}} \equiv -\frac{|e|}{\hbar}\nabla_{\mathbf{k}} E^{\mathrm{ren}}_{\lambda,\mathbf{k}}$ of the renormalized bands $E^{\mathrm{ren}}_{\lambda,\mathbf{k}}$ defined in (3.14), the Berry curvature $\mathbf{\Omega}^{\lambda}_{\mathbf{k}} \equiv \nabla_{\mathbf{k}} \times \boldsymbol{\mathcal{A}}^{\lambda}_{\mathbf{k}}$, and the renormalized Rabi energy $\Omega^{\lambda\nu}_{\mathbf{k}}$ defined in Equation (3.15). $\mathbf{J}[\Delta\langle 2\rangle]$ denotes doublet contributions to the macroscopic current density that originate from the Coulomb-interaction term in the Hamiltonian in Eq. (B.5).

Appendix C

Microscopic Scattering Model

The microscopic scattering model used in our lightwave investigations is implemented by

$$\mathrm{i}\hbar\frac{\partial}{\partial t}P_{\mathbf{k}} = S_{\mathbf{k}}\Big[P_{\mathbf{k}}, f_{\mathbf{k}}^{\mathrm{e/h}}\Big] - \mathrm{i}\sum_{\mathbf{k}'}\gamma_{\mathbf{k},\mathbf{k}'}^{\mathrm{EID}}R_{\mathbf{k}'}\ , \tag{C.1}$$

$$\mathrm{i}\hbar\frac{\partial}{\partial t}R_{\mathbf{k}} = S_{\mathbf{k}}\Big[R_{\mathbf{k}}, f_{\mathbf{k}}^{\mathrm{e/h}}\Big]\Big|_{\mathbf{d}_{\mathbf{k}}^{c,v}=0} + \mathrm{i}\sum_{\mathbf{k}'}\gamma_{\mathbf{k},\mathbf{k}'}^{\mathrm{EID}}P_{\mathbf{k}'} - \mathrm{i}\sum_{\mathbf{k}'}\gamma_{\mathbf{k},\mathbf{k}'}^{\mathrm{QM}}R_{\mathbf{k}'}\ , \tag{C.2}$$

where the functional $S_{\mathbf{k}}$ is short hand for the singlet term in the right-hand side of the SBE (3.13a). The dynamic nature of microscopic scattering, which results in quantum memory effects discussed in Section 3.4.3, is described by introducing a second, polarization-like singlet $R_{\mathbf{k}}$ following the description of Ref. [87]. The new singlet is generated by the scattering of $P_{\mathbf{k}}$ and, once formed, adds scattering to the $P_{\mathbf{k}}$ dynamics. The scattering is described by a diffusive model

$$\gamma_{\mathbf{k},\mathbf{k}'}^{\mathrm{EID}} = \delta_{\mathbf{k},\mathbf{k}'}\gamma_{\mathbf{k}}^{(1)} - \gamma_{\mathbf{k},\mathbf{k}'}^{(2)} + \delta_{\mathbf{k},\mathbf{k}'}\gamma_{\mathbf{k}}^{\mathrm{phonon}}\ , \quad \gamma_{\mathbf{k},\mathbf{k}'}^{\mathrm{QM}} = s_{\mathrm{QM}}\gamma_{\mathbf{k},\mathbf{k}'}^{\mathrm{EID}}\ , \tag{C.3}$$

where the factor $s_{\mathrm{QM}} > 4$ determines the strength of scattering for $R_{\mathbf{k}}$ itself and sets the strength of the quantum-memory effect.

Appendix D

Numerical Implementation of the SBEs

D.1 Crystal structure of TMDs

The hexagonal lattice of two-dimensional TMDs is described by the primitive lattice vectors

$$\mathbf{a}_1 = \begin{pmatrix} a \\ 0 \\ 0 \end{pmatrix}, \quad \mathbf{a}_2 = \begin{pmatrix} a/2 \\ \sqrt{3}a/2 \\ 0 \end{pmatrix}, \quad \mathbf{a}_3 = \begin{pmatrix} 0 \\ 0 \\ c \end{pmatrix}, \tag{D.1}$$

with lattice constant a and a separation of layers $c \to \infty$. From these, the reciprocal lattice vectors are defined by

$$\mathbf{b}_i = \frac{2\pi}{V} \mathbf{a}_j \times \mathbf{a}_k \,, \tag{D.2}$$

where (i, j, k) is a cyclic permutation of $(1, 2, 3)$ and $V = \mathbf{a}_1 \cdot (\mathbf{a}_2 \times \mathbf{a}_3) = \sqrt{3}ac/2$ is the unit cell volume. We obtain

$$\mathbf{b}_1 = \frac{2\pi}{a} \begin{pmatrix} 1 \\ -1/\sqrt{3} \\ 0 \end{pmatrix}, \quad \mathbf{b}_2 = \frac{2\pi}{a} \begin{pmatrix} 0 \\ 2/\sqrt{3} \\ 0 \end{pmatrix}, \tag{D.3}$$

with $\left|\mathbf{b}_{1/2}\right| = 4\pi/(\sqrt{3}a)$.

The important high-symmetry points K and K' are separated by

$$|K - K'| = 4\pi/(3a) \ , \tag{D.4}$$

in momentum space. For WSe_2 with a lattice constant of $a = 0.3325$ nm, this yields $|K - K'| = 12.60\ \mathrm{nm}^{-1}$.

D.2 Discretization of momentum space

The honeycomb lattice structure of TMDs yields a hexagonal first Brillouin zone (Fig. D.1, red line). For numerical purposes, it is more convenient to choose a rhombic primitive cell in reciprocal space (Fig. D.1, blue lines). We choose the vectors

$$\mathbf{c}_1 = \left(\frac{4\pi}{3a}\right)\begin{pmatrix} 3/2 \\ -\sqrt{3}/2 \end{pmatrix} \ , \quad \mathbf{c}_2 = \left(\frac{4\pi}{3a}\right)\begin{pmatrix} 3/2 \\ \sqrt{3}/2 \end{pmatrix} \ , \tag{D.5}$$

to span the rhombic cell and discretize it with $N \times N$ points

$$\mathbf{k}_{i,j} = \frac{i-1}{N}\mathbf{c}_1 + \frac{j-1}{N}\mathbf{c}_2 = \left(\frac{4\pi}{3a}\right)\begin{pmatrix} 3(i+j-2)/(2N) \\ \sqrt{3}(i-j)/(2N) \end{pmatrix} \ , \tag{D.6}$$

with $(i, j = 1, \ldots N)$. Each grid point (Fig. D.1, red points) represents a hexagonal area $\mathcal{A}$ surrounding it (Fig. D.1, small hexagons). This grid discretizes the Brillouin zone via a simple two-dimensional grid where periodic boundary conditions are easily implemented.

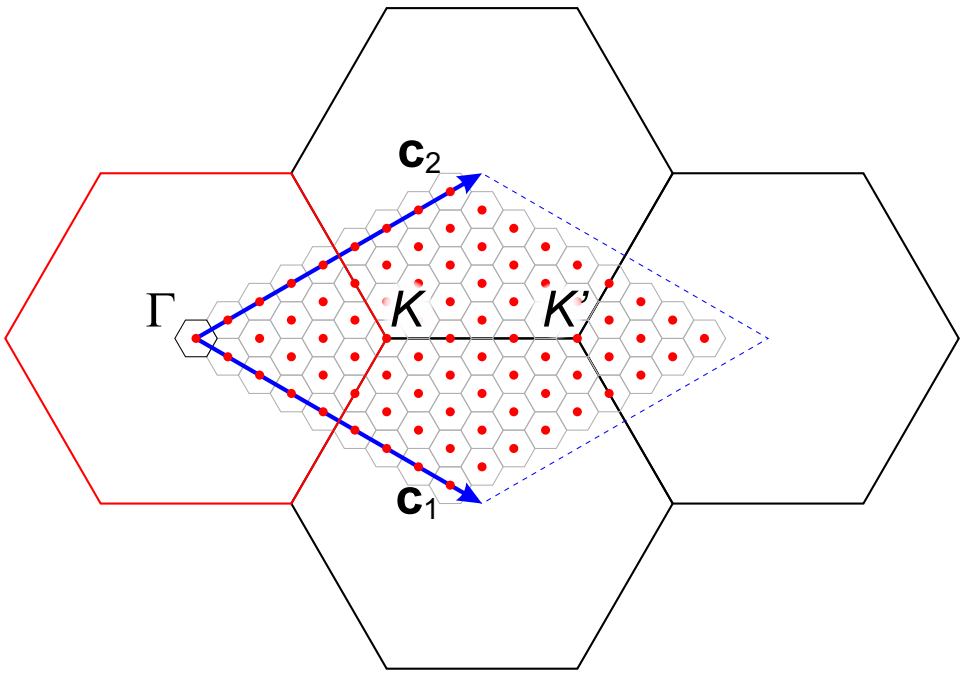

Figure D.1: Discretization of the primitive cell. An alternative to the hexagonal Brillouin zone (red hexagon) of two-dimensional TMDs is a rhombic primitive cell (dashed blue line) spanned by vectors $\mathbf{c}_1$ and $\mathbf{c}_2$ (blue arrows) and with Γ points on its corners. The rhombic shape is discretized with a two-dimensional grid (red dots) where each dot represents a hexagonal area (small hexagons) around it.

D.3 Coulomb sum

In the SBEs, we encounter Coulomb sums of the form

$$I_{\mathbf{k}} = \sum_{\mathbf{k}'} V_{\mathbf{k},\mathbf{k}'} f_{\mathbf{k}'} \ , \tag{D.7}$$

that run over discrete $\mathbf{k}$ created by a finite quantization length $\mathcal{L}$. In the continuum limit ($\mathcal{L} \to \infty$), the discrete sum can be treated as a Riemann sum and converted into the integral

$$I_{\mathbf{k}} \to \left(\frac{\mathcal{L}}{2\pi}\right)^2 \int_{\mathrm{BZ}} \mathrm{d}^2k' \, V_{\mathbf{k},\mathbf{k}'} f_{\mathbf{k}'} \ , \tag{D.8}$$

over the entire Brillouin zone. This integral can be split into smaller pieces using the discretization (D.6), replacing $\int_{\mathrm{BZ}} \mathrm{d}^2k = \sum_{i,j} \int_{\mathbf{k}_{i,j}+\mathcal{A}} \mathrm{d}^2k$. In the Coulomb sum, $f_{\mathbf{k}}$ typically

changes slowly on the scale of the numerical grid and can be approximated to be constant within the area $\mathcal{A}$ (for $\mathbf{k} \in \mathbf{k}_{i,j} + \mathcal{A}: \; f_{\mathbf{k}} = f_{\mathbf{k}_{i,j}}$) so that we can write

$$I_{\mathbf{k}} \approx \sum_{i,j} V^{\text{num}}_{\mathbf{k},\mathbf{k}_{i,j}} f_{\mathbf{k}_{i,j}} \; , \tag{D.9}$$

with

$$V^{\text{num}}_{\mathbf{k},\mathbf{k}_{i,j}} \equiv \left(\frac{\mathcal{L}}{2\pi}\right)^2 \int_{\mathbf{k}_{i,j}+\mathcal{A}} \mathrm{d}^2 k' \, V_{\mathbf{k},\mathbf{k}_{i,j}} \; . \tag{D.10}$$

In contrast, $V_{\mathbf{k},\mathbf{k}'}$ can change quickly within the area $\mathcal{A}$, especially near the Coulomb singularity at $\mathbf{k} = \mathbf{k}'$. In order to take into account the fast changes and lift the integrable

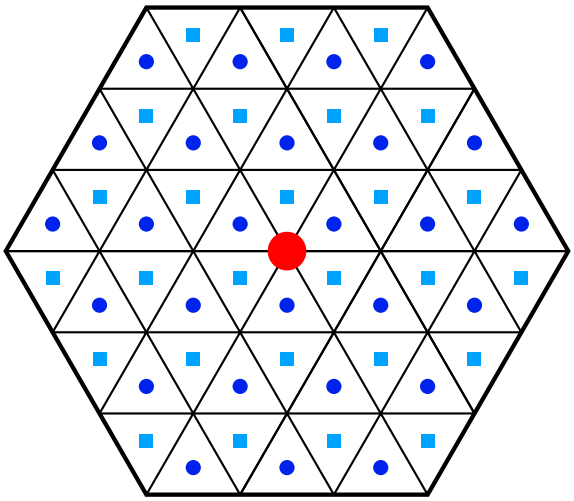

Figure D.2: Tiling of the discretization area. The hexagonal area around a grid point (red dot) is discretized with a fine grid (blue dots and squares) where each point represents a triangular area around it.

Coulomb singularity, we numerically evaluate the integral (D.10) by tiling the hexagon $\mathcal{A}$ with $6N^2_{\text{fine}}$ triangles as shown in Fig. D.2. As a result, (D.10) is approximated by the sum

$$V^{\text{num}}_{\mathbf{k},\mathbf{k}_{i,j}} \approx \left(\frac{\mathcal{L}}{2\pi}\right)^2 \sum_{\alpha,\beta,\gamma,\delta} \Delta A \, V_{\mathbf{k},\mathbf{k}^{\text{fine}}_{i,j;\alpha,\beta,\gamma,\delta}} \; . \tag{D.11}$$

γ	1	2	3	4	5	6
$\mathbf{A}_1^\gamma$	$\begin{pmatrix}1\\0\end{pmatrix}$	$\begin{pmatrix}1/2\\\sqrt{3}/2\end{pmatrix}$	$\begin{pmatrix}-1/2\\\sqrt{3}/2\end{pmatrix}$	$\begin{pmatrix}-1\\0\end{pmatrix}$	$\begin{pmatrix}-1/2\\-\sqrt{3}/2\end{pmatrix}$	$\begin{pmatrix}1/2\\-\sqrt{3}/2\end{pmatrix}$
$\mathbf{A}_2^\gamma$	$\begin{pmatrix}1/2\\\sqrt{3}/2\end{pmatrix}$	$\begin{pmatrix}-1/2\\\sqrt{3}/2\end{pmatrix}$	$\begin{pmatrix}-1\\0\end{pmatrix}$	$\begin{pmatrix}-1/2\\-\sqrt{3}/2\end{pmatrix}$	$\begin{pmatrix}1/2\\-\sqrt{3}/2\end{pmatrix}$	$\begin{pmatrix}1\\0\end{pmatrix}$
$\mathbf{B}_1^\gamma$	$\begin{pmatrix}1/2\\1/(2\sqrt{3})\end{pmatrix}$	$\begin{pmatrix}0\\1/\sqrt{3}\end{pmatrix}$	$\begin{pmatrix}-1/2\\1/(2\sqrt{3})\end{pmatrix}$	$\begin{pmatrix}-1/2\\-1/(2\sqrt{3})\end{pmatrix}$	$\begin{pmatrix}0\\-1/\sqrt{3}\end{pmatrix}$	$\begin{pmatrix}1/2\\-1/(2\sqrt{3})\end{pmatrix}$
$\mathbf{B}_2^\gamma$	$\begin{pmatrix}1\\1/\sqrt{3}\end{pmatrix}$	$\begin{pmatrix}0\\2/\sqrt{3}\end{pmatrix}$	$\begin{pmatrix}-1\\1/\sqrt{3}\end{pmatrix}$	$\begin{pmatrix}-1\\-1/\sqrt{3}\end{pmatrix}$	$\begin{pmatrix}0\\-2/\sqrt{3}\end{pmatrix}$	$\begin{pmatrix}1\\-1/\sqrt{3}\end{pmatrix}$

Table D.1: Vectors for fine integration.

over the $6N_{\rm fine}^2$ points

$$\mathbf{k}^{\rm fine}_{i,j;\alpha,\beta,\gamma,\delta} = \mathbf{k}_{i,j} + \left(\frac{4\pi}{3aN}\right)[(\alpha-1)\mathbf{A}_1^\gamma + (\beta-1)\mathbf{A}_2^\gamma + \mathbf{B}_\delta^\gamma]/N_{\rm fine}\ , \tag{D.12}$$

with

$$\alpha = 1,\ldots,N_{\rm fine}\ ;\ \beta = 1,\ldots,N_{\rm fine}+1-\alpha\ ; \qquad \text{if } \delta = 1\ , \tag{D.13}$$

$$\alpha = 1,\ldots,N_{\rm fine}-1;\ \beta = 1,\ldots N_{\rm fine}-\alpha\ ; \qquad \text{if } \delta = 2\ , \tag{D.14}$$

$$\gamma = 1,\ldots,6\ ; \tag{D.15}$$

$$\delta = 1,2\ . \tag{D.16}$$

The vectors $\mathbf{A}_{1/2}^\gamma$ and $\mathbf{B}_\delta^\gamma$ are defined in Table D.1 and $\Delta A = 8\pi^2/(18a^2N^2N_{\rm fine}^2)$.

Appendix E

Band-Pass Filter

We define a gate function

$$G(\omega) = \frac{1}{\mathrm{e}^{(\omega-\omega_2)/\Delta\omega}+1} - \frac{1}{\mathrm{e}^{(\omega-\omega_1)/\Delta\omega}+1} \,, \tag{E.1}$$

that passes frequencies between angular frequencies ω_1 and $\omega_2 > \omega_1$ to define a band-pass filter where $\Delta\omega$ sets the steepness of the cutoffs. The resulting band-pass filter can be applied to a time-dependent function $P(t)$ by computing

$$P_{\text{filtered}}(t) = \int \mathrm{d}t'\, P(t')G(t-t') \,, \tag{E.2}$$

where

$$G(t) = \frac{\Delta\omega \sin\left(\frac{\omega_2-\omega_1}{2}t\right)}{\sinh(\pi\Delta\omega\, t)} \mathrm{e}^{-\mathrm{i}\frac{\omega_1+\omega_2}{2}t} \,, \tag{E.3}$$

is the Fourier transformation of $G(\omega)$ in Eq. (E.1).

Appendix F

Inhomogeneous SBEs

The exact singlet dynamics is given by

$$
\begin{aligned}
\mathrm{i}\hbar\frac{\partial}{\partial t}P_{\mathbf{k}}^{\lambda\nu}(\mathbf{R}) &= [E_\nu - E_\lambda]P_{\mathbf{k}}^{\lambda\nu}(\mathbf{R}) \\
&+ \left[\mathrm{e}^{\mathrm{i}F_{\nu\lambda}\nabla_{\mathbf{k}}\cdot\nabla_{\mathbf{R}_1}}(U_\nu(\mathbf{R}_1)+U_H(\mathbf{R}_1)) - \mathrm{e}^{\mathrm{i}F_{\nu\lambda}\nabla_{\mathbf{k}}\cdot\nabla_{\mathbf{R}_1}}(U_\lambda(\mathbf{R}_1)+U_H(\mathbf{R}_1))\right]P_{\mathbf{k}}^{\lambda\nu}(\mathbf{R}) \\
&+ \left[\tfrac{\hbar^2}{2}\left(\tfrac{F_{\nu\lambda}^2}{m_\lambda} - \tfrac{F_{\lambda\nu}^2}{m_\nu}\right)\nabla_{\mathbf{R}}^2 - \mathrm{i}\hbar^2\left(\tfrac{F_{\nu\lambda}}{m_\lambda} + \tfrac{F_{\lambda\nu}}{m_\nu}\right)\mathbf{k}\cdot\nabla_{\mathbf{R}} - \tfrac{\hbar^2}{2}\left(\tfrac{1}{m_\lambda} - \tfrac{1}{m_\nu}\right)\mathbf{k}^2\right]P_{\mathbf{k}}^{\lambda\nu}(\mathbf{R}) \\
&+ \sum_{\mu\neq\lambda}\left[\mathrm{e}^{-\mathrm{i}F_{\lambda\nu}\nabla_{\mathbf{k}}\cdot\nabla_{\mathbf{R}_1}}\mathrm{e}^{\mathrm{i}(F_{\mu\nu}-F_{\lambda\nu})\nabla_{\mathbf{k}}\cdot\nabla_{\mathbf{R}_2}}dE(\mathbf{R}_1)P_{\mathbf{k}}^{\mu\nu}(\mathbf{R}_2)\right] \\
&\quad + \sum_{\mu\neq\lambda}\left[\mathrm{e}^{\mathrm{i}F_{\nu\lambda}\nabla_{\mathbf{k}}\cdot\nabla_{\mathbf{R}_1}}\mathrm{e}^{\mathrm{i}(F_{\lambda\mu}-F_{\lambda\nu})\nabla_{\mathbf{k}}\cdot\nabla_{\mathbf{R}_2}}dE(\mathbf{R}_1)P_{\mathbf{k}}^{\lambda\mu}(\mathbf{R}_2)\right] \\
&+ \sum_{\mu}\mathrm{e}^{\mathrm{i}(F_{\lambda\mu}-F_{\lambda\nu})\nabla_{\mathbf{k}_1}\cdot\nabla_{\mathbf{R}_1}}\mathrm{e}^{\mathrm{i}(F_{\mu\nu}-F_{\lambda\nu})\nabla_{\mathbf{k}_2}\cdot\nabla_{\mathbf{R}_2}}\mathrm{e}^{\mathrm{i}F_{\nu\lambda}\nabla_{\mathbf{k}_1}\cdot\nabla_{\mathbf{R}_2}}\mathrm{e}^{-\mathrm{i}F_{\lambda\nu}\nabla_{\mathbf{k}_2}\cdot\nabla_{\mathbf{R}_1}} \\
&\quad \times\left[\Delta_{\mathbf{k}_1}^{\lambda\mu}(\mathbf{R}_1)P_{\mathbf{k}_2}^{\mu\nu}(\mathbf{R}_2) - P_{\mathbf{k}_1}^{\lambda\mu}(\mathbf{R}_1)\Delta_{\mathbf{k}_2}^{\mu\nu}(\mathbf{R}_2)\right] \\
&+ \sum_{\mu}\mathrm{e}^{\frac{\mathrm{i}}{2}(2F_{\nu\lambda}-F_{\mu\lambda})\nabla_{\mathbf{k}_1}\cdot\nabla_{\mathbf{R}}}\mathrm{e}^{\frac{\mathrm{i}}{2}(F_{\mu\nu}-2F_{\lambda\nu})\nabla_{\mathbf{k}_2}\cdot\nabla_{\mathbf{R}}}\sum_{\mathbf{Q}}\mathrm{e}^{\mathbf{Q}\cdot(F_{\mu\nu}\nabla_{\mathbf{k}_2}-F_{\mu\lambda}\nabla_{\mathbf{k}_1})} \\
&\quad \times\left[\frac{1}{\mathcal{S}}\sum_{\mathbf{q}}V_{\mathbf{k}_1-\mathbf{q}}C_{\lambda\mu,\mu\nu}^{\mathbf{q},\mathbf{k}_2,\mathbf{Q}}(\mathbf{R}) - \frac{1}{\mathcal{S}}\sum_{\mathbf{q}}V_{\mathbf{k}_2-\mathbf{q}}C_{\lambda\mu,\mu\nu}^{\mathbf{k}_1,\mathbf{q},\mathbf{Q}}(\mathbf{R})\right]. \qquad \text{(F.1)}
\end{aligned}
$$

For the purpose of denoting the variables that gradients operate on, additional coordinates $\mathbf{R}_1 = \mathbf{R}_2 = \mathbf{R}$ and $\mathbf{k}_1 = \mathbf{k}_2 = \mathbf{k}$ were introduced. We also identified the Hartree potential

$$U_H(\mathbf{R}) \equiv \int \mathrm{d}^3x\, V(\mathbf{R}-\mathbf{r}) \sum_\alpha \frac{1}{\mathcal{S}} \sum_{\mathbf{k}} P^{\alpha\alpha}_{\mathbf{k}}(\mathbf{R}) \;, \tag{F.2}$$

and defined a short hand for Coulomb sums

$$\Delta^{\lambda\nu}_{\mathbf{k}}(\mathbf{R}) \equiv \frac{1}{\mathcal{S}} \sum_{\mathbf{q}} V_{\mathbf{k}-\mathbf{q}} P^{\lambda\nu}_{\mathbf{k}}(\mathbf{R}) \;. \tag{F.3}$$

Appendix G

Inhomogeneous SBEs of a Two-Band Model

Using the power series (7.10), the singlet dynamics (F.1) yields

$$
\begin{aligned}
\mathrm{i}\hbar\frac{\partial}{\partial t}P_{\mathbf{k}}(\mathbf{R}) = \widetilde{E}^{eh}_{\mathbf{k}}P_{\mathbf{k}}(\mathbf{R}) - \frac{\hbar^2}{2M}\nabla^2_{\mathbf{R}}P_{\mathbf{k}}(\mathbf{R}) \\
+\mathrm{i}\nabla_{\mathbf{R}}\big[\bar{m}_e U_e(\mathbf{R}) - \bar{m}_h U_h(\mathbf{R}) + U_H(\mathbf{R}) + \bar{m}_e\Delta^h_{\mathbf{k}}(\mathbf{R}) - \bar{m}_h\Delta^e_{\mathbf{k}}(\mathbf{R})\big]\cdot\nabla_{\mathbf{k}}P_{\mathbf{k}}(\mathbf{R}) \\
+\mathrm{i}\nabla_{\mathbf{k}}(\bar{m}_e\Delta^e_{\mathbf{k}}(\mathbf{R}) - \bar{m}_h\Delta^h_{\mathbf{k}}(\mathbf{R}))\cdot\nabla_{\mathbf{R}}P_{\mathbf{k}}(\mathbf{R}) \\
-\big(1 - f^e_{\mathbf{k}}(\mathbf{R}) - f^h_{\mathbf{k}}(\mathbf{R}) - \mathrm{i}\tfrac{m_h-m_e}{2M}\nabla_{\mathbf{k}}\cdot\nabla_{\mathbf{R}}(f^e_{\mathbf{k}}(\mathbf{R}) + f^h_{\mathbf{k}}(\mathbf{R}))\big)\Omega_{\mathbf{k}}(\mathbf{R}) \\
-\nabla_{\mathbf{R}}\Omega_{\mathbf{k}}(\mathbf{R})\cdot\nabla_{\mathbf{k}}(\bar{m}_e f^e_{\mathbf{k}}(\mathbf{R}) - \bar{m}_h f^h_{\mathbf{k}}(\mathbf{R})) - \mathrm{i}\nabla_{\mathbf{k}}\Omega_{\mathbf{k}}(\mathbf{R})\cdot\nabla_{\mathbf{R}}(\bar{m}_e f^h_{\mathbf{k}}(\mathbf{R}) - \bar{m}_h f^e_{\mathbf{k}}(\mathbf{R})) \\
+\Gamma^{vc}_{\mathbf{k}}(\mathbf{R}) + \mathcal{O}([\nabla_{\mathbf{k}}\cdot\nabla_{\mathbf{R}}]^2)\,, \qquad \text{(G.1)}
\end{aligned}
$$

and

$$\hbar\frac{\partial}{\partial t}f^e_{\mathbf{k}}(\mathbf{R}) = 2\mathrm{iIm}[P_{\mathbf{k}}(\mathbf{R})\Omega^*_{\mathbf{k}}(\mathbf{R})] - \tfrac{\hbar^2}{m_e}\mathbf{k}\cdot\nabla_{\mathbf{R}}f^e_{\mathbf{k}}(\mathbf{R}) + \nabla_{\mathbf{R}}(U_e(\mathbf{R})+U_H(\mathbf{R}))\cdot\nabla_{\mathbf{k}}f^e_{\mathbf{k}}(\mathbf{R})$$
$$+ \tfrac{m_h-m_e}{M}\mathrm{Re}[P_{\mathbf{k}}(\mathbf{R})(\nabla_{\mathbf{k}}\cdot\nabla_{\mathbf{R}}\Omega_{\mathbf{k}}(\mathbf{R}))^* - (\nabla_{\mathbf{k}}\cdot\nabla_{\mathbf{R}}P_{\mathbf{k}}(\mathbf{R}))\Omega_{\mathbf{k}}(\mathbf{R})^*]$$
$$+ \mathrm{Re}[\nabla_{\mathbf{R}}P_{\mathbf{k}}(\mathbf{R})\cdot\nabla_{\mathbf{k}}\Omega^*_{\mathbf{k}}(\mathbf{R}) - \nabla_{\mathbf{k}}P_{\mathbf{k}}(\mathbf{R})\cdot\nabla_{\mathbf{R}}\Omega^*_{\mathbf{k}}(\mathbf{R})]$$
$$+ \nabla_{\mathbf{R}}f^e_{\mathbf{k}}(\mathbf{R})\cdot\nabla_{\mathbf{k}}\Delta^e_{\mathbf{k}}(\mathbf{R}) - \nabla_{\mathbf{k}}f^e_{\mathbf{k}}(\mathbf{R})\cdot\nabla_{\mathbf{R}}\Delta^e_{\mathbf{k}}(\mathbf{R})$$
$$- \mathrm{i}\bar{m}_e\tfrac{1}{\mathcal{S}}\sum_{\mathbf{q}}V_{\mathbf{k}-\mathbf{q}}\sum_{\mathbf{Q}}\mathbf{Q}\cdot\nabla_{\mathbf{k}}\Big[c_X^{\mathbf{q},\mathbf{k},\mathbf{Q}} + c_X^{\mathbf{k},\mathbf{q},\mathbf{Q}}\Big]$$
$$+ \mathrm{i}\bar{m}_e\tfrac{1}{\mathcal{S}}\sum_{\mathbf{q}}[\nabla_{\mathbf{k}}V_{\mathbf{k}-\mathbf{q}}]\cdot\sum_{\mathbf{Q}}\mathbf{Q}\Big[c_X^{\mathbf{q},\mathbf{k},\mathbf{Q}} + c_X^{\mathbf{k},\mathbf{q},\mathbf{Q}}\Big] \tag{G.2}$$
$$+ \tfrac{1}{2}\sum_{\mathbf{Q}}\tfrac{1}{\mathcal{S}}\sum_{\mathbf{q}}\Big[(\nabla_{\mathbf{k}}V_{\mathbf{k}-\mathbf{q}})\cdot\nabla_{\mathbf{R}}(\bar{m}_e c_X^{\mathbf{q},\mathbf{k},\mathbf{Q}} + \bar{m}_h c^{\mathbf{k},\mathbf{q},\mathbf{Q}})$$
$$- V_{\mathbf{k}-\mathbf{q}}\nabla_{\mathbf{k}}\cdot\nabla_{\mathbf{R}}(\bar{m}_h c_X^{\mathbf{q},\mathbf{k},\mathbf{Q}} + \bar{m}_e c^{\mathbf{k},\mathbf{q},\mathbf{Q}})\Big]$$
$$+ \mathcal{O}([\nabla_{\mathbf{k}}\cdot\nabla_{\mathbf{R}}]^2)\,. \tag{G.3}$$

We identified the renormalized kinetic energy

$$\widetilde{E}^{eh}_{\mathbf{k}}(\mathbf{R}) \equiv E_{\mathrm{gap}} + \frac{\hbar^2\mathbf{k}^2}{2\mu} + [U_{\mathrm{c}}(\mathbf{R}) - U_{\mathrm{v}}(\mathbf{R})]$$
$$- \big[\Delta^e_{\mathbf{k}}(\mathbf{R}) + \Delta^h_{\mathbf{k}}(\mathbf{R})\big] - \mathrm{i}\tfrac{m_h-m_e}{2M}\big[\Delta^e_{\mathbf{k}}(\mathbf{R}) + \Delta^h_{\mathbf{k}}(\mathbf{R})\big]\,, \tag{G.4}$$

the renormalized Rabi energy

$$\Omega_{\mathbf{k}}(\mathbf{R}) \equiv dE(\mathbf{R}) + \sum_{\mathbf{k}'}V_{\mathbf{k}-\mathbf{k}'}P_{\mathbf{k}'}(\mathbf{R})\,, \tag{G.5}$$

the reduced mass $\mu = (1/m_e + 1/m_h)^{-1}$, and defined $\Delta^e_{\mathbf{k}} \equiv \Delta^{c,c}_{\mathbf{k}}$ and $\Delta^h_{\mathbf{k}} \equiv \Delta^{v,v}_{\mathbf{k}}$ based on Eq. (F.3).

Appendix H

Author's contributions

All studies presented in this Thesis are the result of frequent meetings and intensive discussions with my advisor Mackillo Kira where intermediate results were discussed and new calculations planned. Most of the actual programming and calculations have been performed by myself.

My work related to lightwave electronics was in large parts driven by a collaboration with the group of Rupert Huber (University of Regensburg) who performed various measurements of harmonic-sideband (HSB) spectra in quantum materials. In a first project, I analyzed time-resolved HSB spectrograms that showed differences in the optimum delay between measurements in bulk and monolayer tungsten diselenide (WSe_2) which we hypothesized to originate from differences in the interaction strength within the two materials. Together with Benjamin Girodias, we first started using a code developed by Peter Hawkins. Together, we extended the code to use a diffusive scattering model which we fitted to scattering computations performed by Johannes Steiner (now University of Paderborn) in the group of Stephan Koch (University of Marburg). However, the numerical methods used in the original code were unable to explain the experiments. In a shift from the old code base, I developed a completely new code with a different numerical approach to solve the semiconductor Bloch equations on the full two-dimensional Brillouin zone combined with inputs from tight-binding models (later extended to use density-matrix theory computations). This

new approach was able to explain the experimental data quantitatively. Together with a Wigner-function based representation of the microscopic state in phase space that I developed, we were able to confirm our hypothesis. The results were published in J. Freudenstein, M. Borsch, M. Meierhofer, D. Afanasiev, C. P. Schmid, F. Sandner, M. Liebich, A. Girnghuber, M. Knorr, M. Kira, and R. Huber, "Attosecond clocking of correlations between Bloch electrons", Nature **610**, 7931 (2022). I performed all quantum-mechanical computations presented in the paper, contributed to the writing of the manuscript, and was mainly responsible for writing of the theory part of the Methods section. I also presented the results at the CLEO conference in San Jose, CA, in 2023.

I also worked on a second set of HSB measurements performed in Rupert Huber's group. This time, HSB spectra were measured as function of the peak field strength and central frequency of the HSB-generating multi-terahertz pulse with the goal to understand the extremely non-perturbative dependence of the HSB intensities. Together with Mackillo Kira, I discovered the emergence of crystal-momentum combs and found that they could be used to connect the HSB intensities to the band structure and explain their nonperturbative behavior. In many meetings and discussions between Mackillo Kira, Rupert Huber's group, and myself, we eventually formulated the technique of lightwave tomography that was published in M. Borsch, C. P. Schmid, L. Weigl, S. Schlauderer, N. Hofmann, C. Lange, J. T. Steiner, S. W. Koch, R. Huber, and M. Kira, "Super-resolution lightwave tomography of electronic bands in quantum materials", Science **370**, 1204–1207 (2020). I performed all quantum-mechanical computations, contributed to the writing of the manuscript, and was responsible for writing of the theory part of the Supplementary Material. I presented the results of this publication at several international and national conferences, including the CLEO conference in 2021 (San Jose, CA) and ATTO VIII in 2022 (Orlando, FL).

Based on the insights gained from the collaboration with Rupert Huber, I also theoretically explored the limitations of lightwave valleytronic switching. This work is mainly the result of frequent meetings and discussions between Mackillo Kira and myself where we

discussed intermediate results and planned computational investigations. The results are summarized in Section 6 and are in preparation for publication at the time of this writing. Preliminary results were presented in several posters as well as a talk at the CLEO conference in San Jose, CA, in 2019.

Together with Mackillo Kira, Rupert Huber, and Manuel Meierhofer (University of Regensburg) I wrote a review article on lightwave electronics in condensed matter, published as M. Borsch, M. Meierhofer, R. Huber, M. Kira, "Lightwave electronics in condensed matter", Nat. Rev. Mater. **8**, 668–687 (2023). I contributed to the researching and writing of the manuscript and performed quantum-mechanical computations.

The work on spatially inhomogeneous excitations presented Chapters 7 and 8 was a continuation of my Master's thesis in which I started to develop the microscopic theory. During my PhD work, I further refined the approach and developed a code to numerically solve the theory. I performed extensive analytical and numerical studies to compare our theory to experimental measurements of the spatio-temporal dynamics of coherent excitons performed by Eric Martin in the group of Steven Cundiff (University of Michigan). A subset of the results are discussed in Chapter 8 and were presented at several international conferences, including a contributed talk at the CLEO conference in San Jose, CA, in 2018.

The theory developed for spatially inhomogeneous excitations was later extended to describe the macroscopic dynamics of incoherent excitons and compared to experiments in the group of Parag Deotare (University of Michigan). I contributed to analytical and numerical studies to explain the measured dynamics of incoherent excitons which were discussed in regular meetings between Mackillo Kira, Parag Deotare, Matthias Florian (University of Michigan), Zidong Li (University of Michigan), and myself. The results are published in Z. Li, M. Florian, K. Datta, Z. Jiang, M. Borsch, Q. Wen, M. Kira, and P. B.Deotare, "Enhanced exciton-drift transport through suppressed diffusion in one-dimensional guides", ACS Nano, https://doi.org/10.1021/acsnano.3c04870 (2023). I have mainly contributed to writing of the Supplementary Material.

Bibliography

[1] C. A. Mack, "Fifty years of Moore's law", IEEE Transactions on Semiconductor Manufacturing **24**, 202–207 (2011).

[2] M. M. Waldrop, "The chips are down for Moore's law", Nature News **530**, 144 (2016).

[3] J. P. Dowling and G. J. Milburn, "Quantum technology: the second quantum revolution", Philosophical Transactions of the Royal Society of London. Series A: Mathematical, Physical and Engineering Sciences **361**, edited by A. G. J. MacFarlane, 1655–1674 (2003).

[4] N. W. Ashcroft, *Solid state physics* (Holt, Rinehart and Winston, 1976).

[5] C. Kittel, *Introduction to Solid State Physics*, 8th edition (Wiley, Hoboken, NJ, Nov. 2004).

[6] T. D. Ladd, F. Jelezko, R. Laflamme, Y. Nakamura, C. Monroe, and J. L. O'Brien, "Quantum computers", Nature **464**, 45–53 (2010).

[7] L. Gyongyosi and S. Imre, "A survey on quantum computing technology", Computer Science Review **31**, 51–71 (2019).

[8] N. Gisin and R. Thew, "Quantum communication", Nature Photonics **1**, 165–171 (2007).

[9] A. Orieux and E. Diamanti, "Recent advances on integrated quantum communications", Journal of Optics **18**, 083002 (2016).

[10] C. Degen, F. Reinhard, and P. Cappellaro, "Quantum sensing", Reviews of Modern Physics **89**, 035002 (2017).

[11] S. Pirandola, B. R. Bardhan, T. Gehring, C. Weedbrook, and S. Lloyd, "Advances in photonic quantum sensing", Nature Photonics **12**, 724–733 (2018).

[12] P. Michler, ed., *Quantum Dots for Quantum Information Technologies* (Springer International Publishing, 2017).

[13] M. Kjaergaard, M. E. Schwartz, J. Braumüller, P. Krantz, J. I.-J. Wang, S. Gustavsson, and W. D. Oliver, "Superconducting qubits: current state of play", Annual Review of Condensed Matter Physics **11**, 369–395 (2020).

[14] I. Buluta, S. Ashhab, and F. Nori, "Natural and artificial atoms for quantum computation", Reports on Progress in Physics **74**, 104401 (2011).

[15] L. Henriet, L. Beguin, A. Signoles, T. Lahaye, A. Browaeys, G.-O. Reymond, and C. Jurczak, "Quantum computing with neutral atoms", Quantum **4**, 327 (2020).

[16] P. Kok, W. J. Munro, K. Nemoto, T. C. Ralph, J. P. Dowling, and G. J. Milburn, "Linear optical quantum computing with photonic qubits", Reviews of Modern Physics **79**, 135–174 (2007).

[17] J. Wang, F. Sciarrino, A. Laing, and M. G. Thompson, "Integrated photonic quantum technologies", Nature Photonics **14**, 273–284 (2019).

[18] R. Schirhagl, K. Chang, M. Loretz, and C. L. Degen, "Nitrogen-vacancy centers in diamond: nanoscale sensors for physics and biology", Annual Review of Physical Chemistry **65**, 83–105 (2014).

[19] M. W. Day, K. M. Bates, C. L. Smallwood, R. C. Owen, T. Schröder, E. Bielejec, R. Ulbricht, and S. T. Cundiff, "Coherent interactions between silicon-vacancy centers in diamond", Physical Review Letters **128**, 203603 (2022).

[20] M. Borsch, M. Meierhofer, R. Hubert, and M. Kira, "Lightwave electronics in condensed matter", Nature Reviews Materials, accepted (2023).

[21] E. Goulielmakis, V. S. Yakovlev, A. L. Cavalieri, M. Uiberacker, V. Pervak, A. Apolonski, R. Kienberger, U. Kleineberg, and F. Krausz, "Attosecond control and measurement: Lightwave electronics", Science **317**, 769–775 (2007).

[22] J. J. Macklin, J. D. Kmetec, and C. L. Gordon, "High-order harmonic generation using intense femtosecond pulses", Physical Review Letters **70**, 766–769 (1993).

[23] A. L'Huillier and P. Balcou, "High-order harmonic generation in rare gases with a 1-ps 1053-nm laser", Physical Review Letters **70**, 774–777 (1993).

[24] P. B. Corkum, "Plasma perspective on strong field multiphoton ionization", Physical Review Letters **71**, 1994–1997 (1993).

[25] N. Dudovich, O. Smirnova, J. Levesque, Y. Mairesse, M. Y. Ivanov, D. M. Villeneuve, and P. B. Corkum, "Measuring and controlling the birth of attosecond XUV pulses", Nature Physics **2**, 781–786 (2006).

[26] P. B. Corkum and F. Krausz, "Attosecond science", Nature Physics **3**, 381–387 (2007).

[27] F. Krausz and M. I. Stockman, "Attosecond metrology: from electron capture to future signal processing", Nature Photonics **8**, 205–213 (2014).

[28] F. Krausz, "The birth of attosecond physics and its coming of age", Physica Scripta **91**, 063011 (2016).

[29] M. Hentschel, R. Kienberger, C. Spielmann, G. A. Reider, N. Milosevic, T. Brabec, P. Corkum, U. Heinzmann, M. Drescher, and F. Krausz, "Attosecond metrology", Nature **414**, 509–513 (2001).

[30] R. Kienberger, E. Goulielmakis, M. Uiberacker, A. Baltuska, V. Yakovlev, F. Bammer, A. Scrinzi, T. Westerwalbesloh, U. Kleineberg, U. Heinzmann, M. Drescher, and F. Krausz, "Atomic transient recorder", Nature **427**, 817–821 (2004).

[31] E. Goulielmakis, M. Uiberacker, R. Kienberger, A. Baltuska, V. Yakovlev, A. Scrinzi, T. Westerwalbesloh, U. Kleineberg, U. Heinzmann, M. Drescher, and F. Krausz, "Direct measurement of light waves", Science **305**, 1267–1269 (2004).

[32] G. Sansone, E. Benedetti, F. Calegari, C. Vozzi, L. Avaldi, R. Flammini, L. Poletto, P. Villoresi, C. Altucci, R. Velotta, S. Stagira, S. D. Silvestri, and M. Nisoli, "Isolated single-cycle attosecond pulses", Science **314**, 443–446 (2006).

[33] H. Niikura, F. Légaré, R. Hasbani, A. D. Bandrauk, M. Y. Ivanov, D. M. Villeneuve, and P. B. Corkum, "Sub-laser-cycle electron pulses for probing molecular dynamics", Nature **417**, 917–922 (2002).

[34] T. Kanai, S. Minemoto, and H. Sakai, "Quantum interference during high-order harmonic generation from aligned molecules", Nature **435**, 470–474 (2005).

[35] S. Baker, J. S. Robinson, C. A. Haworth, H. Teng, R. A. Smith, C. C. Chirilă, M. Lein, J. W. G. Tisch, and J. P. Marangos, "Probing proton dynamics in molecules on an attosecond time scale", Science **312**, 424–427 (2006).

[36] J. Itatani, J. Levesque, D. Zeidler, H. Niikura, H. Pépin, J. C. Kieffer, P. B. Corkum, and D. M. Villeneuve, "Tomographic imaging of molecular orbitals", Nature **432**, 867–871 (2004).

[37] O. Smirnova, Y. Mairesse, S. Patchkovskii, N. Dudovich, D. Villeneuve, P. Corkum, and M. Y. Ivanov, "High harmonic interferometry of multi-electron dynamics in molecules", Nature **460**, 972–977 (2009).

[38] C. Vozzi, M. Negro, F. Calegari, G. Sansone, M. Nisoli, S. De Silvestri, and S. Stagira, "Generalized molecular orbital tomography", Nature Physics **7**, 822–826 (2011).

[39] F. Bloch, "Über die Quantenmechanik der Elektronen in Kristallgittern", Zeitschrift für Physik **52**, 555–600 (1929).

[40] G. H. Wannier, "The structure of electronic excitation levels in insulating crystals", Physical Review **52**, 191–197 (1937).

[41] M. Kira and S. W. Koch, *Semiconductor Quantum Optics* (Cambridge University Press, 2012).

[42] G. Wang, A. Chernikov, M. M. Glazov, T. F. Heinz, X. Marie, T. Amand, and B. Urbaszek, "Colloquium: Excitons in atomically thin transition metal dichalcogenides", Reviews of Modern Physics **90**, 021001 (2018).

[43] A. E. Almand-Hunter, H. Li, S. T. Cundiff, M. Mootz, M. Kira, and S. W. Koch, "Quantum droplets of electrons and holes", Nature **506**, 471–475 (2014).

[44] D. Van Tuan, S.-F. Shi, X. Xu, S. A. Crooker, and H. Dery, "Six-body and eight-body exciton states in monolayer WSe_2", Physical Review Letters **129**, 076801 (2022).

[45] Y. Cao, V. Fatemi, S. Fang, K. Watanabe, T. Taniguchi, E. Kaxiras, and P. Jarillo-Herrero, "Unconventional superconductivity in magic-angle graphene superlattices", Nature **556**, 43–50 (2018).

[46] J. Černe, J. Kono, M. S. Sherwin, M. Sundaram, A. C. Gossard, and G. E. W. Bauer, "Terahertz dynamics of excitons in GaAs/AlGaAs quantum wells", Physical Review Letters **77**, 1131–1134 (1996).

[47] J. R. Danielson, Y.-S. Lee, J. P. Prineas, J. T. Steiner, M. Kira, and S. W. Koch, "Interaction of strong single-cycle terahertz pulses with semiconductor quantum wells", Physical Review Letters **99**, 237401 (2007).

[48] S. Leinß, T. Kampfrath, K. v.Volkmann, M. Wolf, J. T. Steiner, M. Kira, S. W. Koch, A. Leitenstorfer, and R. Huber, "Terahertz coherent control of optically dark paraexcitons in Cu_2O", Physical Review Letters **101**, 246401 (2008).

[49] M. Wagner, H. Schneider, D. Stehr, S. Winnerl, A. M. Andrews, S. Schartner, G. Strasser, and M. Helm, "Observation of the intraexciton Autler-Townes effect in GaAs / AlGaAs semiconductor quantum wells", Physical Review Letters **105**, 167401 (2010).

[50] A. H. Chin, O. G. Calderón, and J. Kono, "Extreme midinfrared nonlinear optics in semiconductors", Physical Review Letters **86**, 3292–3295 (2001).

[51] S. Ghimire, A. D. DiChiara, E. Sistrunk, P. Agostini, L. F. DiMauro, and D. A. Reis, "Observation of high-order harmonic generation in a bulk crystal", Nature Physics **7**, 138–141 (2011).

[52] O. Schubert, M. Hohenleutner, F. Langer, B. Urbanek, C. Lange, U. Huttner, D. Golde, T. Meier, M. Kira, S. W. Koch, and R. Huber, "Sub-cycle control of terahertz high-harmonic generation by dynamical Bloch oscillations", Nature Photonics **8**, 119–123 (2014).

[53] G. Vampa, C. R. McDonald, G. Orlando, D. D. Klug, P. B. Corkum, and T. Brabec, "Theoretical analysis of high-harmonic generation in solids", Physical Review Letters **113**, 073901 (2014).

[54] G. Vampa, T. J. Hammond, N. Thiré, B. E. Schmidt, F. Légaré, C. R. McDonald, T. Brabec, and P. B. Corkum, "Linking high harmonics from gases and solids", Nature **522**, 462–464 (2015).

[55] S. Ghimire, A. D. DiChiara, E. Sistrunk, G. Ndabashimiye, U. B. Szafruga, A. Mohammad, P. Agostini, L. F. DiMauro, and D. A. Reis, "Generation and propagation of high-order harmonics in crystals", Physical Review A **85**, 043836 (2012).

[56] M. Hohenleutner, F. Langer, O. Schubert, M. Knorr, U. Huttner, S. W. Koch, M. Kira, and R. Huber, "Real-time observation of interfering crystal electrons in high-harmonic generation", Nature **523**, 572–575 (2015).

[57] J. Kono, M. Y. Su, T. Inoshita, T. Noda, M. S. Sherwin, J. Allen S. J., and H. Sakaki, "Resonant terahertz optical sideband generation from confined magnetoexcitons", Physical Review Letters **79**, 1758–1761 (1997).

[58] B. Zaks, R. B. Liu, and M. S. Sherwin, "Experimental observation of electron–hole recollisions", Nature **483**, 580–583 (2012).

[59] F. Langer, M. Hohenleutner, C. P. Schmid, C. Poellmann, P. Nagler, T. Korn, C. Schüller, M. S. Sherwin, U. Huttner, J. T. Steiner, S. W. Koch, M. Kira, and R. Huber, "Lightwave-driven quasiparticle collisions on a subcycle timescale", Nature **533**, 225–229 (2016).

[60] A. Schiffrin, T. Paasch-Colberg, N. Karpowicz, V. Apalkov, D. Gerster, S. Mühlbrandt, M. Korbman, J. Reichert, M. Schultze, S. Holzner, J. V. Barth, R. Kienberger, R. Ernstorfer, V. S. Yakovlev, M. I. Stockman, and F. Krausz, "Optical-field-induced current in dielectrics", Nature **493**, 70–74 (2013).

[61] M. Ludwig, G. Aguirregabiria, F. Ritzkowsky, T. Rybka, D. C. Marinica, J. Aizpurua, A. G. Borisov, A. Leitenstorfer, and D. Brida, "Sub-femtosecond electron transport in a nanoscale gap", Nature Physics **16**, 341–345 (2020).

[62] F. Langer, C. P. Schmid, S. Schlauderer, M. Gmitra, J. Fabian, P. Nagler, C. Schüller, T. Korn, P. G. Hawkins, J. T. Steiner, U. Huttner, S. W. Koch, M. Kira, and R. Huber, "Lightwave valleytronics in a monolayer of tungsten diselenide", Nature **557**, 76–80 (2018).

[63] J. J. Sakurai and J. Napolitano, *Modern Quantum Mechanics*, 2nd ed. (Cambridge University Press, Cambridge, 2017).

[64] C. Cohen-Tannoudji, J. Dupont-Roc, and G. Grynberg, *Photons and Atoms - Introduction to Quantum Electrodynamics* (Wiley-Interscience).

[65] M. Kira, F. Jahnke, W. Hoyer, and S. W. Koch, "Quantum theory of spontaneous emission and coherent effects in semiconductor microstructures", Progress in Quantum Electronics **23**, 189–279 (1999).

[66] M. Göppert-Mayer, "Über Elementarakte mit zwei Quantensprüngen", Annalen der Physik **401**, 273–294 (1931).

[67] G. D. Mahan, *Many-Particle Physics* (Springer Science & Business Media, Oct. 2000).

[68] A. L. Fetter and J. D. Walecka, *Quantum Theory of Many-Particle Systems* (Courier Corporation, Mar. 2012).

[69] H. Haug and S. W. Koch, *Quantum Theory of the Optical and Electronic Properties of Semiconductors: Fifth Edition* (World Scientific Publishing Company, 2009).

[70] M. Kira and S. W. Koch, "Many-body correlations and excitonic effects in semiconductor spectroscopy", Progress in Quantum Electronics **30**, 155–296 (2006).

[71] M. Kira and S. W. Koch, "Quantum-optical spectroscopy of semiconductors", Physical Review A **73**, 013813 (2006).

[72] M. Mootz, M. Kira, and S. W. Koch, "Sequential build-up of quantum-optical correlations", Journal of the Optical Society of America B **29**, A17 (2012).

[73] M. Kira, "Hyperbolic Bloch equations: Atom-cluster kinetics of an interacting Bose gas", Annals of Physics **356**, 185–243 (2015).

[74] T. T. Luu, M. Garg, S. Y. Kruchinin, A. Moulet, M. T. Hassan, and E. Goulielmakis, "Extreme ultraviolet high-harmonic spectroscopy of solids", Nature **521**, 498–502 (2015).

[75] F. Yang and R.-B. Liu, "Berry phases of quantum trajectories of optically excited electron–hole pairs in semiconductors under strong terahertz fields", New Journal of Physics **15**, 115005 (2013).

[76] G. Vampa, C. R. McDonald, G. Orlando, P. B. Corkum, and T. Brabec, "Semiclassical analysis of high harmonic generation in bulk crystals", Physical Review B **91**, 064302 (2015).

[77] L. Yue and M. B. Gaarde, "Introduction to theory of high-harmonic generation in solids: tutorial", Journal of the Optical Society of America B **39**, 535 (2022).

[78] D. Golde, T. Meier, and S. W. Koch, "High harmonics generated in semiconductor nanostructures by the coupled dynamics of optical inter- and intraband excitations", Physical Review B **77**, 075330 (2008).

[79] F. H. M. Faisal and J. Z. Kamiński, "Floquet-Bloch theory of high-harmonic generation in periodic structures", Physical Review A **56**, 748–762 (1997).

[80] T. Tamaya, A. Ishikawa, T. Ogawa, and K. Tanaka, "Diabatic mechanisms of higher-order harmonic generation in solid-state materials under high-intensity electric fields", Physical Review Letters **116**, 016601 (2016).

[81] O. Neufeld, D. Podolsky, and O. Cohen, "Floquet group theory and its application to selection rules in harmonic generation", Nature Communications **10**, 405 (2019).

[82] D. S. Sholl and J. A. Steckel, *Density Functional Theory: A Practical Introduction* (John Wiley & Sons, 2011).

[83] P. Giannozzi, S. Baroni, N. Bonini, M. Calandra, R. Car, C. Cavazzoni, D. Ceresoli, G. L. Chiarotti, M. Cococcioni, I. Dabo, A. Dal Corso, S. de Gironcoli, S. Fabris, G. Fratesi, R. Gebauer, U. Gerstmann, C. Gougoussis, A. Kokalj, M. Lazzeri, L. Martin-Samos, N. Marzari, F. Mauri, R. Mazzarello, S. Paolini, A. Pasquarello, L. Paulatto, C. Sbraccia, S. Scandolo, G. Sclauzero, A. P. Seitsonen, A. Smogunov, P. Umari, and R. M. Wentzcovitch, "QUANTUM ESPRESSO: a modular and open-source software project for quantum simulations of materials", Journal of Physics: Condensed Matter **21**, 395502 (2009).

[84] P. Giannozzi, O. Andreussi, T. Brumme, O. Bunau, M. Buongiorno Nardelli, M. Calandra, R. Car, C. Cavazzoni, D. Ceresoli, M. Cococcioni, N. Colonna, I. Carnimeo, A. Dal Corso, S. de Gironcoli, P. Delugas, R. A. DiStasio, A. Ferretti, A. Floris, G. Fratesi, G. Fugallo, R. Gebauer, U. Gerstmann, F. Giustino, T. Gorni, J. Jia, M. Kawamura, H.-Y. Ko, A. Kokalj, E. Küçükbenli, M. Lazzeri, M. Marsili, N. Marzari, F. Mauri, N. L. Nguyen, H.-V. Nguyen, A. Otero-de-la-Roza, L. Paulatto, S. Poncé, D. Rocca, R. Sabatini, B. Santra, M. Schlipf, A. P. Seitsonen, A. Smogunov, I. Timrov, T. Thonhauser, P. Umari, N. Vast, X. Wu, and S. Baroni, "Advanced capabilities for materials modelling with Quantum ESPRESSO", Journal of Physics: Condensed Matter **29**, 465901 (2017).

[85] L. V. Keldysh, "Coulomb interaction in thin semiconductor and semimetal films", Journal of Experimental and Theoretical Physics Letters **29**, 658 (1979).

[86] M. L. Trolle, T. G. Pedersen, and V. Véniard, "Model dielectric function for 2D semiconductors including substrate screening", Scientific Reports **7**, 39844 (2017).

[87] K. Cong, W. Jiang, B. E. Anthonio, G. T. Noe, H. Liu, H. Kataura, M. Kira, and J. Kono, "Quantum-memory-enabled ultrafast optical switching in carbon nanotubes", ACS Photonics **7**, 1382–1387 (2020).

[88] M. Born, E. Wolf, A. B. Bhatia, P. C. Clemmow, D. Gabor, A. R. Stokes, A. M. Taylor, P. A. Wayman, and W. L. Wilcock, *Principles of Optics* (Cambridge University Press, 1999).

[89] Fully microscopic computations based on Ref. [70] were performed by Johannes Steiner and Stephan W. Koch (Philipps-Universität Marburg, Germany).

[90] W. V. Houston, "Acceleration of electrons in a crystal lattice", Physical Review **57**, 184–186 (1940).

[91] N. Marzari and D. Vanderbilt, "Maximally localized generalized Wannier functions for composite energy bands", Physical Review B **56**, 12847–12865 (1997).

[92] I. Souza, N. Marzari, and D. Vanderbilt, "Maximally localized Wannier functions for entangled energy bands", Physical Review B **65**, 035109 (2001).

[93] A. A. Mostofi, J. R. Yates, Y.-S. Lee, I. Souza, D. Vanderbilt, and N. Marzari, "Wannier90: A tool for obtaining maximally-localised Wannier functions", Computer Physics Communications **178**, 685–699 (2008).

[94] N. Marzari, A. A. Mostofi, J. R. Yates, I. Souza, and D. Vanderbilt, "Maximally localized Wannier functions: Theory and applications", Reviews of Modern Physics **84**, 1419–1475 (2012).

[95] D. Vanderbilt, *Berry Phases in Electronic Structure Theory: Electric Polarization, Orbital Magnetization and Topological Insulators* (Cambridge University Press, Cambridge, 2018).

[96] L. C. Lew Yan Voon and L. R. Ram-Mohan, "Tight-binding representation of the optical matrix elements: Theory and applications", Physical Review B **47**, 15500–15508 (1993).

[97] W. H. Press, S. A. Teukolsky, W. T. Vetterling, and B. P. Flannery, *Numerical Recipes 3rd Edition, The art of scientific computing* (Cambridge University Press, 2007).

[98] T. Ohta, A. Bostwick, T. Seyller, K. Horn, and E. Rotenberg, "Controlling the electronic structure of bilayer graphene", Science **313**, 951–954 (2006).

[99] Y. L. Chen, J. G. Analytis, J.-H. Chu, Z. K. Liu, S.-K. Mo, X. L. Qi, H. J. Zhang, D. H. Lu, X. Dai, Z. Fang, S. C. Zhang, I. R. Fisher, Z. Hussain, and Z.-X. Shen, "Experimental realization of a three-dimensional topological insulator, Bi_2Te_3", Science **325**, 178–181 (2009).

[100] J. Reimann, S. Schlauderer, C. P. Schmid, F. Langer, S. Baierl, K. A. Kokh, O. E. Tereshchenko, A. Kimura, C. Lange, J. Güdde, U. Höfer, and R. Huber, "Subcycle observation of lightwave-driven Dirac currents in a topological surface band", Nature **562**, 396–400 (2018).

[101] B. Lv, T. Qian, and H. Ding, "Angle-resolved photoemission spectroscopy and its application to topological materials", Nature Reviews Physics **1**, 609–626 (2019).

[102] G. Vampa, T. J. Hammond, N. Thiré, B. E. Schmidt, F. Légaré, C. R. McDonald, T. Brabec, D. D. Klug, and P. B. Corkum, "All-optical reconstruction of crystal band structure", Physical Review Letters **115**, 193603 (2015).

[103] T. T. Luu and H. J. Wörner, "Measurement of the Berry curvature of solids using high-harmonic spectroscopy", Nature Communications **9**, 916 (2018).

[104] C.-M. Wang, T.-S. Ho, and S.-I. Chu, "Determination of band structure from the intraband power spectrum of high harmonic generation in crystal", Journal of Physics B: Atomic, Molecular and Optical Physics **49**, 225401 (2016).

[105] A. A. Lanin, E. A. Stepanov, A. B. Fedotov, and A. M. Zheltikov, "Mapping the electron band structure by intraband high-harmonic generation in solids", Optica **4**, 516–519 (2017).

[106] Y.-T. Zhao, Y.-T. Zhao, S.-y. Ma, S.-C. Jiang, Y.-J. Yang, X. Zhao, X. Zhao, and J.-G. Chen, "All-optical reconstruction of k-dependent transition dipole moment by solid harmonic spectra from ultrashort laser pulses", Optics Express **27**, 34392–34404 (2019).

[107] J. L. Hall, "Nobel Lecture: Defining and measuring optical frequencies", Reviews of Modern Physics **78**, 1279–1295 (2006).

[108] N. Picqué and T. W. Hänsch, "Frequency comb spectroscopy", Nature Photonics **13**, 146–157 (2019).

[109] D. Xiao, G.-B. Liu, W. Feng, X. Xu, and W. Yao, "Coupled spin and valley physics in monolayers of MoS_2 and other group-VI dichalcogenides", Physical Review Letters **108**, 196802 (2012).

[110] M. Borsch, C. P. Schmid, L. Weigl, S. Schlauderer, N. Hofmann, C. Lange, J. T. Steiner, S. W. Koch, R. Huber, and M. Kira, "Super-resolution lightwave tomography of electronic bands in quantum materials", Science **370**, 1204–1207 (2020).

[111] C. P. Schmid, "Lightwave electronic control of van der waals quantum materials", PhD thesis (Universität Regensburg, 2021).

[112] C. Meineke, M. Prager, J. Hayes, Q. Wen, L. Z. Kastner, D. Schuh, K. Fritsch, O. Pronin, M. Stein, F. Schäfer, S. Chatterjee, M. Kira, R. Huber, and D. Bougeard, "Scalable high-repetition-rate sub-half-cycle terahertz pulses from spatially indirect interband transitions", Light: Science & Applications **11**, 151 (2022).

[113] D. N. Basov, R. D. Averitt, D. van der Marel, M. Dressel, and K. Haule, "Electrodynamics of correlated electron materials", Reviews of Modern Physics **83**, 471–541 (2011).

[114] J. Spencer, "Learning many-electron wavefunctions with deep neural networks", Nature Reviews Physics **3**, 458–458 (2021).

[115] D. N. Basov, R. D. Averitt, and D. Hsieh, "Towards properties on demand in quantum materials", Nature Materials **16**, 1077–1088 (2017).

[116] A. Chernikov, T. C. Berkelbach, H. M. Hill, A. Rigosi, Y. Li, O. B. Aslan, D. R. Reichman, M. S. Hybertsen, and T. F. Heinz, "Exciton binding energy and nonhydrogenic Rydberg series in monolayer WS_2", Physical Review Letters **113**, 076802 (2014).

[117] E. V. Calman, M. M. Fogler, L. V. Butov, S. Hu, A. Mishchenko, and A. K. Geim, "Indirect excitons in van der waals heterostructures at room temperature", Nature Communications **9** (2018).

[118] R. Su, A. Fieramosca, Q. Zhang, H. S. Nguyen, E. Deleporte, Z. Chen, D. Sanvitto, T. C. H. Liew, and Q. Xiong, "Perovskite semiconductors for room-temperature exciton-polaritonics", Nature Materials **20**, 1315–1324 (2021).

[119] J. R. Schaibley, H. Yu, G. Clark, P. Rivera, J. S. Ross, K. L. Seyler, W. Yao, and X. Xu, "Valleytronics in 2D materials", Nature Reviews Materials **1** (2016).

[120] S. A. Vitale, D. Nezich, J. O. Varghese, P. Kim, N. Gedik, P. Jarillo-Herrero, D. Xiao, and M. Rothschild, "Valleytronics: opportunities, challenges, and paths forward", Small **14**, 1801483 (2018).

[121] T. Kampfrath, K. Tanaka, and K. A. Nelson, "Resonant and nonresonant control over matter and light by intense terahertz transients", Nature Photonics **7**, 680–690 (2013).

[122] S. S. Dhillon, M. S. Vitiello, E. H. Linfield, A. G. Davies, M. C. Hoffmann, J. Booske, C. Paoloni, M. Gensch, P. Weightman, G. P. Williams, E. Castro-Camus, D. R. S. Cumming, F. Simoens, I. Escorcia-Carranza, J. Grant, S. Lucyszyn, M. Kuwata-Gonokami, K. Konishi, M. Koch, C. A. Schmuttenmaer, T. L. Cocker, R. Huber, A. G. Markelz, Z. D. Taylor, V. P. Wallace, J. A. Zeitler, J. Sibik, T. M. Korter, B. Ellison, S. Rea, P. Goldsmith, K. B. Cooper, R. Appleby, D. Pardo, P. G. Huggard, V. Krozer, H. Shams, M. Fice, C. Renaud, A. Seeds, A. Stöhr, M. Naftaly, N. Ridler, R. Clarke, J. E. Cunningham, and M. B. Johnston, "The 2017 terahertz science and technology roadmap", Journal of Physics D: Applied Physics **50**, 043001 (2017).

[123] A. L. Cavalieri, N. Müller, T. Uphues, V. S. Yakovlev, A. Baltuška, B. Horvath, B. Schmidt, L. Blümel, R. Holzwarth, S. Hendel, M. Drescher, U. Kleineberg, P. M. Echenique, R. Kienberger, F. Krausz, and U. Heinzmann, "Attosecond spectroscopy in condensed matter", Nature **449**, 1029–1032 (2007).

[124] M. Schultze, E. M. Bothschafter, A. Sommer, S. Holzner, W. Schweinberger, M. Fiess, M. Hofstetter, R. Kienberger, V. Apalkov, V. S. Yakovlev, M. I. Stockman, and F. Krausz, "Controlling dielectrics with the electric field of light", Nature **493**, 75–78 (2013).

[125] M. Schultze, K. Ramasesha, C. Pemmaraju, S. Sato, D. Whitmore, A. Gandman, J. S. Prell, L. J. Borja, D. Prendergast, K. Yabana, D. M. Neumark, and S. R. Leone, "Attosecond band-gap dynamics in silicon", Science **346**, 1348–1352 (2014).

[126] S. Neppl, R. Ernstorfer, A. L. Cavalieri, C. Lemell, G. Wachter, E. Magerl, E. M. Bothschafter, M. Jobst, M. Hofstetter, U. Kleineberg, J. V. Barth, D. Menzel, J. Burgdörfer, P. Feulner, F. Krausz, and R. Kienberger, "Direct observation of electron propagation and dielectric screening on the atomic length scale", Nature **517**, 342–346 (2015).

[127] A. Sommer, E. M. Bothschafter, S. A. Sato, C. Jakubeit, T. Latka, O. Razskazovskaya, H. Fattahi, M. Jobst, W. Schweinberger, V. Shirvanyan, V. S. Yakovlev, R. Kienberger, K. Yabana, N. Karpowicz, M. Schultze, and F. Krausz, "Attosecond nonlinear polarization and light–matter energy transfer in solids", Nature **534**, 86–90 (2016).

[128] Z. Tao, C. Chen, T. Szilvási, M. Keller, M. Mavrikakis, H. Kapteyn, and M. Murnane, "Direct time-domain observation of attosecond final-state lifetimes in photoemission from solids", Science **353**, 62–67 (2016).

[129] M. Lucchini, S. A. Sato, A. Ludwig, J. Herrmann, M. Volkov, L. Kasmi, Y. Shinohara, K. Yabana, L. Gallmann, and U. Keller, "Attosecond dynamical Franz-Keldysh effect in polycrystalline diamond", Science **353**, 916–919 (2016).

[130] A. Moulet, J. B. Bertrand, T. Klostermann, A. Guggenmos, N. Karpowicz, and E. Goulielmakis, "Soft x-ray excitonics", Science **357**, 1134–1138 (2017).

[131] F. Siek, S. Neb, P. Bartz, M. Hensen, C. Strüber, S. Fiechter, M. Torrent-Sucarrat, V. M. Silkin, E. E. Krasovskii, N. M. Kabachnik, S. Fritzsche, R. D. Muiño, P. M. Echenique, A. K. Kazansky, N. Müller, W. Pfeiffer, and U. Heinzmann, "Angular momentum–induced delays in solid-state photoemission enhanced by intra-atomic interactions", Science **357**, 1274–1277 (2017).

[132] M. Ossiander, J. Riemensberger, S. Neppl, M. Mittermair, M. Schäffer, A. Duensing, M. S. Wagner, R. Heider, M. Wurzer, M. Gerl, M. Schnitzenbaumer, J. V. Barth, F. Libisch, C. Lemell, J. Burgdörfer, P. Feulner, and R. Kienberger, "Absolute timing of the photoelectric effect", Nature **561**, 374–377 (2018).

[133] N. F. Mott, "The basis of the electron theory of metals, with special reference to the transition metals", Proceedings of the Physical Society. Section A **62**, 416–422 (1949).

[134] A. Chernikov, C. Ruppert, H. M. Hill, A. F. Rigosi, and T. F. Heinz, "Population inversion and giant bandgap renormalization in atomically thin WS_2 layers", Nature Photonics **9**, 466–470 (2015).

[135] J. Freudenstein, M. Borsch, M. Meierhofer, D. Afanasiev, C. P. Schmid, F. Sandner, M. Liebich, A. Girnghuber, M. Knorr, M. Kira, and R. Huber, "Attosecond clocking of correlations between Bloch electrons", Nature **610**, 290–295 (2022).

[136] E. Wigner, "On the quantum correction for thermodynamic equilibrium", Physical Review **40**, 749–759 (1932).

[137] W. Yao, D. Xiao, and Q. Niu, "Valley-dependent optoelectronics from inversion symmetry breaking", Physical Review B **77**, 235406 (2008).

[138] J. Wang, J. Ardelean, Y. Bai, A. Steinhoff, M. Florian, F. Jahnke, X. Xu, M. Kira, J. Hone, and X.-Y. Zhu, "Optical generation of high carrier densities in 2d semiconductor heterobilayers", Science Advances **5** (2019).

[139] T. Paasch-Colberg, S. Y. Kruchinin, Ö. Sağlam, S. Kapser, S. Cabrini, S. Muehlbrandt, J. Reichert, J. V. Barth, R. Ernstorfer, R. Kienberger, V. S. Yakovlev, N. Karpowicz, and A. Schiffrin, "Sub-cycle optical control of current in a semiconductor: from the multiphoton to the tunneling regime", Optica **3**, 1358–1361 (2016).

[140] O. Kwon and D. Kim, "PHz current switching in calcium fluoride single crystal", Applied Physics Letters **108**, 191112 (2016).

[141] T. Boolakee, C. Heide, A. Garzón-Ramírez, H. B. Weber, I. Franco, and P. Hommelhoff, "Light-field control of real and virtual charge carriers", Nature **605**, 251–255 (2022).

[142] T. Rybka, M. Ludwig, M. F. Schmalz, V. Knittel, D. Brida, and A. Leitenstorfer, "Sub-cycle optical phase control of nanotunnelling in the single-electron regime", Nature Photonics **10**, 667–670 (2016).

[143] F. Langer, Y.-P. Liu, Z. Ren, V. Flodgren, C. Guo, J. Vogelsang, S. Mikaelsson, I. Sytcevich, J. Ahrens, A. L'Huillier, C. L. Arnold, and A. Mikkelsen, "Few-cycle lightwave-driven currents in a semiconductor at high repetition rate", Optica **7**, 276–279 (2020).

[144] K. F. Mak, K. He, J. Shan, and T. F. Heinz, "Control of valley polarization in monolayer MoS_2 by optical helicity", Nature Nanotechnology **7**, 494–498 (2012).

[145] T. Cao, G. Wang, W. Han, H. Ye, C. Zhu, J. Shi, Q. Niu, P. Tan, E. Wang, B. Liu, and J. Feng, "Valley-selective circular dichroism of monolayer molybdenum disulphide", Nature Communications **3**, 887 (2012).

[146] H. Zeng, J. Dai, W. Yao, D. Xiao, and X. Cui, "Valley polarization in MoS_2 monolayers by optical pumping", Nature Nanotechnology **7**, 490–493 (2012).

[147] W. Yang, J. Shang, J. Wang, X. Shen, B. Cao, N. Peimyoo, C. Zou, Y. Chen, Y. Wang, C. Cong, W. Huang, and T. Yu, "Electrically tunable valley-light emitting diode (vLED) based on CVD-grown monolayer WS_2", Nano Letters **16**, 1560–1567 (2016).

[148] K. F. Mak, K. L. McGill, J. Park, and P. L. McEuen, "The valley Hall effect in MoS_2 transistors", Science **344**, 1489–1492 (2014).

[149] G. Wang, X. Marie, B. L. Liu, T. Amand, C. Robert, F. Cadiz, P. Renucci, and B. Urbaszek, "Control of exciton valley coherence in transition metal dichalcogenide monolayers", Physical Review Letters **117**, 187401 (2016).

[150] Z. Ye, D. Sun, and T. F. Heinz, "Optical manipulation of valley pseudospin", Nature Physics **13**, 26–29 (2016).

[151] J. Kim, X. Hong, C. Jin, S.-F. Shi, C.-Y. S. Chang, M.-H. Chiu, L.-J. Li, and F. Wang, "Ultrafast generation of pseudo-magnetic field for valley excitons in WSe_2 monolayers", Science **346**, 1205–1208 (2014).

[152] E. J. Sie, "Valley-selective optical Stark effect in monolayer WS_2", in *Coherent Light-Matter Interactions in Monolayer Transition-Metal Dichalcogenides* (Springer International Publishing, Nov. 2017), pp. 37–57.

[153] Y. Li, J. Ludwig, T. Low, A. Chernikov, X. Cui, G. Arefe, Y. D. Kim, A. M. van der Zande, A. Rigosi, H. M. Hill, S. H. Kim, J. Hone, Z. Li, D. Smirnov, and T. F. Heinz, "Valley splitting and polarization by the Zeeman effect in monolayer $MoSe_2$", Physical Review Letters **113**, 266804 (2014).

[154] A. Srivastava, M. Sidler, A. V. Allain, D. S. Lembke, A. Kis, and A. Imamoğlu, "Valley Zeeman effect in elementary optical excitations of monolayer WSe_2", Nature Physics **11**, 141–147 (2015).

[155] D. MacNeill, C. Heikes, K. F. Mak, Z. Anderson, A. Kormányos, V. Zólyomi, J. Park, and D. C. Ralph, "Breaking of valley degeneracy by magnetic field in monolayer $MoSe_2$", Physical Review Letters **114**, 037401 (2015).

[156] G. Aivazian, Z. Gong, A. M. Jones, R.-L. Chu, J. Yan, D. G. Mandrus, C. Zhang, D. Cobden, W. Yao, and X. Xu, "Magnetic control of valley pseudospin in monolayer WSe_2", Nature Physics **11**, 148–152 (2015).

[157] A. Arora, R. Schmidt, R. Schneider, M. R. Molas, I. Breslavetz, M. Potemski, and R. Bratschitsch, "Valley zeeman splitting and valley polarization of neutral and charged excitons in monolayer $MoTe_2$ at high magnetic fields", Nano Letters **16**, 3624–3629 (2016).

[158] K. F. Mak and J. Shan, "Photonics and optoelectronics of 2D semiconductor transition metal dichalcogenides", Nature Photonics (2016).

[159] J. Rauch and G. Mourou, "The time integrated far field for Maxwell's and D'Alembert's equations", Proceedings of the American Mathematical Society **134**, 851–858 (2006).

[160] R. M. Arkhipov, M. V. Arkhipov, and N. N. Rosanov, "Unipolar light: existence, generation, propagation, and impact on microobjects", Quantum Electronics **50**, 801–815 (2020).

[161] G. Scuri, Y. Zhou, A. A. High, D. S. Wild, C. Shu, K. De Greve, L. A. Jauregui, T. Taniguchi, K. Watanabe, P. Kim, M. D. Lukin, and H. Park, "Large excitonic reflectivity of monolayer $MoSe_2$ encapsulated in hexagonal boron nitride", Physical Review Letters **120**, 037402 (2018).

[162] J. Horng, E. W. Martin, Y.-H. Chou, E. Courtade, T.-c. Chang, C.-Y. Hsu, M.-H. Wentzel, H. G. Ruth, T.-c. Lu, S. T. Cundiff, F. Wang, and H. Deng, "Perfect absorption by an atomically thin crystal", Physical Review Applied **14**, 024009 (2020).

[163] O. Hess and T. Kuhn, "Maxwell-Bloch equations for spatially inhomogeneous semiconductor lasers. I. Theoretical formulation", Physical Review A **54**, 3347–3359 (1996).

[164] M. Lindberg and R. Binder, "Transversal light forces in semiconductors", Journal of Physics: Condensed Matter **15**, 1119 (2003).

[165] M. Borsch, "Quantum theory of inhomogeneous optical excitations in semiconductors", MA thesis (Philipps Universität Marburg, 2016).

[166] Y.-S. Lee, T. B. Norris, M. Kira, F. Jahnke, S. W. Koch, G. Khitrova, and H. M. Gibbs, "Quantum correlations and intraband coherences in semiconductor cavity QED", Physical Review Letters **83**, 5338–5341 (1999).

[167] R. P. Smith, J. K. Wahlstrand, A. C. Funk, R. P. Mirin, S. T. Cundiff, J. T. Steiner, M. Schafer, M. Kira, and S. W. Koch, "Extraction of many-body configurations from nonlinear absorption in semiconductor quantum wells", Physical Review Letters **104**, 247401 (2010).

[168] H. Wang, K. Ferrio, D. G. Steel, Y. Z. Hu, R. Binder, and S. W. Koch, "Transient nonlinear optical response from excitation induced dephasing in GaAs", Physical Review Letters **71**, 1261–1264 (1993).

[169] N. Peyghambarian, H. M. Gibbs, J. L. Jewell, A. Antonetti, A. Migus, D. Hulin, and A. Mysyrowicz, "Blue shift of the exciton resonance due to exciton-exciton interactions in a multiple-quantum-well structure", Physical Review Letters **53**, 2433–2436 (1984).

[170] M. Kira and S. W. Koch, "Exciton-population inversion and terahertz gain in semiconductors excited to resonance", Physical Review Letters **93**, 076402 (2004).

[171] E. W. Martin, "Coherent spectroscopy at the diffraction limit", PhD thesis (University of Michigan, 2018).

[172] M. Hagn, A. Zrenner, G. Böhm, and G. Weimann, "Electric-field-induced exciton transport in coupled quantum well structures", Applied Physics Letters **67**, 232–234 (1995).

[173] S. Deng, E. Shi, L. Yuan, L. Jin, L. Dou, and L. Huang, "Long-range exciton transport and slow annihilation in two-dimensional hybrid perovskites", Nature Communications **11** (2020).

[174] K. Datta, Z. Lyu, Z. Li, T. Taniguchi, K. Watanabe, and P. B. Deotare, "Spatiotemporally controlled room-temperature exciton transport under dynamic strain", Nature Photonics **16**, 242–247 (2022).

[175] M. Kira, W. Hoyer, T. Stroucken, and S. W. Koch, "Exciton formation in semiconductors and the influence of a photonic environment", Physical Review Letters **87**, 176401 (2001).

[176] W. Hoyer, M. Kira, and S. W. Koch, "Influence of Coulomb and phonon interaction on the exciton formation dynamics in semiconductor heterostructures", Physical Review B **67**, 155113 (2003).

[177] Z. Li, "Exciton transport properties and devices", PhD thesis (University of Michigan, 2022).

[178] Z. Li, M. Florian, K. Datta, Z. Jiang, M. Borsch, Q. Wen, M. Kira, and P. B. Deotare, "Enhanced exciton-drift transport through suppressed diffusion in one-dimensional guides", In preparation (2023).

[179] Z. Li, D. F. C. Leon, W. Lee, K. Datta, Z. Lyu, J. Hou, T. Taniguchi, K. Watanabe, E. Kioupakis, and P. B. Deotare, "Dielectric engineering for manipulating exciton transport in semiconductor monolayers", Nano Letters **21**, 8409–8417 (2021).

[180] Z. Lin, B. R. Carvalho, E. Kahn, R. Lv, R. Rao, H. Terrones, M. A. Pimenta, and M. Terrones, "Defect engineering of two-dimensional transition metal dichalcogenides", 2D Materials **3**, 022002 (2016).

[181] H. Wang, C. Zhang, and F. Rana, "Ultrafast dynamics of defect-assisted electron–hole recombination in monolayer MoS_2", Nano Letters **15**, 339–345 (2014).